이학박사 학위논문

전자 효과가 화학감지체 및 센싱 플랫폼에 미치는 영향에 대한 연구

Studies on the Electronic Effect on Chemosensors and Sensing Platforms

2017년 2월

서울대학교 대학원

화학부 유기화학전공

이 동 남

Abstract

Studies on the Electronic Effect on Chemosensors and Sensing Platforms

Dong-Nam Lee
Major in Organic Chemistry
Department of Chemistry
The Graduate School
Seoul National University

Practical use for the electronic effect on a sensing system can produce innovative approaches that can solve previous questions.

Part I describes a new prototype of flavin sensing strategy based on a photo-oxidation mechanism. A synthetic probe, consisted of a coumarin unit and a bis(diethylamino)-[9*H*]xanthene ring linked through a phenyl spacer, showed high brightness ($\varepsilon \times \Phi_F = 6.5 \times 10^3\ M^{-1}cm^{-1}$) at long wavelength ($\lambda_{em} = 600$ nm) upon oxidation, assisted by flavins' strong electron accepting ability. The oxidation process was promoted upon photoirradiation ($\lambda_{irr} = 450$ nm), which is termed photo-oxidation. Moreover, the probe exhibited high selectivity for flavins over other biological oxidants, remarkable photostability, and most importantly, mitochondria localized ability. Therefore, the probe enabled a

fluorescence monitoring of mitochondrial flavins in live cells and tissues.

Subsequently, an electric field effect on the redox probes was described. Zn^{2+}–dipicolyamine complex (Zn^{II}-DPA) was introduced to the coumarin unit to make probe **1-Zn**, which decreased in the autooxidation rate exerting attractive Coulombic force on the [9*H*]xanthene ring. The positive charge of Zn^{II}-DPA lowered electronic density of the vicinal [9*H*]xanthene ring, and thereby stabilizing probe **1-Zn**. On the other hand, the positive charge increased in the flavin-mediated photo-oxidation rate. The positive charge lowered the reduction potential of isoalloxazine and promoted intermolecular electron transfer from the reduced xanthene to isoalloxazine. Consequently, the probe was successfully applied to various flavin-linked studies such as eosinophils imaging and differential diagnosis of eosinophilia using human blood cell lysate.

Part II describes a new sensing strategy for pyrophosphate (PPi) utilizing electrostatic interactions between negatively charged graphene oxide (GO) and a positively charged synthetic probe that is consisted of phenoxo-bridged binuclear Zn^{2+}–dipicolylamine complex (bisZnDPA) ligand. The combination of the well-known surface characteristics of GO and the selective recognition ability of the bisZnDPA-containing probe resulted in improved selectivity toward PPi even in excess amount of nucleoside triphosphates (NTPs). Consequently, the GO-probe conjugate was successfully applied to polymerase chain reaction monitoring that requires highly selective and sensitive detection of PPi.

Part III describes push-pull π-conjugation effect on small molecular probes. In Section I, paper strip for cyanide (CN^-) detection was prepared by utilizing a synthetic probe, consisted of 6-(dimethylamino)-1,3-benzothiazole linked to

a vinyl malononitrile group. A nucleophilic attack of CN^- on an electron deficient site of probe altered π-conjugation length and dipole moment of the probe, and thereby giving a large spectral shift accompanied by color change, which are desired for naked eye detection. Further, the internal referencing system allowed compensation of measurement errors, which is indispensable for quantitative analysis in point-of-care testing. The paper strip test showed selective response to CN^- with a linear correlation in a range of 0–25 mM in a simple and cost-effective manner.

In Section II, a synthetic probe, bearing a benzothiazolium hemicyanine fluorophore and the bisZnDPA ligand, facilitated cellular imaging of PPi by means of its long wavelength emission ($\lambda_{em} \approx 560$ nm). The probe allowed highly selective fluorescent detection for PPi over other potential competitors except for ATP. Despite the response to ATP, the probe was successfully applied to fluorescence imaging of PPi in the C2C12 myoblast cell line.

Key Words: small molecular probe, fluorescent detection, electric field effect, photo-oxidation, flavin, electrostatic interaction, graphene oxide, pyrophosphate, π-conjugation effect, paper strip

Student Number: 2010-30930

Content

Part I. Electrostatic effect on a photo-oxidation mechanism based flavin probe

Part II. The Combination of Probe and Graphene Oxide for Electrostatics-Driven Sensing Platform for Pyrophosphate Recognition

Background

Section 1. Graphene oxide-probe conjugate system for the selective detection of pyrophosphate

Part III. Push-pull π-conjugated Probes for Paper Strip Test and Bioimaging

Background

PART I.

Electrostatic effect on a photo-oxidation mechanism based flavin probe

Background

1. Introduction to electrostatics in biochemistry

Electrostatic forces play crucial roles in many examples of enzymatic reactions, such as catalysis, gene expression, and the electron transfer process. Electrostatic forces affects various physical and physiological parameters, such as the proximity, surface charge and orientation of proteins, specificity, and electron accepting/donating abilities.[1] The followings are four examples. First, enzyme catalysis occurs by virtue of a well-organized active site structure, in which the transition-state conformation of proteins is stabilized by the electrostatic forces originated from nearby ionisable groups. In carbonic anhydrase II (CA II), the electrostatic environment of zinc ion in the active site is a principal feature governing the enzymatic function of CO_2 hydration, where nucleophilic molecules turns to an activated form that concomitantly is

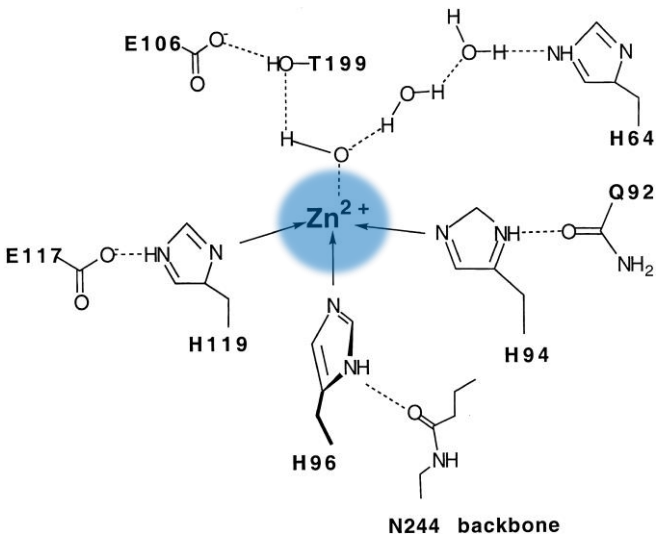

Figure 1. Active site structure of CA II (cited from Hakansson, K. *et al., J. Mol. Biol.* **1992**, *227*, 1192−1204.)

maintained for a sufficient time (i.e., water to hydroxide ion) (Figure 1).[2] Second, gene expression is also regulated by the electrostatic forces in modulation of protein surface charge. Histone deacetylases (HDAC) remove acetyl groups from ε-N-acetyl lysine amino acid on a histone protein, allowing the histone to be super positively charged concomitantly to wrap the DNA more tightly via electrostatic attraction, where the DNA transcription becomes inactive. Histone acetyltransferase (HAT) functions in complementary to regulate the gene expression by acetylation and de-acetylation (Figure 2).[3] Third, electron transfer processes, which are essential events in energy acquisition during respiration and photosynthesis, are finely regulated by electrostatic forces. Thus, the electron accepting/donation ability of prosthetic groups in apoenzyme, such as heme, iron-sulfur cluster, and flavin, are controlled by peptide chains that cause a different electrostatic environment.[4] Fourth, other cases include the signal transduction in neural

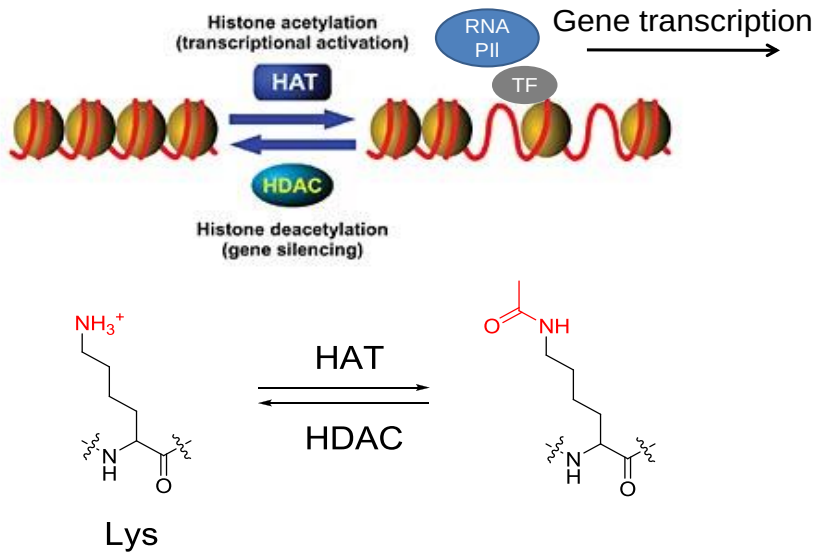

Figure 2. Complementary function of HDAC and HAT to regulate the gene expression.

activities. Changes in electric potential across neural membrane are cellular events during neural activities that underlie basic human behaviors, emotions, perceptions, and thought.[5]

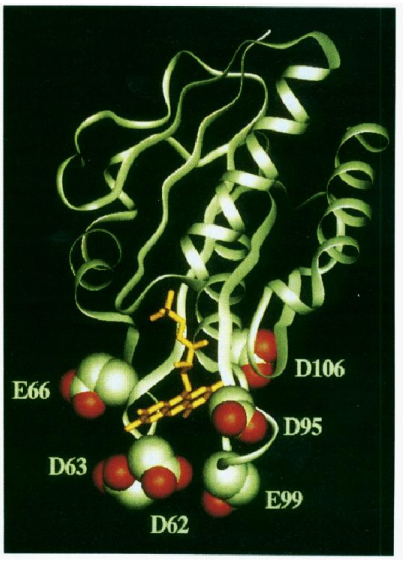

Figure 3. Representation of the six acidic amino acid residues clustered around the flavin mononucleotide binding site in flavodoxin. The acidic residues are depicted as the van der Waals surfaces. The FMN cofactor is highlighted in yellow. Four aspartate and two glutamate were substituted in various combinations to asparagine and glutamine, respectively. The structure is adapted from Swenson, R. P. *et al.*, *Biochemistry* **1995**, *34*, 3183−3192.

In the late 1990s, studies have shown that consideration of electrostatic interactions in redox-active enzymes provide insight into related protein functions, including electron transport and metabolic reactions. Swenson and co-workers demonstrated the electrostatic effect on the redox properties of flavoproteins, especially in flavodoxin.[6] Flavodoxins have a distinguishing feature of very low one-electron reduction potential for the

semiquinone/hydroquinone couple of the flavin mononucleotide (FMN) cofactor (−172 mV for FMN free in solution versus −443 mV when bound). They investigated the contribution of six acidic residues (4Asp, 2Glu), clustered about the FMN binding site, to the perturbation of the redox potential of FMN. The acidic residues were systematically neutralized in various combinations through the substitution of asparagine (Asn) for aspartate (Asp) and glutamine (Gln) for glutamate (Glu) from a net charge of −6 to 0 (Figure 3).[6a] There was obvious correlation between the number of acid to amide substitutions and the midpoint potential shift with an average contribution of about 15 mV per substitution. Thus, the very low reduction potential of the flavodoxin family was accounted by the unfavorable electrostatic environment provided by the six acidic residues, apparently through the destabilization of flavin hydroquinone anion.

Numerous computational and experimental model studies have been established to understand the electrostatic forces in redox chemistry of flavoenzymes. The Rotello group has used host-guest chemistry to explore the nature and effects of flavin cofactor-apoenzyme interactions, and they designed many artificial receptors to examine the effects of π-stacking on flavin redox chemistry.[7] As shown in Figure 4, flavin was oriented over the aromatic surface of the artificial receptor (**1**) through three-point hydrogen bonding of the isoalloxazine and diaminotriazine of the receptor. Modularity of aromatic ring then allowed a varied parametric electronic effect on the isoalloxazine ring while other interactions are kept constant. Interaction with the anthracyl group (**1**c) shifted the reduction potential of flavin to 63 mV more negative than flavin alone while the phenyl group (**1**a) is 18 mV less negative than flavin alone, showing that the increase of electronic density makes flavin more difficult to

reduce by 81 mV ($\Delta\Delta E_{1/2}$).[7c] Consequently, the electrostatic interaction between flavin and the relatively electron-rich aromatics can modulate flavin reduction potential moving to a more negative potential. Therefore, the electron accepting ability is decreased.

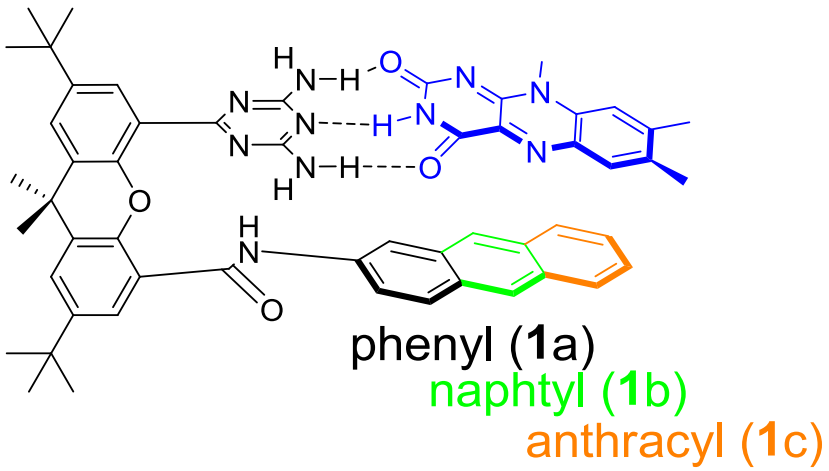

Figure 4. Binding of flavin to receptor **1**, showing computationally predicted π-π overlap with phenyl (**1**a), naphtyl (**1**b), and anthracyl aromatic ring (**1**c).

Recently, researchers have paid considerable attention to the electrostatic effect in developing a new concept of a sensing system. Sections 2 and 3 briefly review the related examples on design strategies, photophysical properties, fluorescence transduction mechanisms, and operating mechanisms of reported fluorescent probes.

2. Electrostatic effect on photoinduced electron transfer mechanism

Photoinduced electron transfer (PET) has been extensively studied and widely used as a sensing mechanism. Generally, PET probes have a 'fluorophore–spacer–receptor' format in a three component system. PET can occur when

redox potentials of the receptor and fluorophore are properly organized to transfer an electron, where the fluorophore accepts an electron from higher HOMO (highest occupied molecular orbital) of the receptor (a-PET) and transfers an electron to a lower LUMO (lowest unoccupied molecular orbital) of the receptor (d-PET) (Figure 5). Sections 2.1 and 2.2 describe examples of the electrostatic effect on the PET process.

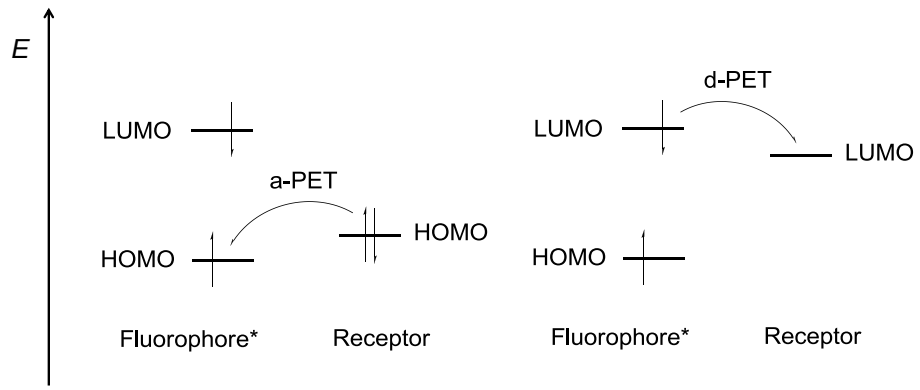

Figure 5. Molecular orbital energy diagrams which show the relative energetic dispositions of the frontier orbitals of the fluorophore and the receptor in (a) a-PET and (b) d-PET situation.

2.1. Model system of electrostatic effect on the PET process

In 1995, the de Silva group exploited pioneering works on the electric-field-effect on electron transfer.[8] Figure 6 shows the 4-aminonaphthalimide fluorophore (**2**), which has a "push-pull" π-electron flow from the 4-amino group as an electron pushing group to the naphthalimide as an electron pulling group. This leads to a strong internal charge transfer (ICT) in the lowest excited singlet state and considerable dipole character. The large dipole moment in an excited state gives rise to a strong photogenerated electric field. The electron

transfer efficiency from electron donor (tertiary amine) to electron acceptor (4-aminonaphthalimide) can be controlled by transition dipole of the fluorophore. When the tertiary amine is linked to the right side (**2**), the electron transfer rate can be accelerated due to an attractive electric field formed by the positive pole at the 4-amino terminus, while the process in the opposite direction (**3**) requires the electron to enter the fluorophore across the imide moiety of the negative pole with its repulsive electric field. The PET rate of compound **2** was estimated over 100-fold larger than those of **3**.[8a]

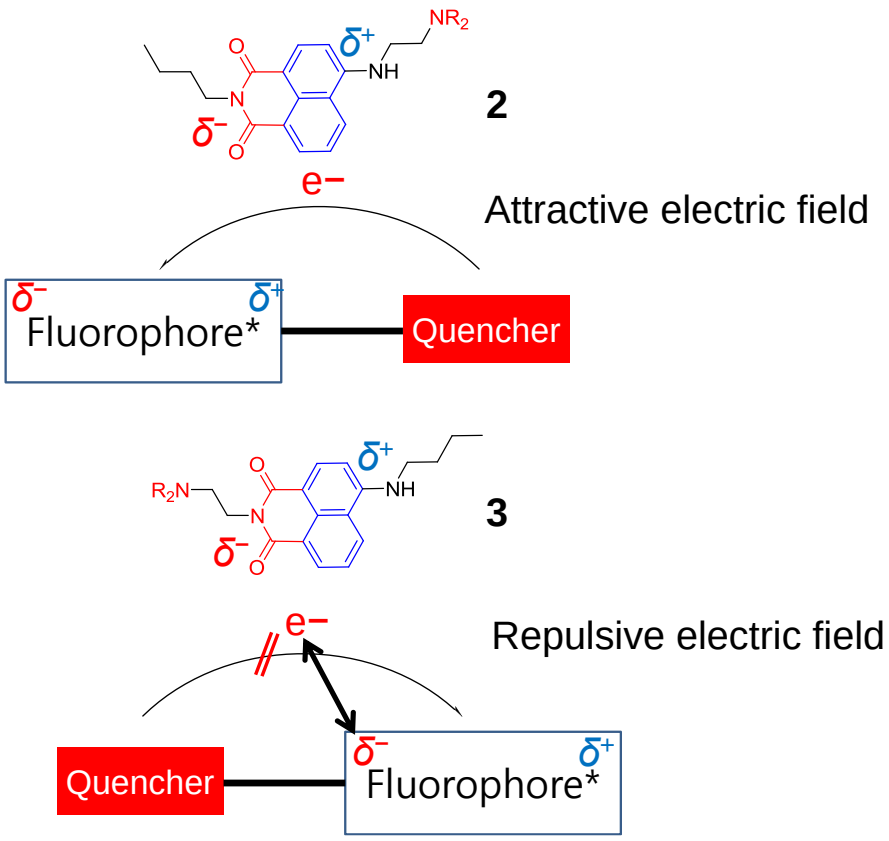

Figure 6. Schematic representation of PET process from amine to fluorophore in excited state through intramolecular electron transfer in two regioisomers (**2** and **3**).

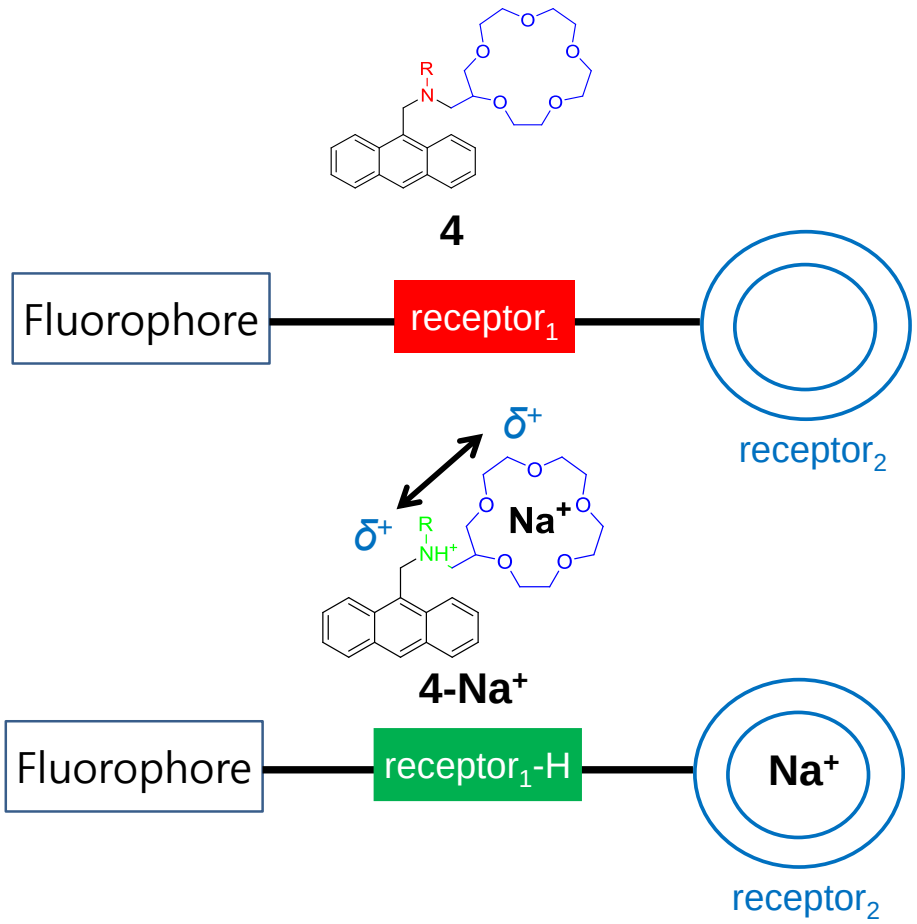

Figure 7. Schematic representation of electric field effect of receptor$_2$ on proton binding on receptor$_1$. After Na^+ binding, the protonation of receptor$_1$ was suppressed due to repulsive electrostatic force originated from Na^+ bound receptor$_2$.

In 2014, the de Silva group also reported the electric-field-effect on pK_a values using 'fluorophore–spacer$_1$–receptor$_1$–spacer$_2$–receptor$_2$' format (**4**), where the amine receptor$_1$ binds H^+ and the crown ether receptor$_2$ binds alkali and alkaline earth cations.[8b] The PET process was controlled by the H^+ binding on the amine receptor$_1$, where the H^+ binding of receptor$_1$ was influenced by the selective cation binding of receptor$_2$. Thus, pK_a values were influenced by the

electric field effect from nearby cations bound on receptor$_2$, which controls the H^+ binding of receptor$_1$. As a consequence of the good geometric fit of Na^+ ion into the [15]crown-5 ether cavity (**4**-**Na**$^+$), it produces the essential contribution, resulting in a large pK_a value shift (ΔpK_a = 0.6) rather than other metal binding (Δp$K_{a,mean}$ = 0.3). In other words, the positive electric field from Na^+ suppressed the H^+ binding on the amine receptor$_1$ due to Coulombic repulsion, decreasing the pK_a value of the amine protonated form (Figure 7). Additionally, alkaline earth cations (divalent ions) provided more effective contribution to the pK_a value. Moreover, size effect of the cations was also observed such that the larger the size, the more shift of pK_a values.

2.2. Membrane potential changes affect PET process

In 2012, the Tsien group found a novel PET sensor that images voltage change in neurons.[9] The PET sensor (**5**) positioned itself in cell membranes, where its hydrocarbon chains, including an aniline group, became stuck in phospholipid bilayers and ionized fluorescein fluorophore was forced to be oriented in the outer leaflet of the plasma membrane. The PET process occurs from the aniline electron donor through the hydrocarbon chain to the fluorophore in response to the electric field, which is caused by a large fraction of the membrane potential. At resting or hyperpolarized potentials, the outside of the cell membrane provides a positively charged environment, where the transmembrane electric field promotes electron transfer from the quencher to an excited-state fluorophore through the molecular wire, thereby quenching fluorescence. Depolarization reverses the electric field, hinders electron transfer, and brightens fluorescence (Figure 8a). Thus, the PET probe is a nice alternative to

classical electrophysiology on an image membrane in accordance with neural activity.

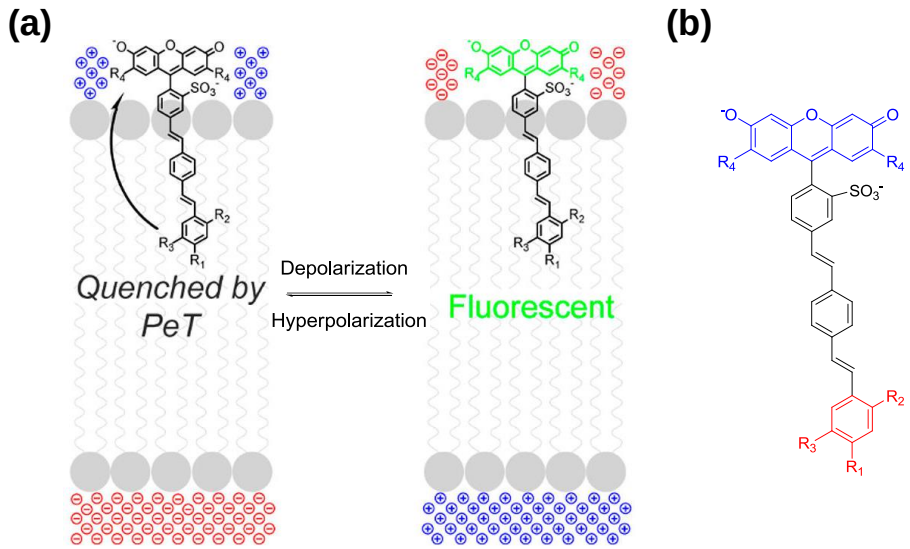

Figure 8. (a) Membrane potential change sensing mechanism of PET sensor **5**: (a) Hyperpolarized (left) membrane potentials (negative inside cell) promote PET and quench fluorescence. Depolarization (positive inside cell) decreases PET and increases fluorescence (right). (b) The voltage-responsive PET sensor composed of PET donor (red) and PET acceptor (blue). The panel (a) is adapted from Tsien, R. Y. *et al.*, *J. Am. Chem. Soc.* **2015**, *137*, 1817−1824.

In 2015, the Tsien group subsequently optimized the voltage-responsive PET probe in respect to thermodynamics.[10] Ten series of new probes were prepared for the purpose of tuning the driving force for PET (ΔG_{PET}) through systematic chemical substitution of PET donor and PET acceptor (Figure 8b). The voltage sensitivity was closely correlated with the experimentally measured redox potentials that adjusted the thermodynamic barrier of the PET process. The

most profitable donor-acceptor pair allowed approximately 2-fold improvement of $\Delta F/F$ value over the previous probe.

3. Electrostatics-driven sensing systems

A variety of probes have been developed using intermolecular interactions (hydrogen bonding, π-π interactions, metal-ligand coordination) and chemical reactions (electrophilic/nucleophilic reaction, reduction/oxidation and enzymatic reaction) with analytes, respectively. Sections 3.1, 3.2, and 3.3 describe examples of the electrostatics-driven sensing mechanisms, including enzyme activity assay, toxic metal, and bio-target detections.

3.1. Electrostatics-driven sensing mechanism in enzyme activity assay

In 2014, the Lawrence group developed a new strategy for protein kinase (PKA) activity assay in fluorescence monitoring.[11] They prepared an arginine-containing sequence in conjunction with fluorophore (Aoc) at terminal glycine, Aoc-GRTGRRFSY, where R is arginine that has a positively charged residue. Introduction of an oppositely charged quencher molecule (**6**) to the positively charged peptide chain led to comprise a protein-quencher supramolecular composite owing to their apparent Coulombic attraction, quenching fluorescence. PKA efficiently phosphorylates the serine residue (S) to create a negatively charged phosphoserine product, resulting in displacement of quencher from the peptide as a result of Coulombic repulsion between them (Figure 9). Therefore, the fluorescence increases in response to the enzymatic reaction.

In 2013, the Yu group exploited a self-assembly-based fluorescent detection method for acetylcholinesterase activity assay.[12] The choline-labeled cationic

pyrene probe (**7**) is forced to induce aggregation with polyanion (polyvinylsulfonate, PVS) in aqueous solution through electrostatic attraction, emerging pyrene excimer emission. Acetylcholinesterase hydrolyzes the probe, and concomitantly triggers charge inversion of the probe, resulting in a deaggregation process of the probe due to Coulombic repulsion between PVS

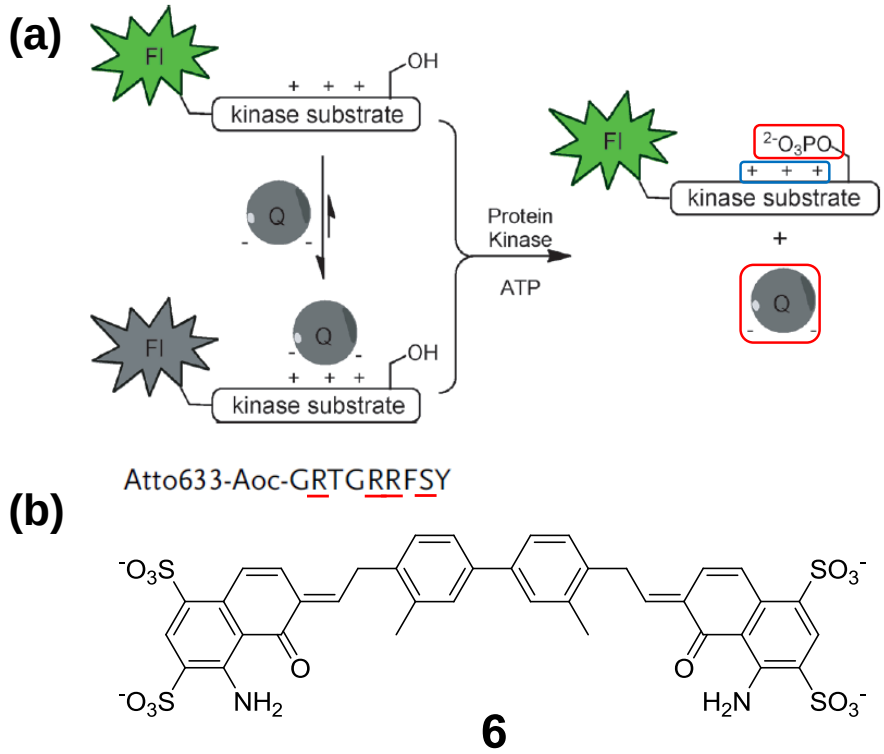

Figure 9. (a) General strategy for the protein kinase catalyzed unquenching of fluorescent kinase substrates. A positively charged fluorescent kinase substrate is quenched upon exposure to a negatively charged quencher dye (**6**). Kinase-catalyzed phosphorylation releases **6** as a result of favorable intramolecular electrostatic interactions between the newly introduced phosphate and positively charged substrate residues (R). The panel (a) is adapted from Lawrence, D. S. *et al.*, *Angew. Chem. Int. Ed.* **2014**, *53*, 3975.

and the probe (Figure 10). The excimer/monomer transition in fluorescence signal was finely controlled by the enzymatic reaction.

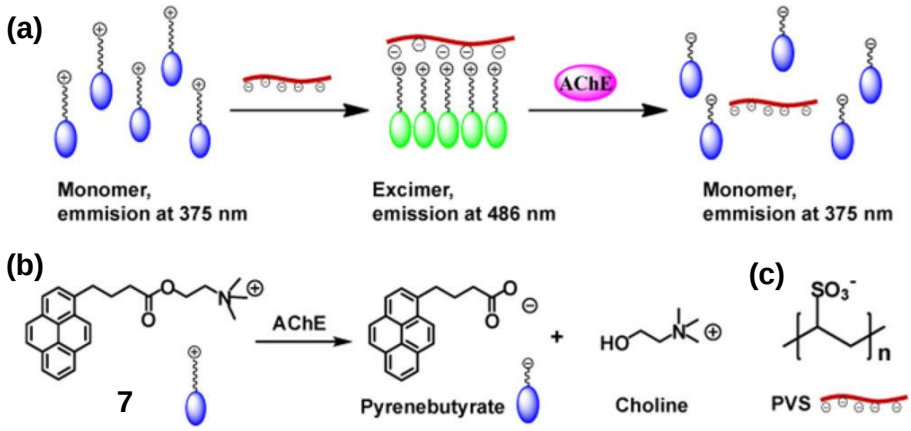

Figure 10. (a) Schematic illustration of the fluorometric detection of acetylcholinesterase (AChE) activity through the excimer/monomer transition. (b) Hydrolysis of pyrene probe **7** by acetylcholinesterase. (c) Structure of PVS. This figure is adapted from Yu, C. *et al.*, *Org. Lett.* **2013**, *15*, 2132−2135.

In 2013, the Wu group developed a ratiometric fluorescence system for carboxylesterase detection based on the fluorescence resonance energy transfer mechanism (FRET).[13] The aggregation of the cationic tetraphenylethene derivative (TPE-N^+) is a well-known natural process. Carboxylesterase hydrolyzes the diacetate group of fluorescein diacetate (FDA), producing negatively charged fluorescein molecules. Upon the enzymatic reaction, electrostatic attraction between the cationic TPE-N^+ and the anionic fluorescein brings them into close proximity, allowing the FRET process to occur, and thereby affording the ratiometric fluorescence in response to carboxylesterase activity (Figure 11).

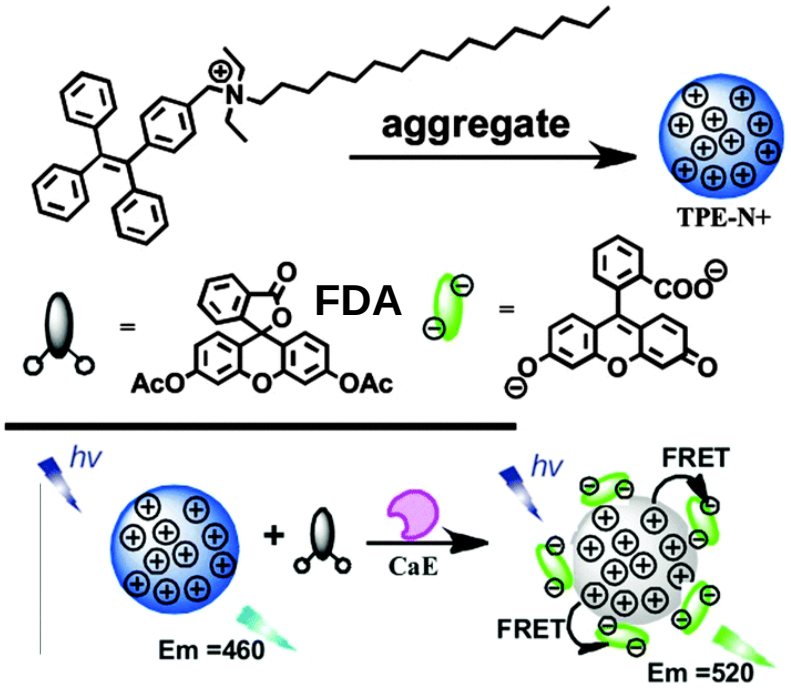

Figure 11. Schematic illustration for the FRET based carboxylesterase (CaE) activity assay. This figure is adapted from Wu, S. *et al., Chem. Commun.* **2015**, *51*, 12791−12794.

3.2. Electrostatics-driven sensing mechanism in mercury detection

In 2014 and 2015, the Prins group developed a self-assembled sensing system that was able to detect Hg^{2+} at low nanomolar concentrations.[14] The positively charged gold nanoparticle (AuNP) interacts with a negatively charged fluorophore (**8**), where the AuNP forms the self-assembled structure (**9**) with the fluorophore. Hg^{2+} derives dimerization of thymine containing ligands (TMP and TDP), which has a low affinity toward the AuNP. After the dimerization, it becomes multivalent anions that turn to be high affinity toward the AuNP, resulting in competitive binding with the AuNP. Thus, the presence of Hg^{2+}

displaces the quenched fluorophore (**8**) from the AuNP, brightening the fluorescence (Figure 12).

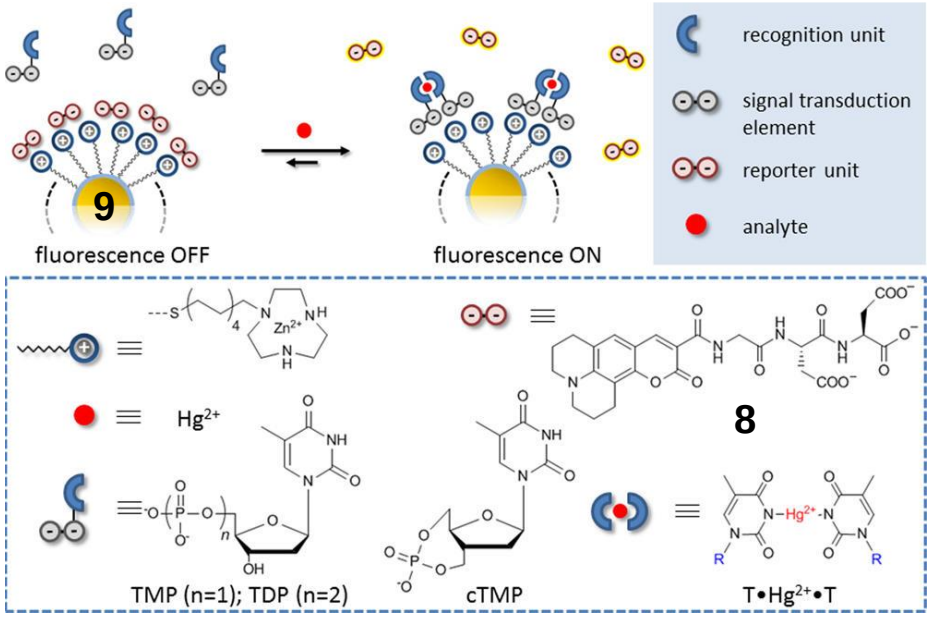

Figure 12. Schematic representation of the sensing assay. Complex formation between two recognition units and Hg^{2+} gives a ternary complex with a high affinity for AuNP **9**, which displaces the quenched fluorescent probe **8** from the surface. This figure is adapted from Prins, L. J. *et al., J. Am. Chem. Soc.* **2014**, *136,* 11288−11291.

3.3. Electrostatics in fluorogenic labeling system to improve property

In 2015, the Kikuchi group focused on the electrostatic effect on protein labeling kinetics.[15] To investigate the effects of surface charges close to the ligand-binding pocket on labeling reactions, they prepared protein mutant (PYP3R) in which anionic residue was converted into arginine, and a labeling probe (**10**) that has a net charge of −1. Owing to the electrostatic attraction between them, the labeling reaction was accelerated and intracellular proteins were detected within an incubation time of only 1 min. These results confirmed

the claim of previous work[16] in which electrostatic attraction between the probe and the protein enhances labeling reactions.

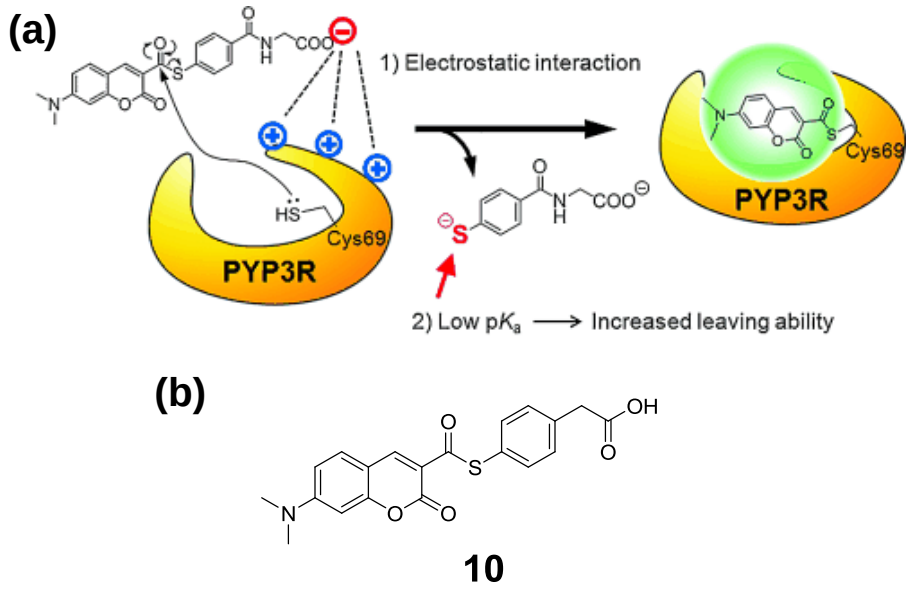

Figure 13. (a) Design of the PYP-tag mutant PYP3R and its fluorogenic probe **10**, with a focus on electrostatic interactions and the pK_a value of the leaving group. (b) Chemical structures of **10**. This figure is adapted from Kikuchi, K. *et al.*, *Angew.Chem. Int.Ed.* **2015**, *54*,14368 –14371.

4. Concluding remarks

In fact, conceptual application of the electrostatic mechanism is of great interest for developing innovative sensors and their corresponding devices. So far, electrostatics-driven sensing systems have been devised to induce electrostatic modification upon target recognition, which results in signal generation typically by an inversed charge or an energy/electron-transfer process. The installment of electrostatics on a sensing system produces an innovative approach for a sensing target to gain the opportunity for significant signal

changes, allowing rapid and portable detection of the target for applications in metabolites imaging, monitoring of the metabolic process and diagnostics.

5. References

(1) Honig, B.; Nicholls, A. *Science* **1995**, *268*, 1144-1149.

(2) (a) McCall, K. A.; Huang, C.-c.; Fierke, C. A. *J. Nutr.* **2000**, *130*, 1437S-1446S; (b) Vallee, B. L.; Auld, D. S. *Proc. Natl. Acad. Sci. USA* **1990**, *87*, 220-224.

(3) Ayer, D. E. *Trends Cell. Biol.* **1999**, *9*, 193-198.

(4) (a) Warshel, A. *Acc. Chem. Res.* **1981**, *14*, 284-290; (b) Menyhárd, D. K.; Náray-Szabó, G. *J. Phys. Chem. B* **1999**, *103*, 227-233.

(5) Freberg, L. *Discovering Behavioral Neuroscience : An Introduction to Biological Psychology*; 3rd ed.; Cengage Learning, 2015.

(6) (a) Zhou, Z.; Swenson, R. P. *Biochemistry* **1995**, *34*, 3183-3192; (b) Zhou, Z.; Swenson, R. P. *Biochemistry* **1996**, *35*, 12443-12454; (c) Zhou, Z.; Swenson, R. P. *Biochemistry* **1996**, *35*, 15980-15988.

(7) (a) Breinlinger, E.; Niemz, A.; Rotello, V. M. *J. Am. Chem. Soc.* **1995**, *117*, 5379-5380; (b) Breinlinger, E. C.; Keenan, C. J.; Rotello, V. M. *J. Am. Chem. Soc.* **1998**, *120*, 8606-8609; (c) Breinlinger, E. C.; Rotello, V. M. *J. Am. Chem. Soc.* **1997**, *119*, 1165-1166.

(8) (a) de Silva, A. P.; Gunaratne, H. Q. N.; Habib-Jiwan, J.-L.; McCoy, C. P.; Rice, T. E.; Soumillion, J.-P. *Angew. Chem. Int. Ed.* **1995**, *34*, 1728-1731; (b) Huxley, A. J. M.; Schroeder, M.; Nimal Gunaratne, H. Q.; de Silva, A. P. *Angew. Chem. Int. Ed.* **2014**, *53*, 3622-3625.

(9) Miller, E. W.; Lin, J. Y.; Frady, E. P.; Steinbach, P. A.; Kristan, W. B.; Tsien, R. Y. *Proc. Natl. Acad. Sci. USA* **2012**, *109*, 2114-2119.

(10) Woodford, C. R.; Frady, E. P.; Smith, R. S.; Morey, B.; Canzi, G.; Palida, S. F.; Araneda, R. C.; Kristan, W. B.; Kubiak, C. P.; Miller, E. W.; Tsien, R. Y. *J. Am. Chem. Soc.* **2015**, *137*, 1817-1824.

(11) Oien, N. P.; Nguyen, L. T.; Jernigan, F. E.; Priestman, M. A.; Lawrence, D. S. *Angew. Chem. Int. Ed.* **2014**, *53*, 3975-3978.

(12) Chen, J.; Liao, D.; Wang, Y.; Zhou, H.; Li, W.; Yu, C. *Org. Lett.* **2013**, *15*, 2132-2135.

(13) Wu, Y.; Huang, S.; Zeng, F.; Wang, J.; Yu, C.; Huang, J.; Xie, H.; Wu, S. *Chem. Commun.* **2015**, *51*, 12791-12794.

(14) (a) Maiti, S.; Pezzato, C.; Garcia Martin, S.; Prins, L. J. *J. Am. Chem. Soc.* **2014**, *136*, 11288-11291; (b) Maiti, S.; Prins, L. J. *Chem. Commun.* **2015**, *51*, 5714-5716.

(15) Hori, Y.; Hirayama, S.; Sato, M.; Kikuchi, K. *Angew. Chem. Int. Ed.* **2015**, *54*, 14368-14371.

(16) Hori, Y.; Norinobu, T.; Sato, M.; Arita, K.; Shirakawa, M.; Kikuchi, K. *J. Am. Chem. Soc.* **2013**, *135*, 12360-12365.

Section 1.

Flavin-mediated photo-oxidation for the detection of mitochondrial flavin's redox balance

Abstract

Herein, a new approach for the detection of mitochondrial flavins will be described, which does not use the green fluorescence of its isoalloxazine moiety. Probe **1** showed superior brightness ($\varepsilon \times \Phi_F$ = 6.5 × 10^3 $M^{-1}cm^{-1}$) at longer wavelengths (maximum emission wavelength, λ_{max} = 600 nm) upon photo-oxidation, assisted by the strong electron accepting ability of the isoalloxazine moiety in flavins. Probe **1** also exhibited high selectivity for flavins over various biological oxidants, remarkable photo-stability, and, most importantly, mitochondrial localization. Furthermore, confocal images revealed that the probe allowed real-time fluorescence monitoring of mitochondrial flavins in cells and tissues, with minimal photobleaching and deep tissue penetration.

1. Introduction

Biologically active flavins such as flavin adenine dinucleotide (FAD) and flavin mononucleotide (FMN) are indispensable cofactors in intracellular oxidation-reduction reactions,[1] along with nicotinamide adenine dinucleotide (NAD) species. Their redox ratio has been recognized as biomarkers for cellular energy metabolism and ultimately, cell viability.[2] The autofluorescence of oxidized flavins, reduced nicotinamide adenine dinucleotide (NADH), and reduced nicotinamide adenine dinucleotide phosphate (NADPH) in living cells or tissues has been used to diagnose human diseases such as diabetes, cancer, and

neurodegeneration.[3] Flavins are mainly localized in the mitochondria as part of the electron transport chain (ETC) and are contained in mitochondrial flavoenzymes such as dihydrolipoamide dehydrogenase.[3a,4] Therefore, flavins are closely related with mitochondrial function and ETC activity.

However, autofluorescence imaging of flavins[2a,5] is limited by their poor spectral characteristics. Their excitation at short wavelengths, between 400−450 nm, only allows shallow penetration and also causes photo-bleaching, thereby limiting their application in deep tissue imaging and long-term imaging of neuronal development, respectively.[6] Moreover, their cellular concentration, especially under varied physiological condition, is remained uncertain[3a,3b] and the quantum yield of FAD is poor (Φ_f = 0.03).[7] The two-photon microscopy application was also hampered by the small cross-section values of flavins,[6a] ranging from 0.01−0.45 Goeppert-Mayer. Therefore, the development of new imaging methods for flavins is an important step towards understanding the energy metabolism in live cells and tissues.

The isoalloxazine ring, the core part of oxidized flavins such as FAD and FMN, is well-known to have high electron accepting ability.[8] Therefore, when the fluorescence of a compound is triggered upon being oxidized by the isoalloxazine moiety, it could be an ideal probe for flavins. In this regard, probe **1** was designed consisting of a coumarin unit and a bis(diethylamino)-[9*H*]xanthene ring linked through a phenyl spacer. Upon photoirradiation, an electron is efficiently moved from the xanthene ring of non-fluorescent probe **1** to the singly occupied molecular orbital of the isoalloxazine ring (Figure 1).[9] Consequently, the xanthene ring of probe **1** becomes fully conjugated to yield oxidized probe **1** ($\mathbf{1}_{ox}$) with a rhodamine-like structure, thereby enabling the detection of flavins (Scheme 1). In fact, $\mathbf{1}_{ox}$ shows spectral behavior

characteristic of rhodamines.[10] To the best of our knowledge, this is the first report for the selective detection of flavins based on the photo-oxidation of the probe.

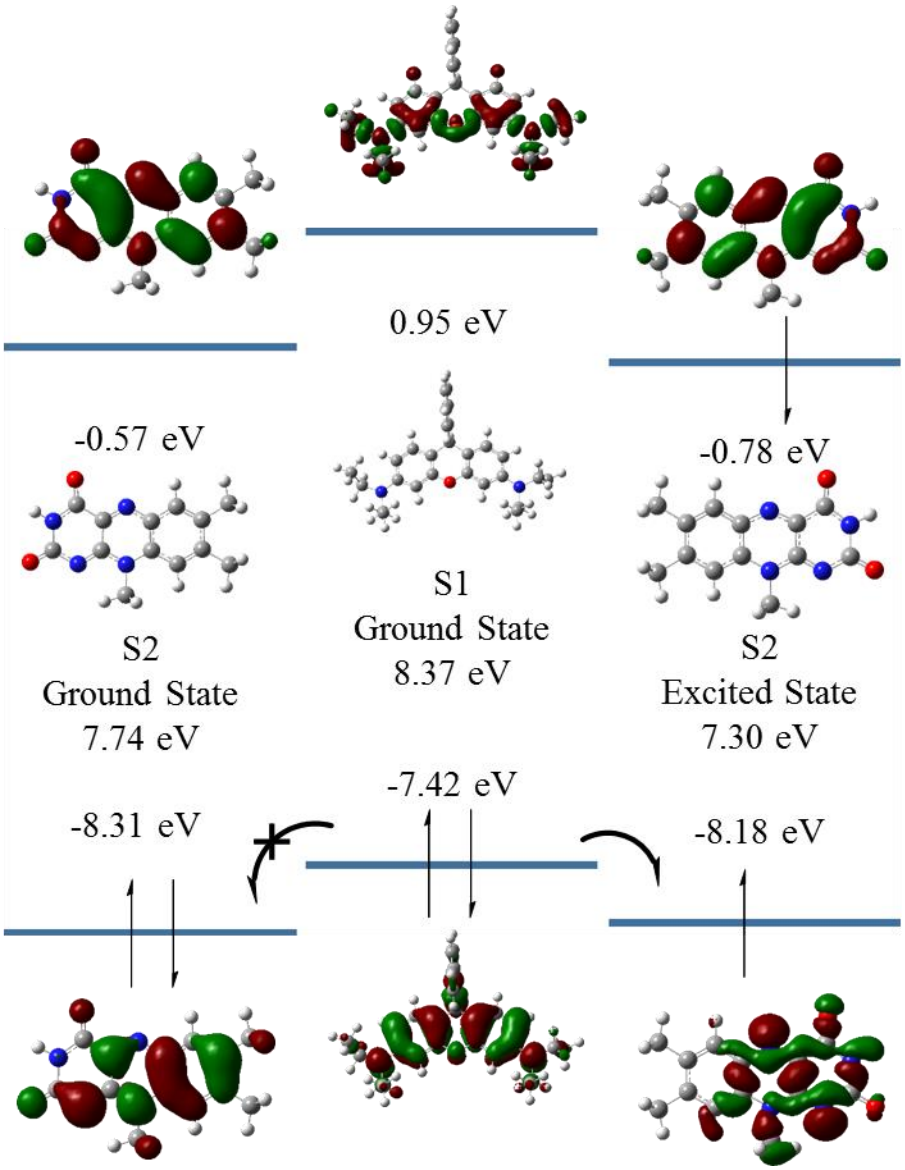

Figure 1. DFT calculations for geometry optimization of probe **1** and isoalloxazine ring. All molecular orbital calculations were performed with MINDO3 method. The energy level of singly occupied molecular orbital (SOMO) was obtained after TD-SCF method.

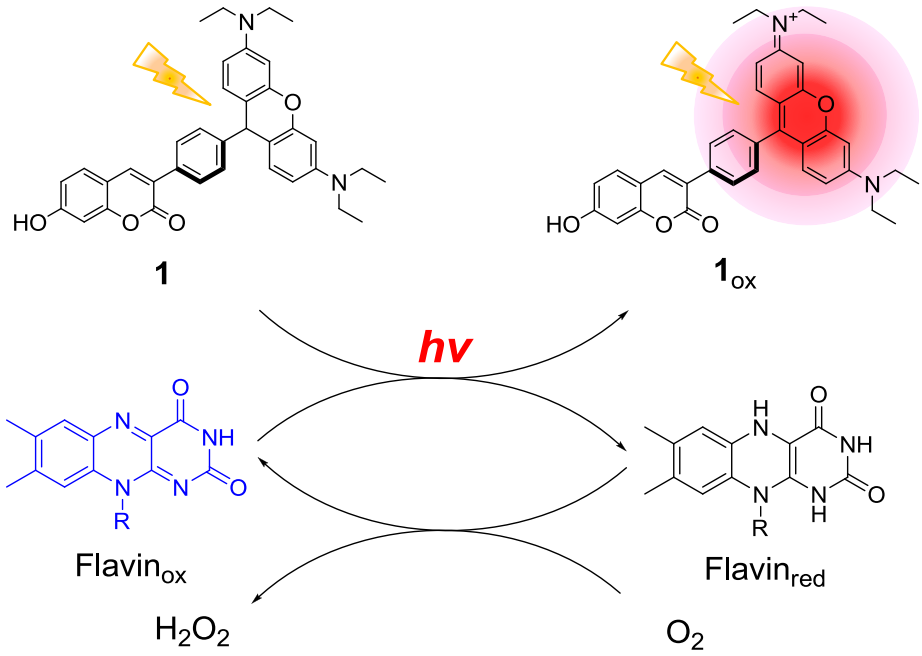

Scheme 1. Proposed mechanism for the detection of flavins by **1**.

2. Data and results

Probe **1** was synthesized by adaptation of previously reported methods.[11] The spectral behavior of probe **1** during its reaction with FMN, an oxidized form of flavins, was investigated under physiological conditions using ultraviolet-visible (UV−Vis) and fluorescence spectroscopies. As shown in Figure 2a, the absorption spectrum of 5 μM probe **1** upon photo-oxidation (365 nm, 6 W, 10 min) with 2.0 equivalents (equiv.) of FMN exhibited a strong new band at 565 nm (log ε_{max} = 4.82), which was attributed to the oxidized xanthene ring. The spectral changes were even visible to the naked eye; the color changed from colorless to pink (inset of Figure 2a). The emission spectra of the corresponding samples showed a time-dependent fluorescence enhancement at 600 nm (Φ_F = 0.20 ± 0.01 in 3:7 CH_3CN: HEPES buffer)[12] upon excitation at 565 nm which

was negligible for the probe alone (Figure 2b). Upon irradiation for 3 min, the

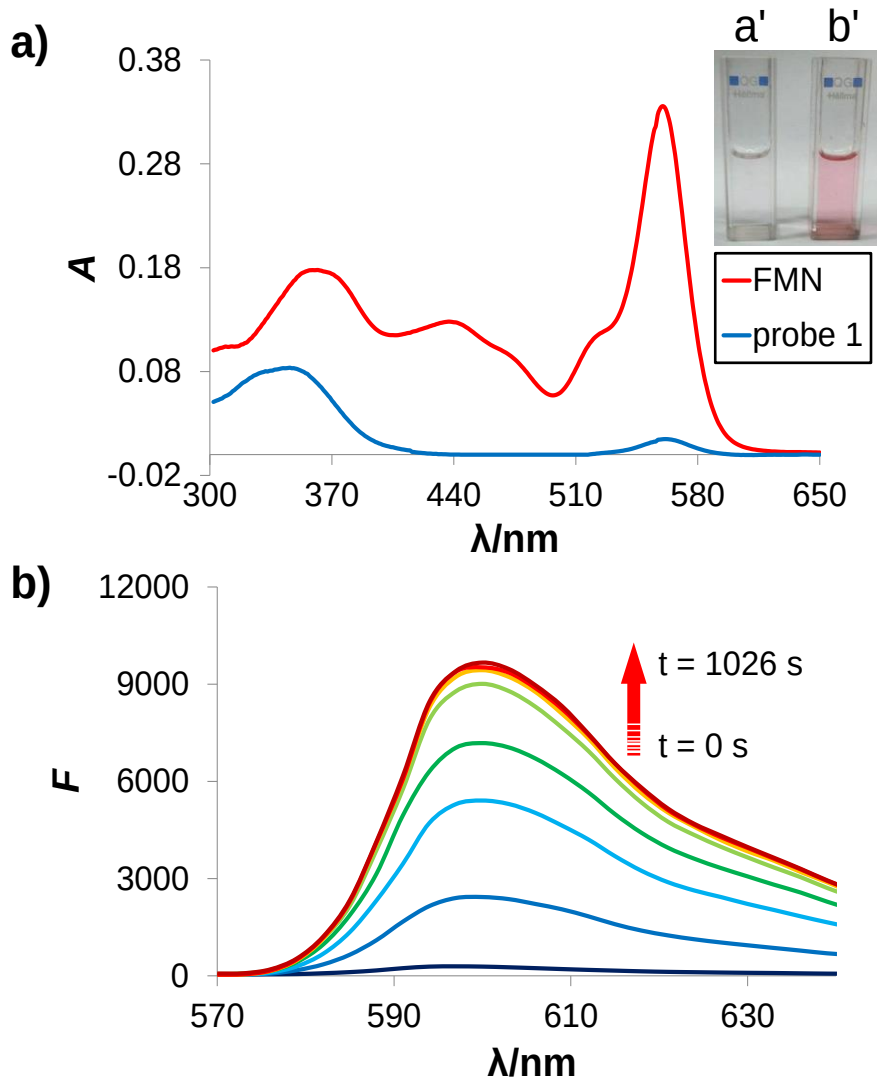

Figure 2. (a) UV−Vis. spectra of **1** (5 μM) in the absence (blue line) and presence (red line) of 2.0 equiv. FMN in 3:7 ACN:Buffer (HEPES 10 mM, pH = 7.4). The spectrum of FMN-driven photo-oxidation was recorded after irradiation with UV hand lamp (365 nm, 6 W) for 10 min. (b) The time-dependent fluorescence spectra in the presence of 2.0 equiv. FMN in which the procedure was performed with the irradiation (365 nm, 6 W). The inset shows the color change of **1** before (a') and after FMN-driven photo-oxidation (b').

detection limit was found to be 5×10^{-7} M, which was sufficiently low to detect intracellular flavins (Figure 3).[3a,3b]

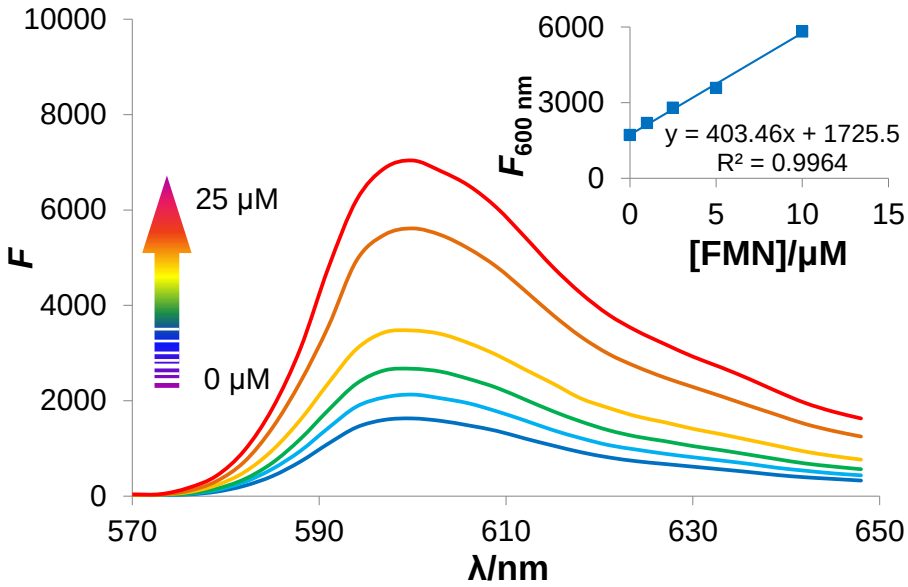

Figure 3. The fluorescence intensity profile of probe **1** (5.0 μM) against concentration of FMN in 3:7 CH_3CN:buffer (10 mM HEPES, pH = 7.4). The inset shows the linear dependence of fluorescence at lower concentrations of FMN. The fluorescence measurement was made after irradiation for 3 min using UV hand lamp.

The importance of FMN for the oxidation of probe **1** was confirmed by high-performance liquid chromatography (HPLC)/UV−Vis spectrophotometer. The UV−Vis detector showed a time-dependent decrease in the absorption intensity at 370 nm (τ = 5.8 min), with concomitant appearance of a new peak at 565 nm (τ = 9.4 min). This newly formed peak was observed only in the presence of FMN (Figure 4). The product $\mathbf{1}_{ox}$ was further confirmed by a peak at m/z = 559.2604 (calcd for $[C_{36}H_{35}N_2O_4]^+$ 559.2597) after preparative HPLC/high

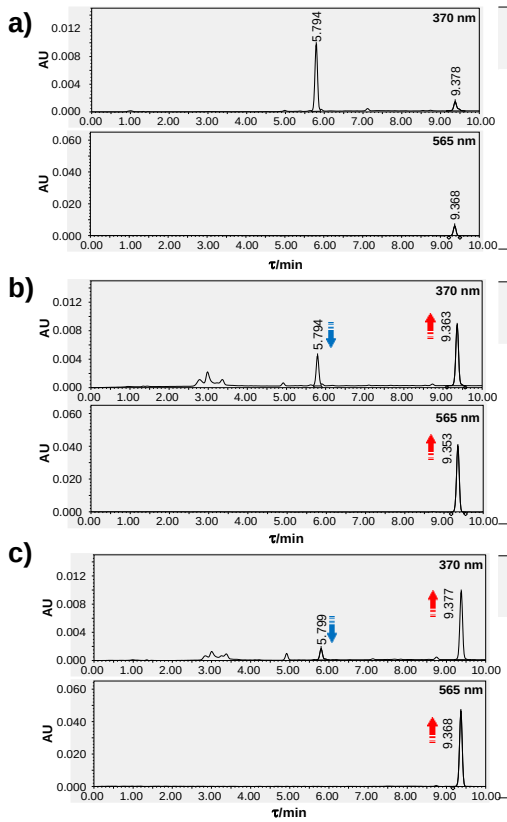

Probe	τ/min	Area	Height
1	5.796	47388	9712
$\mathbf{1}_{ox}$ at 370 nm	9.378	8078	1315
$\mathbf{1}_{ox}$ at 565 nm	9.368	32611	6298

Probe	τ/min	Area	Height
1	5.794	21148	4247
$\mathbf{1}_{ox}$ at 370 nm	9.363	43797	8513
$\mathbf{1}_{ox}$ at 565 nm	9.353	203041	40176

Probe	τ/min	Area	Height
1	5.799	8488	1597
$\mathbf{1}_{ox}$ at 370 nm	9.377	49451	9670
$\mathbf{1}_{ox}$ at 565 nm	9.368	230343	45979

Figure 4. Time-dependent HPLC/UV−Vis. spectra (top line: 370 nm, bottom line: 565 nm) of **1** in 3:7 ACN:Buffer (HEPES 10 mM, pH 7.4) with corresponding values in the absence (a) and presence of 2.0 equiv. FMN (b: after irradiation for 3 min, c: after irradiation for 7 min).

resolution mass spectrometry (HRMS) experiment.

Since the oxidation-reduction of flavins is greatly affected by light irradiation,[13] we measured the apparent oxidation rate constants of probe **1** under various light conditions in the presence of 2.0 equiv. FMN. When the aqueous solution containing probe **1** and FMN was subjected to irradiation under a UV lamp (365 nm, 6 W), the oxidation rate constant was estimated to be k_{obs} = 5.08 × 10^{-3} s^{-1} (half-life, $t_{1/2}$ = 0.136 × 10^{3} sec). Under the ambient

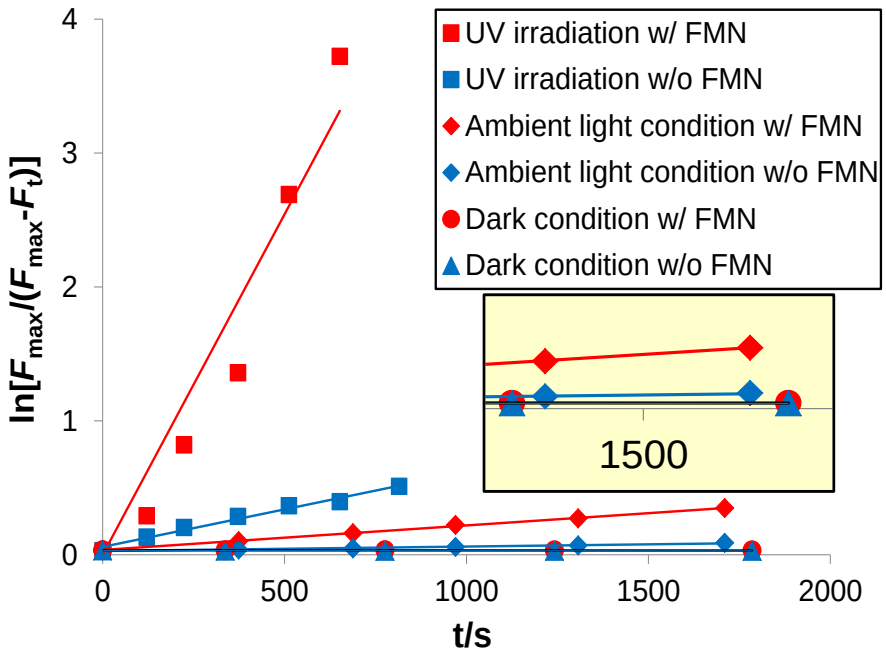

Figure 5. The time-dependent fluorescence intensity profile of probe **1** (5.0 μM) under different light conditions. The inset shows magnified graph.

Table 1. Initial rate constants [a] of **1** [b] in the presence of FMN [c] under different light conditions

Light condition	Auto oxidation	FMN addition
UV irradiation [d]	5.60×10^{-1}	5.08
Ambient light	3.34×10^{-2}	1.83×10^{-1}
Dark	6.88×10^{-4}	1.14×10^{-3}

[a] $k_{obs}/s^{-1} \times 10^{-3}$

[b] 5 μM in 3:7 ACN:Buffer (HEPES 10 mM, pH = 7.4)

[c] 2 equiv., We assumed that there was no photo-decomposition of FMN during the measurement.

[d] 365 nm irradiation (6 W) using Hand held UV lamp (Spectroline, ENF-260C)

light, the rate constant (k_{obs} = 1.83 × 10^{-4} s^{-1}, $t_{1/2}$ = 3.79 × 10^{3} sec), was

approximately 28-fold lower than the value obtained under UV irradiation. Under dark conditions, the rate constant (k_{obs} = 1.14 × 10^{-6} s^{-1}, $t_{1/2}$ = 608 × 10^3 sec) was about 160-fold lower than that estimated under the ambient light conditions. However, when oxidized in the absence of FMN, the rate constants of probe **1** under UV (k_{obs} = 5.60 × 10^{-4} s^{-1}, $t_{1/2}$ = 1.24 × 10^3 sec) and ambient light (k_{obs} = 3.34 × 10^{-5} s^{-1}, $t_{1/2}$ = 20.8 × 10^3 sec) were greater than FMN-assisted oxidation under the dark conditions (Figure 5, Table 1). These results indicate that light exposure is an integral part of the FMN-assisted oxidation; the population of activated FMN molecules increases upon light exposure, which in turn affects the oxidation rate of probe **1**.[14] This was further confirmed by measuring the FMN-assisted oxidation rate constant and fluorescence behavior of probe **1** under varying slit width (*i.e.* 1 × 3, 5 × 3, and 10 × 3 nm) of a fluorometer. Both the rate constant and time-dependent fluorescence

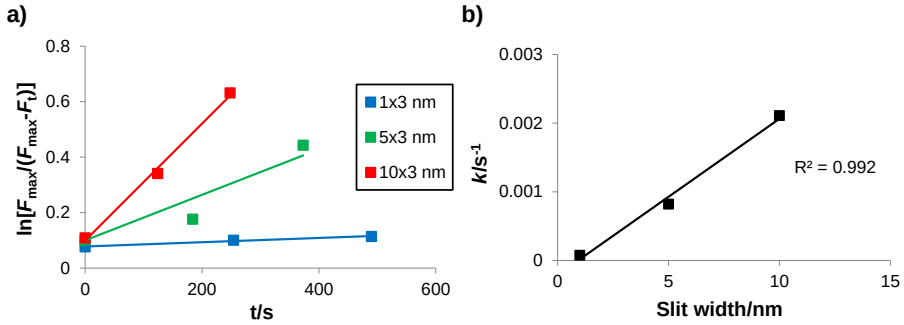

Figure 6. (a) The plot showing the time-dependent fluorescence intensity of **1** (5 μM) in the presence of 2.0 equiv. FMN in 3:7 ACN:Buffer (HEPES 10 mM, pH = 7.4) under varying light intensity by adjusting the slit width of a fluorometer (Jasco FP 6500). The photoirradiation wavelength was at 450 nm, absorption maxima of FMN. (b) Plot showing the linear relationship of rate constants and slit widths. After the photoirradiation, the fluorescence intensity was measured at 600 nm with excitation at 565 nm.

intensity increased with the slit width (Figure 6 and Table 2). FMN-assisted photo-oxidation was most efficient when irradiated at 450 nm, which corresponds to the λ_{max} of FMN (Figure 7 and Table 3).[6a] This clearly indicates that the high-intensity radiation activates the large number of FMN molecules thereby promoting the oxidation rate of probe **1**.

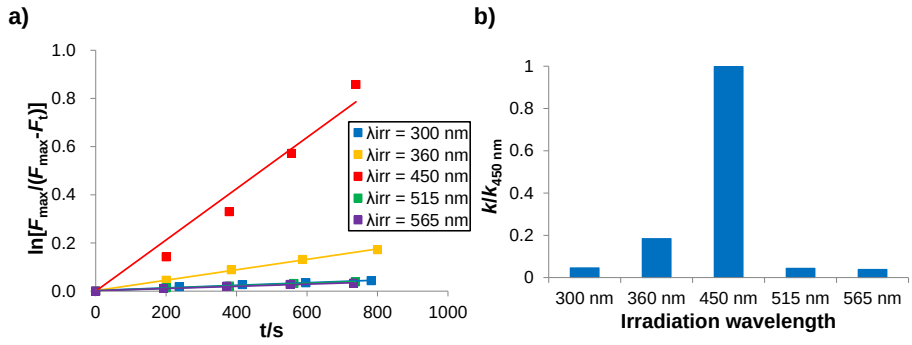

Figure 7. (a) The plot showing the time-dependent fluorescence intensity change of **1** (5 μM) in the presence of 2.0 equiv. FMN in 3:7 ACN:Buffer (HEPES 10 mM, pH = 7.4) upon photoirradiation at different wavelength (λ_{irr} = 300, 360, 450, 515, 565 nm). (b) Bar graph shows ratio ($k/k_{450\ nm}$) of the rate constant upon irradiation at varied wavelength (k, λ_{irr} = 300, 360, 450, 515, 565 nm) to the rate constant upon irradiation at 450 nm ($k_{450\ nm}$). The slit width of photoirradiation was 5×3 nm (sensitivity: medium). After the photoirradiation, the fluorescence intensity of **1** was measured at 600 nm with excitation at 565 nm.

Table 2. Rate constants [a] for oxidation of **1** [b] in the presence of FMN [c] at different slit-widths

Slit width [d]/ nm	k [e]
1×3	7.68×10^{-2}
5×3	8.21×10^{-1}
10×3	2.11

[a] $k_{obs}/s^{-1} \times 10^{-3}$

[b] 5 μM in 3:7 ACN:Buffer (HEPES 10 mM, pH = 7.4)

[c] 2 equiv., We assumed that there was no photo-decomposition of FMN during the measurement.

[d] light exposure at 450 nm (photoirradiation)

[e] fluorescence intensity of **1** was monitored at 600 nm with excitation at 565 nm (monitoring slit width: 5×3 nm)

Table 3. Rate constants [a] for flavin-promoted photo-oxidation of **1** [b] in the presence of FMN [c] under photoirradiation at different wavelength [d]

Irradiation wavelength	$k_{obs}/s^{-1} \times 10^{-3}$
300 nm	5.39×10^{-2}
360 nm	2.16×10^{-1}
450 nm	1.17
515 nm	5.15×10^{-2}
565 nm	4.56×10^{-2}

[a] fluorescence intensity of **1** was monitored at 600 nm with excitation at 565 nm (slit width: 5×3 nm, sensitivity: medium)

[b] 5 μM in 3:7 ACN:buffer (10 mM HEPES, pH = 7.4)

[c] 2 equiv., We assumed that there was no photo-decomposition of FMN during the measurement.

[d] Photoirradiation slit width was 5×3 nm (sensitivity: medium)

The reactivity of probe **1** towards other biologically important oxidants such as NAD^+, Fe(III), 6-biopterin, folic acid, H_2O_2, OCl^-, $OH^{\cdot}$, $O_2^{\cdot-}$, and GSSG was also investigated (Figure 8 and Figure 9) and the results indicated that probe **1** was highly selective towards FMN. Interestingly, even other pterin ring-containing oxidants such as 6-biopterin and folic acid displayed weaker optical responses than those of FMN, which is presumably due to lower excitation energy (E_{ex}) of the isoalloxazine ring.[15] The selectivity of probe **1** to FMN over the other oxidants was clearly visible to the naked eye;

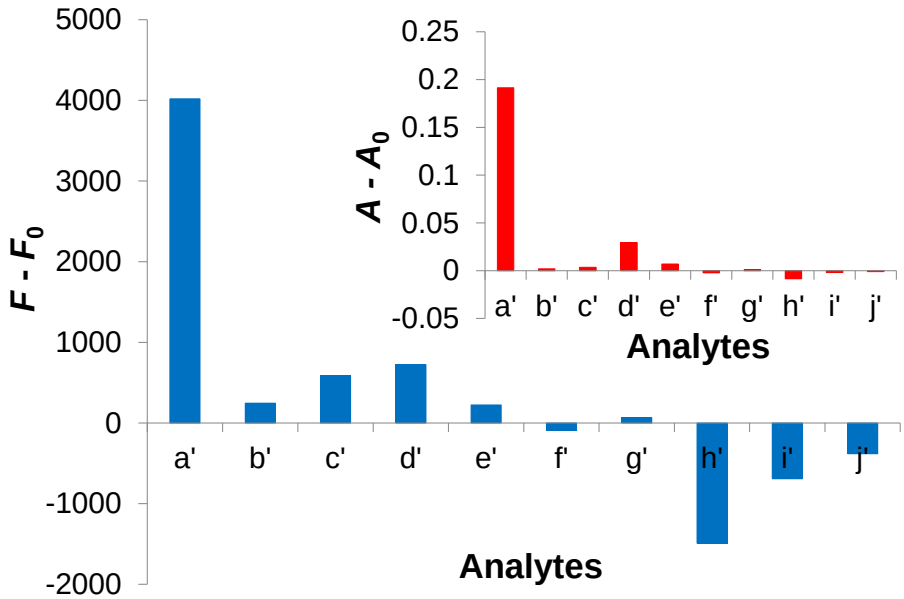

Figure 8. The bar diagram shows changes in the fluorescence intensity of probe **1** (5.0 μM) in the presence of various oxidants such as (a') FMN (2 equiv.), (b') NAD^+ (20 equiv.), (c') Fe(III) (20 equiv.), (d') 6-biopterin (10 equiv.), (e') folic acid (10 equiv.), (f') H_2O_2 (20 equiv.), (g') OCl^- (20 equiv.), (h') $^{\cdot}OH$ (20 equiv.), (i') $O_2^{\cdot-}$ (141 equiv.), and (j') GSSG (163 equiv.). The inset (red bars) shows absorption intensity in the presence of each oxidant. The excitation wavelength was 565 nm. The fluorescence measurement was made after irradiation for 3 min using UV hand lamp.

only the FMN-containing solution showed intense color change from light red to dark red under UV irradiation (Figure 10).

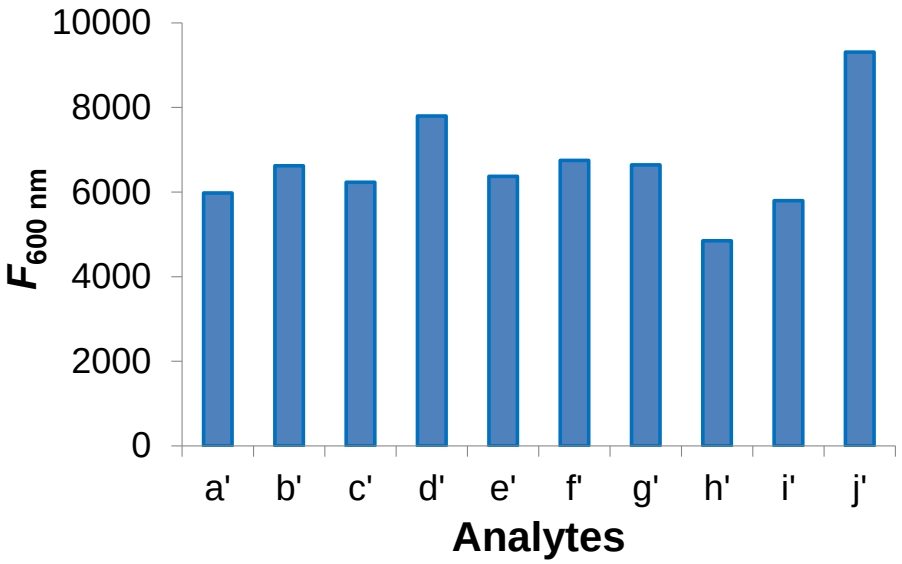

Figure 9. The bar diagram showing the fluorescence response of **1** (5 μM) to FMN (2.0 equiv.) in the presence of different oxidants: (a') control (b') NAD^+ (20 equiv.) (c') Fe(III) (20 equiv.), (d') 6-biopterin (10 equiv.), (e') folic acid (10 equiv.), (f') H_2O_2 (20 equiv.), (g') OCl^- (20 equiv.), (h') $^{\cdot}OH$ (20 equiv.), (i') $O_2^{\cdot -}$ (141 equiv.), (j') GSSG (163 equiv.). After the addition of FMN, various mixtures were irradiated with UV hand lamp for 3 min at RT.

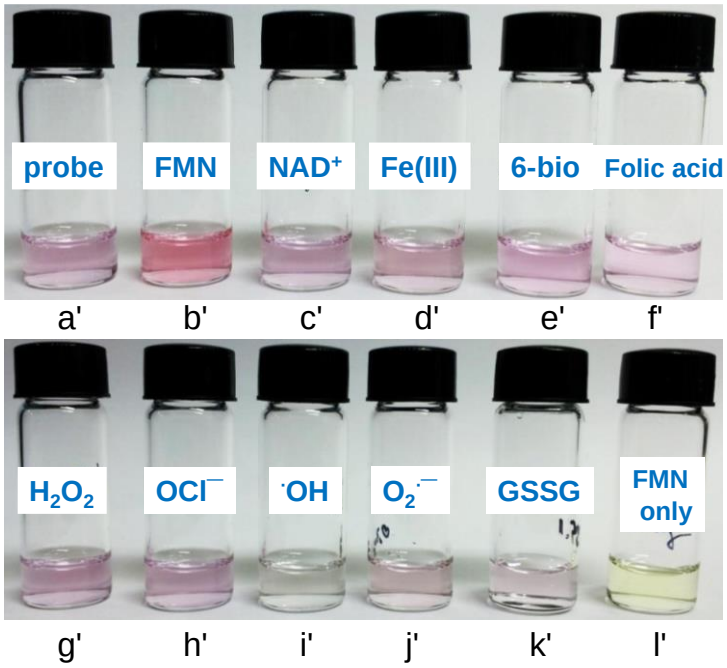

Figure 10. Change in color intensity of **1** (5 μM) in the presence of different oxidants in 3:7 ACN:Buffer (HEPES 10 mM, pH 7.4); (a') **1** only (b') FMN (2 equiv.), (c') NAD^+ (20 equiv.), (d') Fe(III) (20 equiv.), (e') 6-biopterin (10 equiv.), (f') folic acid (10 equiv.), (g') H_2O_2 (20 equiv.), (h') OCl^- (20 equiv.), (i') $^{\cdot}OH$ (20 equiv.), (j') $O_2^{\cdot-}$ (141 equiv.), (k') GSSG (163 equiv.), (l') FMN only (10 μM). After the addition of oxidants, the mixtures were irradiated with UV hand lamp for 3 min at RT.

To demonstrate whether probe **1** can monitor perturbation in the level of oxidized mitochondrial flavins in live cells, a series of confocal microscopic studies were conducted using human astrocytoma cell line U87 and the results are shown in Figure 2. The fluorescence intensity of probe **1** was dramatically increased by UV irradiation (Figure 11a) because it was efficiently oxidized by intracellular flavins (Figure 5). The colocalization experiments of probe **1** along with mitochondria-, lysosome-, and endoplasmic reticulum-selective markers showed that the increased fluorescence by UV irradiation was most clearly observed in mitochondria (Figure 11b), as evident by a high Pearson's correlation coefficient (R = 0.72). Rotenone (ROT), malonate (MAL), antimycin (ANTI), and potassium cyanide (KCN) are well-known inhibitors of ETC complexes I, II, III, and IV, respectively.[16] ROT blocks electron transfer from NADH dehydrogenase to ubiquinone (UQ) thus accelerating another electron transfer pathway, from electron transfer flavoprotein (ETF) to UQ. MAL is a competitive inhibitor of succinate dehydrogenase, which results in the accumulation of succinate. Both ROT and MAL treatment increase the amount of flavin in an oxidized state, whereas ANTI and KCN decrease its oxidized state.[4b,5] Therefore, we determined if probe **1** could measure the level of oxidized mitochondrial flavins upon treatment with ETC inhibitors. In the presence of two of the inhibitors (ROT + ANTI, ROT + KCN, and ROT + MAL), the fluorescence intensity of probe **1** was monitored and quantified relative to that of the untreated cell line (Figure 11c). The results indicated that the fluorescence enhancement was most pronounced with combined treatment of ROT and MAL. This further supports our hypothesis that probe **1** is able to monitor the level of the oxidized mitochondrial flavins perturbed by the treatment of inhibitors.

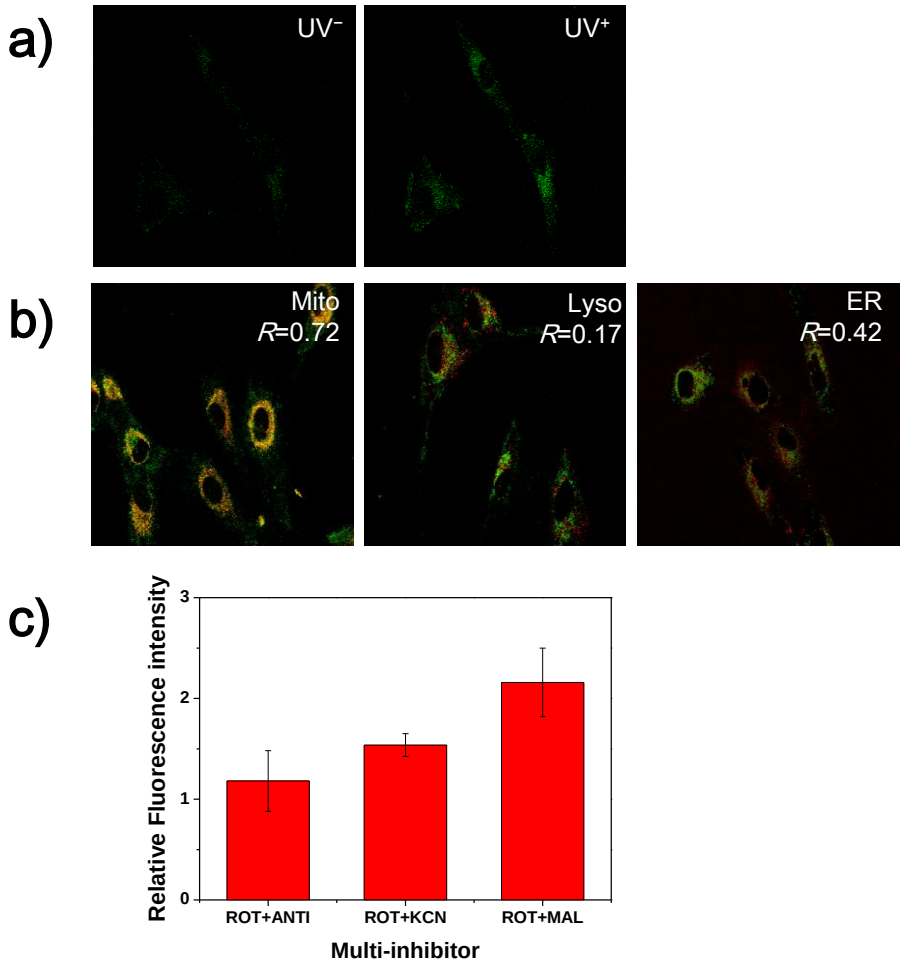

Figure 11. Cellular location of probe **1** in U87 cells and the emission enhancement by ETC inhibitors. (a) Cells were incubated for 5 min with **1** (2.0 μM) at 37°C and irradiated by a UV lamp (365 nm, 6 W) for 3 min. (left without UV; right with UV) (b) The fluorescent image of probe **1** in cells from UV irradiation was colocalized with that of Mito-, Lyso- or ER-tracker, where R indicates the Pearson's correlation coefficient. (c) Red bars indicate the average fluorescence intensity of probe **1** per a cell (n=5) upon the treatment of two inhibitors. The concentrations of ROT, ANTI, MAL, and KCN were 2.5 μM, 5 μg/mL, 0.5 mM and 5 μM, respectively. The fluorescence intensities were normalized relative to that of the untreated cell line. Emission was collected at wavelength 560−610 nm.

To verify that probe **1** can detect bound flavin molecules inside flavoproteins, such as glutathione reductase (GR), the photo-oxidation of probe **1** with a GR-bound FAD molecule was examined. Indeed, the strong fluorescence intensity of probe **1** with GR observed upon photoirradiation (UV hand lamp, 3 min) was dramatically decreased, when GR-bound FAD was first reduced by sodium dithionite (DIT)[4b] prior to its photoreaction with probe **1** (Figure S12a). The DIT-induced FAD reduction is evident by the quenched autofluorescences of GR-bound FAD (Figure S12b) and FMN (Figure S12d). The fluorescence intensity of probe **1** was not influenced by the presence of DIT (Figure S12e). These results support that probe **1** is able to detect flavin molecules bound inside flavoproteins.

Finally, rat hippocampal tissue was treated with ETC inhibitors to demonstrate the validity of probe **1** as a detector of the level of mitochondrial flavin redox states. The hippocampal tissue was first incubated with both ROT and MAL for 30 min, and then with 20 μM probe **1** for additional 30 min at 37˚C. The stacked tissue images upon treatment of inhibitors are shown in Figure 13. The results showed large increase in the emission signals of $\mathbf{1}_{ox}$, particularly in the CA1 region. Along with the results in the U87 cells (Figure 11), these confirmed that probe **1** can detect the inhibitor-induced increase in the level of oxidized flavins.

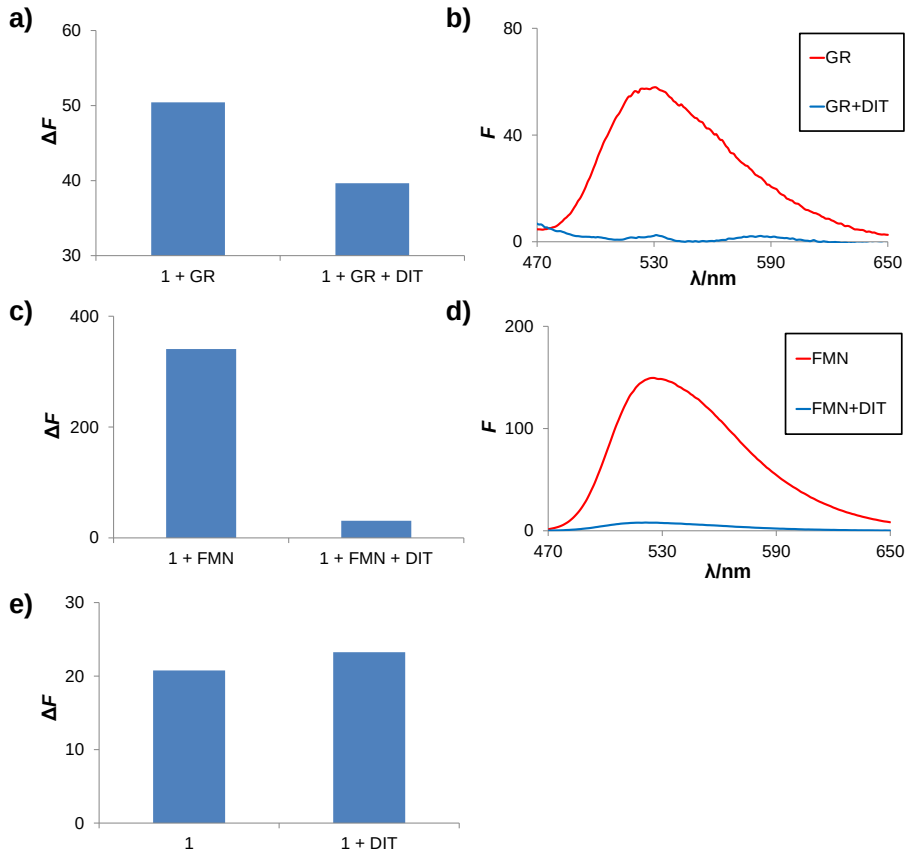

Figure 12. The bar diagram showing that the fluorescence intensity decreases readily when probe **1** (5 μM) was pre-treated with excess sodium dithionite (DIT), prior to its photo-reaction with (a) glutathione reductase (GR, 10 units) and (c) FMN. (b, d) Fluorescence quenching of GR and FMN upon treating with DIT (λ_{ex} = 450 nm). (e) Bar diagram showing negligible emission intensity change of **1** upon treatment with DIT. All spectra were measured in 3:7 ACN:Buffer (HEPES 10 mM, pH 7.4) after the UV hand lamp irradiation for 3 min. In panel (a), (c) and (e), the excitation wavelength was 565 nm showing emission changes at 600 nm.

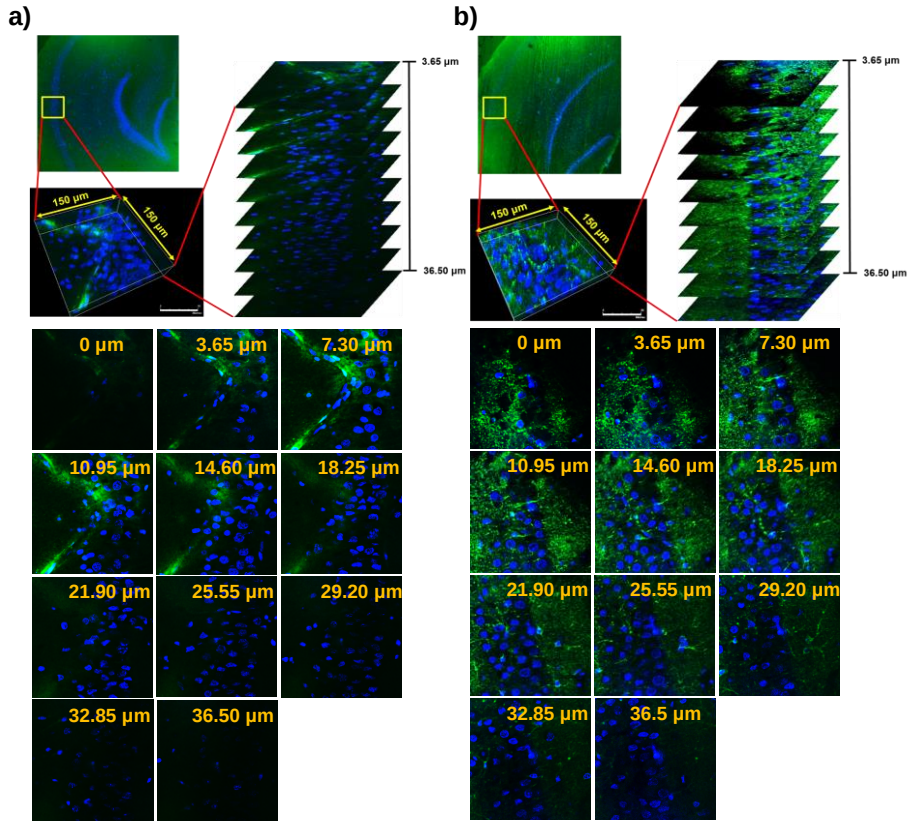

Figure 13. 3-Dimensional confocal images of rat hippocampal tissue stained with probe **1** (20 µM) at depth of 3.65−36.50 µm before (a) and after (b) treatment with 2.5 µM ROT and 0.5 mM MAL. The z-stacked fluorescence confocal images were taken after irradiation with UV lamp for 10 min. The excitation wavelength was 543 nm. Scale bar: 80 µm. The green and blue colors are contributed by probe **1** and Hoechst staining, respectively, under UV irradiation.

3. Conclusion

In conclusion, a novel detection method based on photo-oxidation was described for oxidized flavins detection, which was successfully applied to imaging perturbed mitochondrial flavin's redox balance in live cells and tissues. Probe **1** is characterized by a highly selective fluorescent response to oxidized

flavins. Its mitochondrial localization allows detection of mitochondrial flavins in live cells and brain hippocampal tissues. The method described herein would be a prototype for the development of bioprobes for understanding flavin-linked biological reactions in mitochondria.

4. Experimental

4.1. General procedure

All fluorescence and UV−Vis absorption spectra were recorded with Jasco FP 6500, multimode plate reader (Molecular Devices, SpectraMax M2e), and Beckman coulter DU 800 spectrophotometers. All ^{1}H and ^{13}C NMR spectra were collected in $CDCl_3$ or DMSO-d_6 on a Bruker 300 and Varian 400 MHz spectrometer. All chemical shifts are reported in ppm value using the peak of residual proton signals of TMS as an internal reference. DFT calculations were performed by Hartree-Fock/6-311G method using program "Gaussian 09". HRMS data received directly from the Korea Basic Science Institute. The fluorescence imaging of cells and tissues was performed with a confocal laser scanning microscope (Carl-Zeiss LSM 5 Exciter, Oberko, Germany). All analytes were purchased from Aldrich and used as received. All solvents were analytical reagents from Duksan Pure Chemical Co., Ltd. The DMSO for spectra detection was of HPLC reagent grade, without fluorescent impurity. De-ionized water was used in all studies.

4.2. Synthesis of probe 1

Compound $\mathbf{1_{ox}}$ was prepared by the literature method[11] and synthesis of **1** is described below.

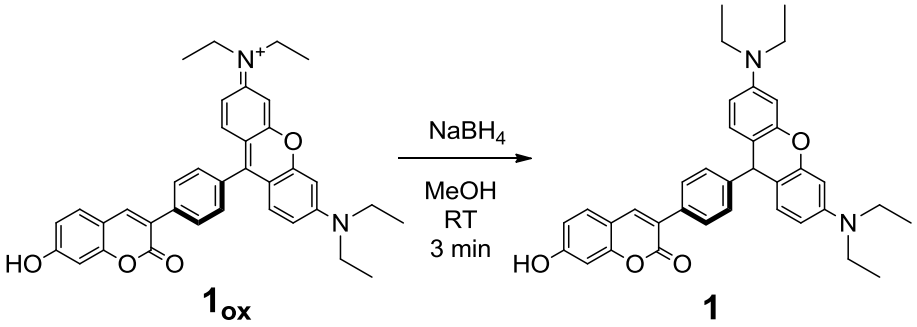

Scheme 2. Synthesis of probe **1**.

To a stirred solution of $\mathbf{1_{ox}}$ in MeOH was added excess amount of $NaBH_4$, and the reaction mixture was stirred at room temperature for 3 min. The solvent was evaporated under reduced pressure, and crude was purified by flash column chromatography using 1:50 MeOH:CH_2Cl_2 as eluent to get the product which was further crystallized from MeOH to give violet colored solid in 56% yield. The compound **1** is air sensitive. So, the synthetic process was completed within 1 hour to minimize the air-oxidation. ^{1}H NMR (DMSO-d_6, 300 MHz): δ 10.59 (s, 1H), 8.06 (s, 1H), 7.56−7.53 (m, 3H), 7.19 (d, 2H, J = 8.1 Hz), 6.85−6.78 (m, 3H), 6.73 (s, 1H), 6.36−6.33 (m, 4H), 5.08 (s, 1H), 3.29 (m, 8H), 1.09 (t, 12H, J = 6.9 Hz,); ^{13}C NMR ($CDCl_3$, 75 MHz): δ 161.8, 159.9, 154.9, 152.1, 148.5, 147.6, 140.4, 132.6, 130.4, 129.2, 128.5, 123.9, 113.8, 113.2, 111.8, 107.7, 102.8, 98.9, 77.2, 44.5, 42.6, 12.6; HRMS (FAB^+, m-NBA) m/z calculated for $C_{36}H_{36}N_2O_4$ 560.2675, observed 560.2670.

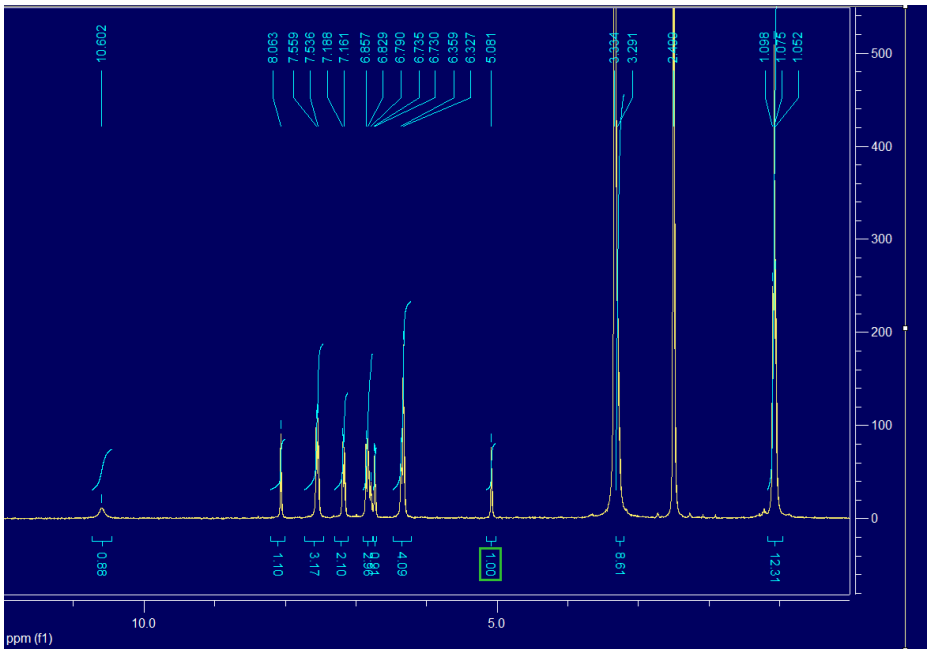

Figure 14. [1]H-NMR spectrum of **1**

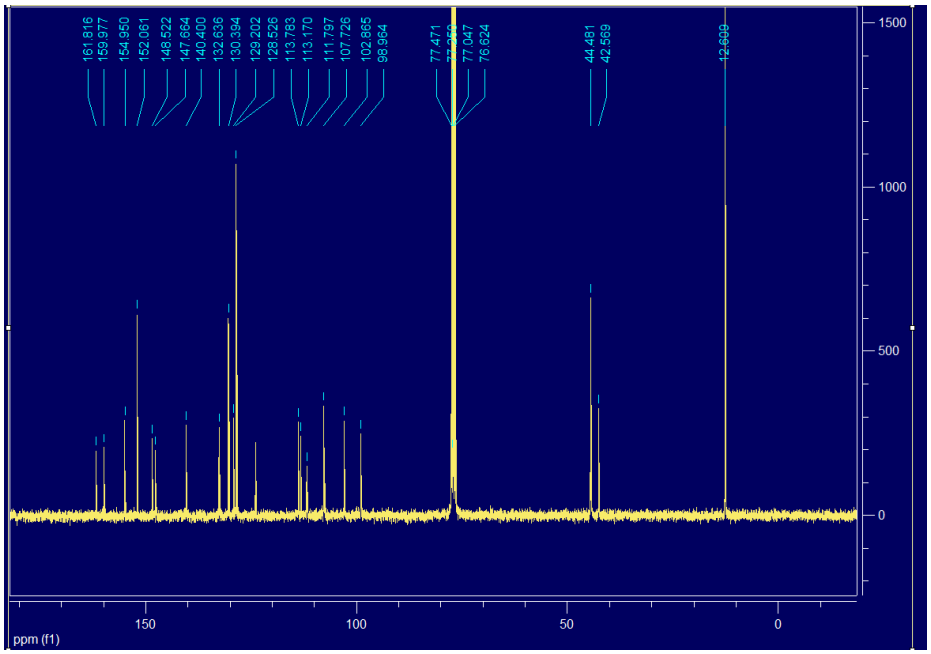

Figure 15. [13]C-NMR spectrum of **1**

4.3. Spectroscopic measurement

Stock solutions of **1** (5 mM in THF) was diluted to 5 μM in 3:7 ACN:Buffer (10 mM HEPES, pH = 7.4). Time-dependent fluorescence spectra of **1** in the presence of 2 equiv. FMN (auto-oxidation *vs.* FMN-promoted oxidation) were recorded under varied light exposure (UV hand lamp, ambient light, dark condition). The oxidation rate constant was measured under pseudo-1st order reaction conditions, assuming that the concentration of flavin remains constant due to short life time of the reduced form. The varying irradiation intensity (λ_{irr} = 450 nm) was feasible by adjusting the irradiation slit width (1×3, 5×3, 10×3 nm) of the fluorometer, Jasco FP 6500. The irradiation wavelength was also controlled by the fluorometer (λ_{irr} = 300, 360, 450, 515, 565 nm), where the slit width of photoirradiation was fixed to 5×3 nm (sensitivity: medium). After the photoirradiation, the fluorescence intensity of **1** was measured at 600 nm with excitation at 565 nm (monitoring slit width: 5×3 nm). For selectivity and competition experiments, stock solutions or solid of different oxidants such as NAD^+, Fe(III), 6-biopterin, folic acid, H_2O_2, OCl^-, $OH^{\cdot}$, $O_2^{\cdot-}$, and GSSG were prepared in deionized water and diluted to different concentrations as shown in Table 4.

Table 4. Preparation of stock solutions and working solutions of **1** and various oxidants

Stock and working solutions	Preparation	Stoichio-metry to probe **1**
5 mM of **1** stock solution	2 μmole of **1** in 0.4 mL of THF	
5 μM of **1** working solution	1000× dilution in 3:7 ACN:buffer (HEPES 10 mM, pH = 7.4)	
FMN	2 μL of 10 mM FMN stock solution into 2 mL of 5 μM **1** solution	2 equiv.
NAD^+, Fe(III), H_2O_2, OCl^-	2 μL of 100 mM each stock solution into 2 mL of 5 μM **1** solution	20 equiv.
6-biopterin, folic acid	10 μL of 10 mM each stock solution into 2 mL of 5 μM **1** solution	10 equiv.
$O_2^{\bullet-}$ [a]	0.1 mg of KO_2 as solid into 2 mL of 5 μM **1** solution	141 equiv.
GSSG [a]	1.0 mg of GSSG as solid into 2 mL of 5 μM **1** solution	163 equiv.
$^{\bullet}OH$ [b]	2 μL of 100 mM Fe(II) stock solution into 2 mL of 100 μM H_2O_2 solution, following by addition of 2 μL of 5 mM **1** stock solution	20 equiv.

[a] The reagent was added as solid into 5 μM **1** solution.
[b] $^{\bullet}OH$ was prepared by the method of Fenton's reagent.

4.4. Determination of reaction rate constant (*k*)

For reaction,

$$A + B \xrightarrow{k} C$$

$$-\frac{d[A]}{dt} = k[A][B]$$

$$-\frac{d[A]}{dt} = k_{obs}[A] \qquad \because \text{ [B] = constant concentration}$$

$$-\int_{[A]_0}^{[A]_t} \frac{d[A]}{[A]} = \int_0^t k_{obs}\, dt$$

$$\ln \frac{[A]_0}{[A]_t} = k_{obs} t$$

For unimolecular reaction, $[A]_t + [C]_t = [C]_{max}$

$$k_{obs} t = \ln \frac{[A]_t + [C]_t}{[A]_t} = \ln\left(1 + \frac{[C]_t}{[C]_{max} - [C]_t}\right) \approx \ln\left(1 + \frac{C_t}{C_{max} - C_t}\right) \qquad (1)$$

In our case,

$[A]_t$ = concentration of **1** unreacted after time elapse of 't' sec

[B] = concentration of FMN

$[C]_t$ = concentration of the $\mathbf{1_{ox}}$ after time elapse of 't' sec

$[C]_{max}$ = maximum concentration of $\mathbf{1_{ox}}$

A_t, C_t, and C_{max} are fluorescence intensity at 600 nm of $[A]_t$, $[C]_t$, and $[C]_{max}$, respectively.

Using equation (1), the initial rate constants was calculated under different light conditions.

5. References and notes

(1) Walsh, C. *Acc. Chem. Res.* **1980**, *13*, 148−155.

(2) (a) Drezek, R.; Brookner, C.; Pavlova, I.; Boiko, I.; Malpica, A.; Lotan, R.; Follen, M.; Richards-Kortum, R. *Photochem. Photobiol.* **2001**, *73*, 636−641; (b) Ramanujam, N.; Richards-Kortum, R.; Thomsen, S.; Mahadevan-Jansen, A.; Follen, M.; Chance, B. *Opt. Express* **2001**, *8*, 335−343; (c) Zhang, Z.; Li, H.; Liu, Q.; Zhou, L.; Zhang, M.; Luo, Q.; Glickson, J.; Chance, B.; Zheng, G. *Biosens. Bioelectron.* **2004**, *20*, 643−650.

(3) (a) Heikal, A. A. *Biomark. Med.* **2010**, *4*, 241−263; (b) Barile, M.; Giancaspero, T. A.; Brizio, C.; Panebianco, C.; Indiveri, C.; Galluccio, M.; Vergani, L.; Eberini, I.; Gianazza, E. *Curr. Pharm. Design* **2013**, *19*, 2649−2675; (c) McKinley, M. C.; McNulty, H.; McPartlin, J.; Strain, J. J.; Scott, J. M. *Eur. J. Clin. Nutr.* **2002**, *56*, 850−856; (d) Jusko, W. J.; Lewis, G. P. *Am. J. Clin. Nutr* **1972**, *25*, 265−268.

(4) (a) Hassinen, I.; Chance, B. *Biochem. Biophys. Res. Commun.* **1968**, *31*, 895−900; (b) Kunz, W. S.; Kunz, W. *Biochim. Biophys. Acta* **1985**, *841*, 237−246.

(5) Sedlic, F.; Pravdic, D.; Hirata, N.; Mio, Y.; Sepac, A.; Camara, A. K.; Wakatsuki, T.; Bosnjak, Z. J.; Bienengraeber, M. *BBA-Bioenergetics* **2010**, *1797*, 1749−1758.

(6) (a) Huang, S.; Heikal, A. A.; Webb, W. W. *Biophys. J.* **2002**, *82*, 2811−2825; (b) Lichtman, J. W.; Fraser, S. E. *Nat. Neurosci.* **2001**, *4*, 1215−1220; (c) Gniadecki, R.; Thorn, T.; Vicanova, J.; Petersen, A.; Wulf, H. C. *J. Cell. Biochem.* **2001**, *80*, 216−222; (d) Lisby, S.; Gniadecki, R.; Wulf, H. C. *Exp. Dermatol.* **2005**, *14*, 349−355.

(7) Visser, A. J. W. G. *Photochem. Photobiol.* **1984**, *40*, 703−706.

(8) Heelis, P. F. *Chem. Soc. Rev.* **1982**, *11*, 15−39.

(9) Tong, W.; Ye, H.; Zhu, H.; D'Souza, V. T. *J. Mol. Struc.-THEOCHEM* **1995**, *333*, 19−27.

(10) Beija, M.; Afonso, C. A. M.; Martinho, J. M. G. *Chem. Soc. Rev.* **2009**, *38*, 2410−2433.

(11) Lin, W.; Yuan, L.; Cao, Z.; Feng, Y.; Song, J. *Angew. Chem. Int. Ed.* **2010**, *49*, 375−379.

(12) (a) The quantum yield was determined using Rhodamine 6G (Φ_f = 0.94 in ethanol) as a standard; (b) Fischer, M.; Georges, J. *Chem. Phys. Lett.* **1996**, *260*, 115−118.

(13) (a) We have measured the rate constant under pseudo-1st order reaction condition, because flavin in reduced form rapidly returns to its original form; (b) Ye, H.; Tong, W.; D'Souza, V. T. *J. Am. Chem. Soc.* **1992**, *114*, 5470−5472.

(14) (a) de Gonzalo, G.; Fraaije, M. W. *ChemCatChem* **2013**, *5*, 403−415; (b) Megerle, U.; Wenninger, M.; Kutta, R.-J.; Lechner, R.; Konig, B.; Dick, B.; Riedle, E. *Phys. Chem. Chem. Phys.* **2011**, *13*, 8869−8880.

(15) Fukuzumi, S.; Tanii, K.; Tanaka, T. *J. Chem. Soc., Chem. Commun.* **1989**, 816−818.

(16) Granger, D. L.; Lehninger, A. L. *J. Cell Biol.* **1982**, *95*, 527−535.

Section 2.

Electrostatic modification of a probe to improve the redox properties on flavin detection

Abstract

A redox photo-chemistry of synthetic probes (**1**, **2**, and **1-Zn**) was simply controlled by introducing a zinc binding site (dipicolylamine, DPA) on coumarin moiety. Zinc-complexation produced a positively charged electrostatic environment on the coumarin (**1-Zn**) on which the induced charge lowered electronic density of a vicinal [9*H*]xanthene ring, stabilizing probe **1-Zn**. An auto-oxidation of **1-Zn** was attenuated by 45% in comparison with probe **1**. The positive net charge of **1-Zn** also offered attractive Coulombic force for flavin detection, lowering the reduction potential of the electron acceptor (isoalloxazine) and improving the intermolecular electron transfer from the [9*H*]xanthene ring to isoalloxazine. The flavin-mediated oxidation rate of **1-Zn** was increased by 1.47-fold in comparison with probe **2**. **1-Zn** showed a highly selective sensing behavior toward flavins, giving high brightness ($\varepsilon \times \Phi_F = 2.80 \times 10^3\ M^{-1}cm^{-1}$) at long wavelength region (λ_{max} = 588 nm), upon flavin-mediated oxidation. Furthermore, flavin-linked studies were performed such as eosinophils imaging and differential diagnosis of eosinophilia, which demonstrates the utilities of **1-Zn** as diagnostic tools.

1. Introduction

Electrostatic interaction is an essential weak force in biology accompanying with hydrogen bonds, π–π interaction, and van der Waals force. For example,

the electrostatic interaction between histone and deoxyribonucleic acid (DNA) backbone is the main driving force to regulate gene expression, which is controlled in complementary by histone deacetylase (HDAC) and histone acetyltransferase (HAT).[1] The reduction potential of flavoenzymes can also be controlled by electrostatic modification of their redox active site.[2] In another case, the osmoregulation is controlled by alterations in the electrostatic forces between cystathionine-synthase (CBS) domains and the surface charge of cell membrane.[3]

Numerous model systems have been devised to examine electrostatic contribution in electron transfer,[4] proton/deprotonation,[5] and enzymatic function in biology.[6] The de Silva group reported the pioneering works about the electric-field-effect on electron transfer or the pK_a value.[4-5] The Rotello group tried to explore the electrostatic effect on the redox chemistry of flavoenzymes, focusing on the electrostatic environment formed around a flavin binding site.[6] Electrostatics-driven sensing strategy also has provided attractive solutions for elusive problems. Recently, the Tsien group developed improved probes that can give fast and significant response to the dynamic change of membrane potential during neural activities.[7] In addition, electrostatics-driven sensing platforms have been developed in enzyme activity assay,[8] toxic metal[9] and bio-target detections.[10]

Flavins (*i.e.*, riboflavin, RF; flavin mononucleotide, FMN; and flavin adenine dinucleotide, FAD) play indispensable roles in many biological redox processes. For example, FMN and FAD are an integral part of the mitochondrial electron transport chain (mETC). Accordingly, their redox state has been considered a biomarker for neurodegenerative diseases.[11] FAD is a central component of eosinophils and generates hydrogen peroxide or superoxide to

damage parasitic organisms for phagocytosis.[12] Thus, the misregulation or break-down of flavin-linked metabolism is correlated with varied symptoms, including neurological problems (*e.g.*, amyotrophic lateral sclerosis, ALS), heart and liver diseases, and even lethal cancers.[11,13] Therefore, an advanced approach for the detection of flavins is highly demanded in the diagnosis of flavin-linked disorders.

In Section 1 of Part I, the fluorescent probe for flavins based on photo-oxidation was described. However, the probe was affected by supplied photon energy even in ambient light exposure, giving activation energy, thereby the probe spontaneously go over the activation barrier to yield its oxidized form. Therefore, it is necessary to control the auto-oxidation in aspects of amenable to handling. For the purpose, dipicolylamine (DPA) was introduced to the coumarin moiety (**1**), and then a zinc binding (**1-Zn**) simply provided a positively charged electrostatic environment on the coumarin moiety (Scheme 1). The zinc complexation resulted in attenuation of the auto-oxidation of **1-Zn**.

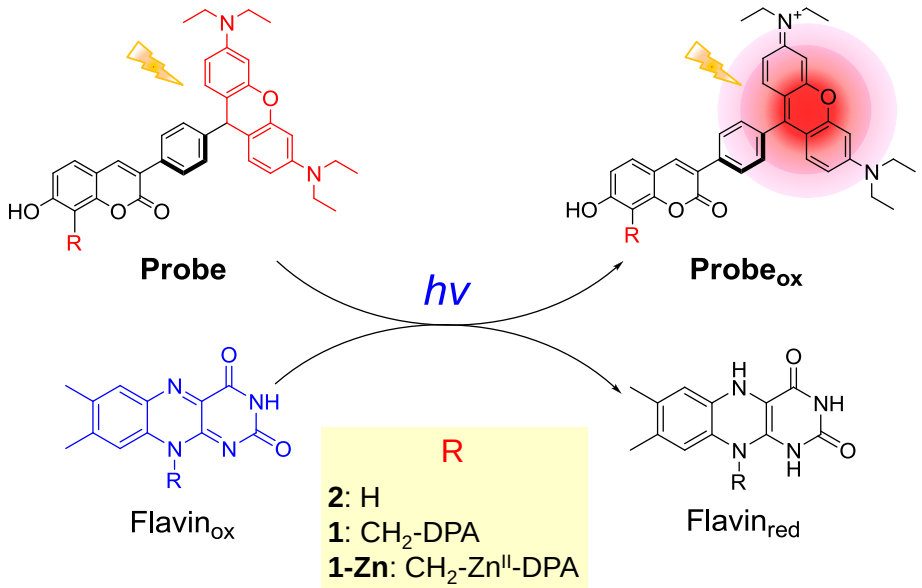

Scheme 1. Proposed mechanism of flavin-mediated photo-oxidation of probe series

The positive net charge around zinc-dipicolylamine (Zn^{II}-DPA) of **1-Zn** also improved the performance on flavin-mediated oxidation. **1-Zn** showed selective sensing behavior toward flavins over other competitive analytes, accompanying with high brightness ($\varepsilon \times \Phi_F = 2.80 \times 10^3\ M^{-1}cm^{-1}$, λ_{em} = 588 nm).[14] Consequently, **1-Zn** was successfully applied to eosinophils imaging and differential diagnosis of eosinophilia.

2. Data and results

2.1. Design and syntheses

The probe series were designed to have two parts: coumarin moiety as a tool for electrostatic modification and [9*H*]xanthene as a redox active site for flavin detection. [9*H*]xanthene is a labile group, and therefore spontaneously converts to its fully conjugated form as described in Section 1 of Part I. The [9*H*]xanthene could be stabilized by modified electrostatic environment around them according to Coulomb's law.[5] In this regard, DPA was introduced on the coumarin moiety to simply modulate the electrostatic environment. The probe series were prepared via three simple steps: the reduction of compound **3** using excess amount of $NaBH_4$ gave probe **2**, which was then subjected to Mannich reaction with dipicolylamine in the presence of formaldehyde to introduce the metal binding site giving probe **1**. Zn^{II}-complexation of **1** simply presented probe **1-Zn** (Scheme 2).

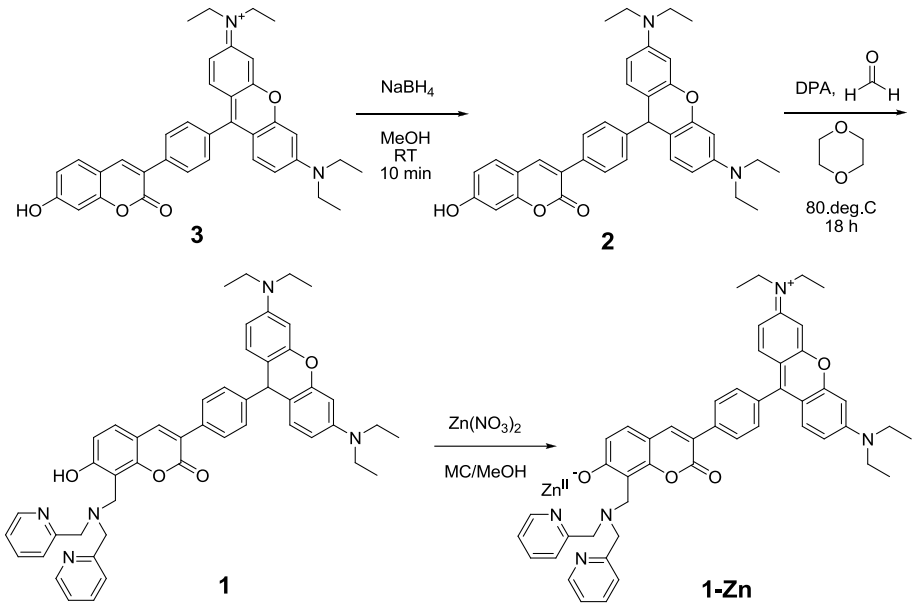

Scheme 2. Syntheses of probes **1**, **2**, and **1-Zn**

2.2. Measurement of the auto-oxidation rate constant

A rate constant for the auto-oxidation was obtained from the time dependent increase in the fluorescence intensity at 600 nm (λ_{ex} = 565 nm) under ambient light exposure at 298, 318, and 333 K. Probe **1-Zn** exhibited the slowest rate of auto-oxidation in the order of **1-Zn** < **2** < **1** at 298 K. In this case, the auto-oxidation rate of **1-Zn** was decreased by 45% in comparison with probe **1**. The auto-oxidation rate of **1-Zn** was also clearly distinguished from **1** and **2** at 318 and 333 K (Table 1 and Figure 1).

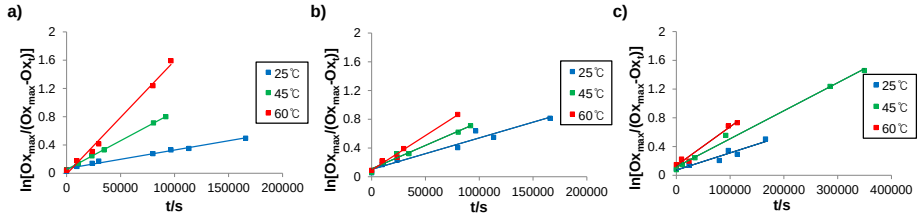

Figure 1. Time coursed plots of (a) **2**, (b) **1**, and (c) **1-Zn** (1 μM each) for the auto-oxidation in a range of 298−333 K. The fluorescence intensities were recorded by multimode plate reader (λ_{em} = 600 nm, λ_{ex} = 565 nm).

2.3. DFT computation

Density functional computation is informative for investigating molecular energy states. Zn^{II}-complexation was expected to stabilize the nearby [9*H*]xanthene, an electron rich site, by attractive Coulombic force.[5] The [9*H*]xanthene of **1-Zn** has a low electronic density in comparison with those of **1** and **2** (Figure 2). Thus the computed thermodynamic barrier of **1-Zn** (ΔE° = 1.75 kcal/mole) was decreased by 73% compared with **1** and **2** (6.49 kcal/mole for **1** and 5.34 kcal/mole for **2**), indicating that the driving force for the auto-oxidation of **1-Zn** is lower than **1** and **2** (Table 2). The response of rate constant

Table 1. Auto-oxidation rate constants [a] of **2**, **1** and **1-Zn**

Probe [b]	*k* at 298 K	*k* at 318 K	*k* at 333 K
2	2.6	8.2	16
1	4.4	6.5	9.6
1-Zn	2.4	3.9	5.4

[a] $10^{-6}k/s^{-1}$. [b] [probe] = 1 μM in 4:6 ACN:buffer (10 mM HEPES, pH = 7.4)

(k) to the change in driving force (ΔE°) has been demonstrated in other electron transfer process.[15]

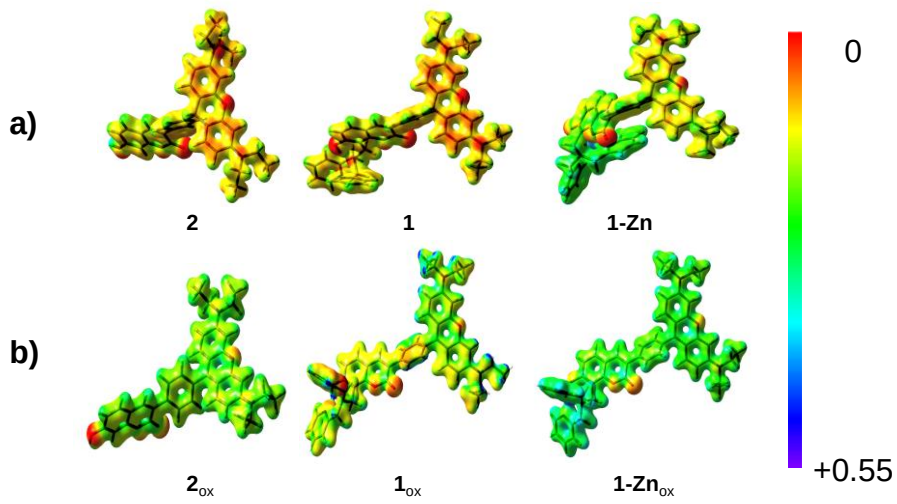

Figure 2. Electrostatic potential map of **2**, **1**, and **1-Zn** (a), and their oxidized form (b). These molecules were geometrically optimized by the method of DFT computation (B3LYP/6-31G level) using Gaussian 09' program.

Table 2. DFT computation (B3LYP/6-31G optimized geometry) of internal energy of three compounds **2**, **1**, and **1-Zn**

	E_{cald} (Hartrees)	E_{cald} (kcal/mole)	$-\Delta E_{cald}$ (kcal/mole)
2	0.687	431.66	5.34
$\mathbf{2}_{ox}$	0.679	426.32	
1	0.946	593.69	6.49
$\mathbf{1}_{ox}$	0.936	587.20	
1-Zn	0.932	584.88	1.75
$\mathbf{1\text{-}Zn}_{ox}$	0.929	583.13	

2.4. Thermodynamic and kinetic studies on flavin-mediated oxidation

In cyclic voltammetry, RF, FMN, and FAD exhibited quasi-reversibly reductive waves at $E_{red}°'$ = −0.419, −0.420, and −0.435 V (vs Ag/AgCl, scan rate = 0.1 V/s), respectively (Table 3). The most negative reduction potential was that of FAD, which is due to the electric field of an anionic 5′-diphosphate group[2a] and π–π stacking of isoalloxazine with the electron-rich adenine group.[16] After flavin reduction, a repulsive electrostatic force arises between the reduced form of isoalloxazine and the phosphate group of FMN and FAD.[2a] Upon the addition of 5 equiv. ZnDPA (Chart 1), the reduction potentials of FMN and FAD moved to the less negative values of $E_{red}°'$ = −0.402, and −0.417 V, respectively ($\Delta E_{red}°'$ = 18 mV each), unlike the negligible shift upon RF addition (Figures 3 and 4). Therefore, the electrostatic repulsion on FMN and FAD could be reduced by ZnDPA binding on the phosphate group.

Table 3. Reduction potential [a] of flavins [b] upon the addition of ZnDPA

ZnDPA/mM	RF	FMN	FAD
0	-0.419	-0.420	-0.435
1	-0.419	-0.410	-0.428
5	-0.419	-0.402	-0.417

[a] The reduction potential ($E_{red}°'$, V vs. Ag/AgCl) was estimated from the mean of two peaks, cathodic (E_{pc}) and anodic (E_{pa}) potential.
[b] 1 mM in 10 mM HEPES buffer (pH = 7.4)

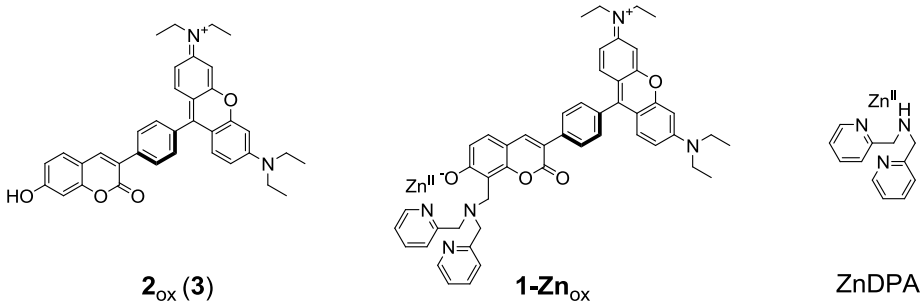

Chart 1. Probes in oxidized form **2_{ox}**, **1-Zn_{ox}**, and ZnDPA

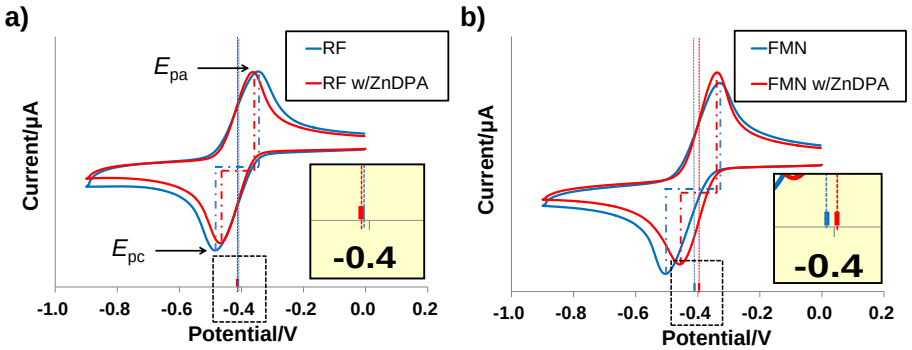

Figure 3. Cyclic voltammogram of (a) RF and (b) FMN (1 mM each, blue line) upon addition of ZnDPA (5 mM, red line) in 10 mM HEPES buffer (pH = 7.4). The reduction potential ($E_{red}°'$) was estimated from the mean of two peaks, cathodic (E_{pc}) and anodic (E_{pa}) potential. The inset yellow box is the magnified area of dotted box.

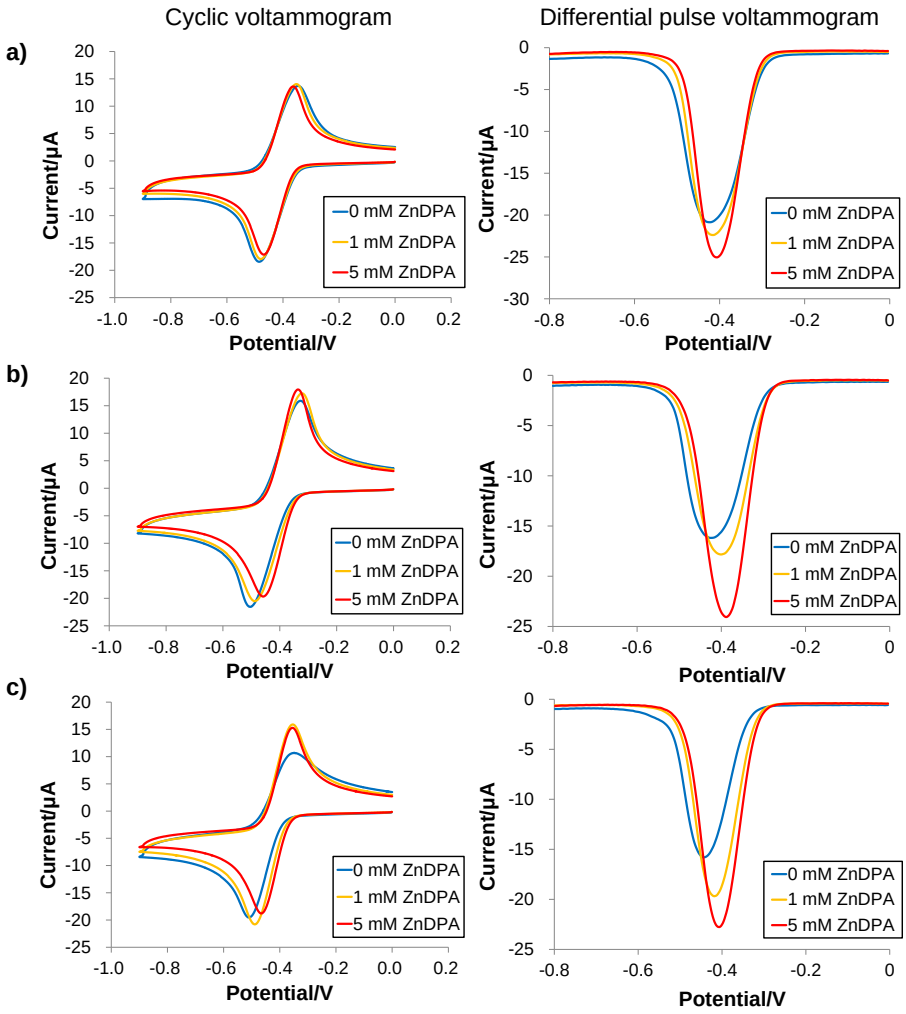

Figure 4. Cyclic voltammogram (left column, scan rate = 0.1 V/s) and differential pulse voltammogram (right column, pulse width = 0.05 s, pulse period = 0.2 s) of 1 mM RF (a), FMN (b), and FAD (c) upon the addition of ZnDPA (0−5 mM) in 10 mM HEPES buffer (pH = 7.4). The quasi-reversible reductive waves of FMN and FAD gradually shift to less negative value upon the addition of ZnDPA ($\Delta E_{red}{}^{\circ\prime}$ = 18 mV each under 5 mM addition), whereas RF exhibits no observable change in its half reduction potential. ZnDPA showed no reduction peak at the given potential range.

It is well-known that the fluorescence lifetime of a molecule is sensitive to its surrounding environment, which could be influenced by both weak intermolecular forces and intermolecular electron transfer from a nearby molecule.[17] Studies on the fluorescence lifetime of flavins, upon addition of probes, revealed much about the function of Zn^{II}-DPA moiety of **1-Zn** in flavin-mediated oxidation. The fluorescence lifetime of FAD (τ_m = 3.18 ns) was largely affected by **1-Zn** (τ_m = 2.57 ns), whereas negligible change appeared upon the addition of **2** (τ_m = 3.10 ns) under a 545−555 nm filter set (Figure 5c). **1-Zn** gave the extra quenching term of $k_e = 7.46 \times 10^7\ s^{-1}$, which was 9.2-fold enhanced rate compared to **2** ($k_e = 0.81 \times 10^7\ s^{-1}$) in the measurement of FAD lifetime (Table 4). Other cases were conducted without the [9*H*]xanthene, which could provide only the weak intermolecular forces on flavins; the addition of probes in oxidized form (**1-Zn**$_{ox}$, **2**$_{ox}$) or other compounds (ZnDPA, Zn^{II} ion) revealed a negligible lifetime change unlike the **1-Zn** addition (Figure 5f). These indicate that the extra quenching term (k_e) is mainly influenced by the intermolecular electron transfer. In this case, the Zn^{II}-DPA moiety could provide an attractive field for electron transfer.[4,7] Coexistence of ZnDPA and **2** also revealed a modest contribution to the lifetime, which shows that the electrostatic effect could be effective near a reducing agent like **1-Zn** (Figure 5 and Table 4).

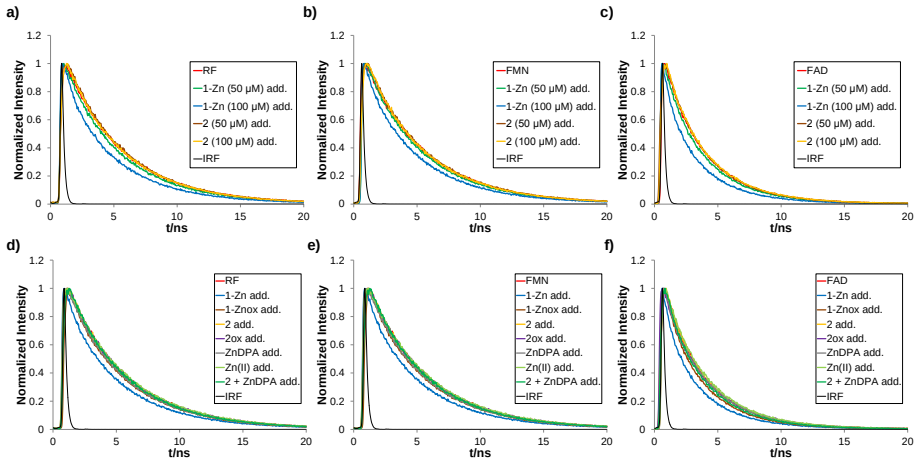

Figure 5. (a−c) Fluorescence decay curves of flavins (100 μM) upon the addition of different concentration of probes (**1-Zn** and **2**) and (d−f) varied compounds such as probes in oxidized form (**1-Zn**$_{ox}$ and **2**$_{ox}$), ZnDPA, Zn^{II}, and ZnDPA + probe **2** (100 μM each) in 3:7 THF:buffer (10 mM HEPES, pH = 7.4) upon excitation at 405 nm using pulsed diode laser and emission filter set of 545−555 nm. IRF is instrument response function curve.

Table 4. Parameters of fluorescence lifetime [a] of flavins [b] upon the addition of varied chemicals [c]

Parameters		default	**1-Zn** addition	**2** addition	**1-Zn**$_{ox}$ addition	**2**$_{ox}$ addition	ZnDPA addition	Zn^{II} addition	**2**+ ZnDPA addition [d]
RF	τ_F (ns)	4.61	4.4	4.52	4.46	4.61	4.56	4.6	4.48
	k_e [e]	-	1.04	0.43	0.73	0.0	0.24	0.05	0.63
	χ^2 [f]	1.10	1.33	1.21	1.14	1.13	1.10	1.08	1.30
FMN	τ_F (ns)	4.71	4.53	4.65	4.57	4.7	4.61	4.76	4.6
	k_e	-	0.84	0.27	0.65	0.05	0.46	N.A. [g]	0.51
	χ^2	1.11	1.32	1.23	1.19	1.12	1.14	1.04	1.04
FAD	τ_1 (ns)	2.15	1.4	1.72	1.93	1.49	1.41	2.26	1.54
	τ_2 (ns)	3.55	3.42	3.53	3.57	3.53	3.46	3.64	3.32
	τ_m [h]	3.18	2.57	3.1	2.91	3.18	3.13	3.25	2.91
	$k_{m,e}$ [i]	-	7.46	0.81	2.92	0.0	0.50	N.A.	2.92
	χ^2	1.06	1.10	1.10	1.05	1.05	1.08	1.08	1.13

[a] Time-resolved fluorescence spectroscopic data were recorded on emission filter set of 545−555 nm by excitation at 405 nm in 3:7 THF:buffer (10 mM HEPES, pH = 7.4). The measured decay curves were deconvoluted and fitted to calculate the lifetimes. The single exponential fits were applied for the decay curves of RF and FMN and the double exponential fits for those of FAD.[S2 b] [flavins] = 100 μM. The quantum yields of RF, FMN, and FAD are Φ_F = 0.43, 0.42, and 0.17 in this condition, respectively. Default values of flavins (k_r and k_D) were determined by using the parameters of Φ_F and τ_F with the equations of $\Phi_F = k_r/(k_r + k_D)$ and $\tau_F = (k_r + k_D)^{-1}$: k_r is the rate constant of radiative decay, k_D is the rate constant of non-radiative decay process. Calculated fluorescence rate constants are k_r = 9.0 ×, 8.7 ×, and 5.2 × 10^7 s^{-1} for RF, FMN, and FAD, respectively. Default values of the rate constant of non-radiative decay are k_D = 1.2 ×, 1.2 ×, and 2.5 × 10^8 s^{-1} for RF, FMN, and FAD, respectively. [c] [chemical] = 100 μM. [d] [**2**] = 100 μM, [ZnDPA] = 100 μM. [e] Extra quenching term (10^7 s^{-1}) after the addition of chemical, which is calculated from $\tau_F = (k_r + k_D + k_e)^{-1}$. [f] χ^2 is defined as the goodness of fit and should be close to 1. [g] Data is not available. In the cases, their fluorescence lifetimes were slightly increased. [h] $\tau_m = a_1 \times \tau_1 + a_2 \times \tau_2$. a_1 and a_2 are the relative contribution of τ_1 and τ_2 to the total lifetime, respectively. [i] $k_{m,e}$ (10^7 s^{-1}) = $\tau_m^{-1} - \tau_{m,\,default}^{-1}$. Although not in the physical meaning, the value of $k_{m,e}$ is considered a parameter which reflects well the decay curve changes.

Kinetic study summarized the electrostatic contribution of Zn^{II}-DPA moiety in flavin-mediated oxidation. The rate constants of **1-Zn** oxidized by RF, FMN, and FAD were 1.34-, 1.38-, and 1.47-fold larger, respectively, than that of **2** (Figure 6, Table 5). The Zn^{II}-DPA moiety of **1-Zn** promoted flavin-mediated oxidation.

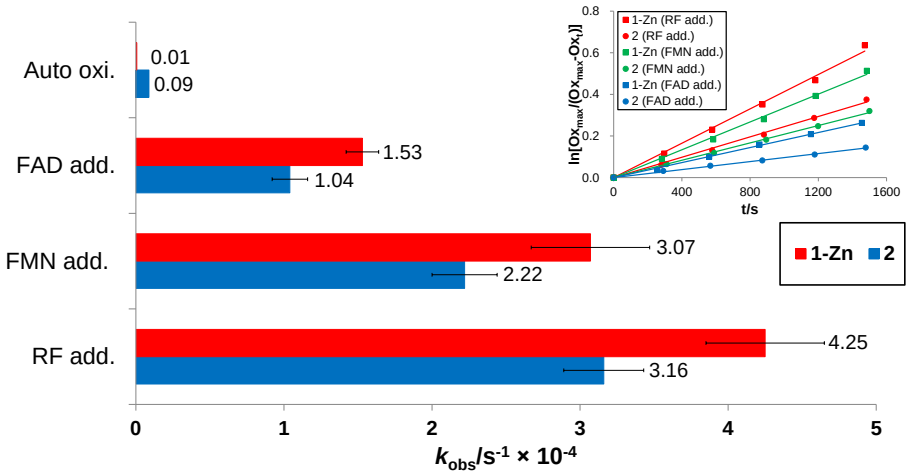

Figure 6. Bar diagram showing rate constant of **1-Zn** (red bar) and **2** (blue bar) (5 μM each) for the flavin-promoted oxidation and the auto-oxidation in 3:7 THF:buffer (10 mM HEPES, pH = 7.4) under ambient-light condition. Inset shows time-coursed plot of **1-Zn** (square) and **2** (circle) upon the addition of RF (red), FMN (green), and FAD (blue) (20 equiv. each).

Table 5. Initial rate constants [a] of **1-Zn** and **2** in the presence of flavins [c]

Probe [b]	Auto oxi.	RF add.	FMN add.	FAD add.
1-Zn	6.1×10^{-3}	4.2 ± 0.4	3.1 ± 0.4	1.5 ± 0.1
2	8.8×10^{-2}	3.2 ± 0.3	2.2 ± 0.2	1.0 ± 0.1

[a] $k_{obs}/s^{-1} \times 10^{-4}$
[b] 5 μM, 3:7 THF:buffer (10 mM HEPES, pH = 7.4).
[c] 20 equiv., Rate constants were measured at 565 nm by UV−Vis spectrometer.

2.5. Photo-physical properties of 1-Zn

The flavin-mediated oxidation of **1-Zn** was performed under an ambient-light driven condition. A solvent screening test reveals that the oxidation rate reaches maximum at 70% water content (Figure 7). Time-elapsed optical signals of **1-Zn** upon presence of 20 equiv. RF were monitored in 3:7 THF:buffer (10 mM HEPES, pH = 7.4). The increasing absorption band at 565 nm (Figure 8a) and the fluorescence intensity at 588 nm (Figure 8b) corroborate the formation of rhodamine-like structure after flavin-mediated oxidation. The rate constant of flavin-mediated oxidation of **1-Zn** is $k_{obs} = 4.25 \pm 0.40 \times 10^{-4}$ s^{-1} (half life, $t_{1/2}$ = 0.5 h), whereas auto-oxidation is approximately 3 orders slower at $k_{obs} = 6.14 \times 10^{-7}$ s^{-1} ($t_{1/2}$ = 313.8 h) under ambient-light condition (Table 6). There were no significant changes of fluorescence intensity upon treatment with excess amount of other analytes such as NAD^+, Fe^{II}, Fe^{III}, 6-biopterin, folic acid, GSSG,

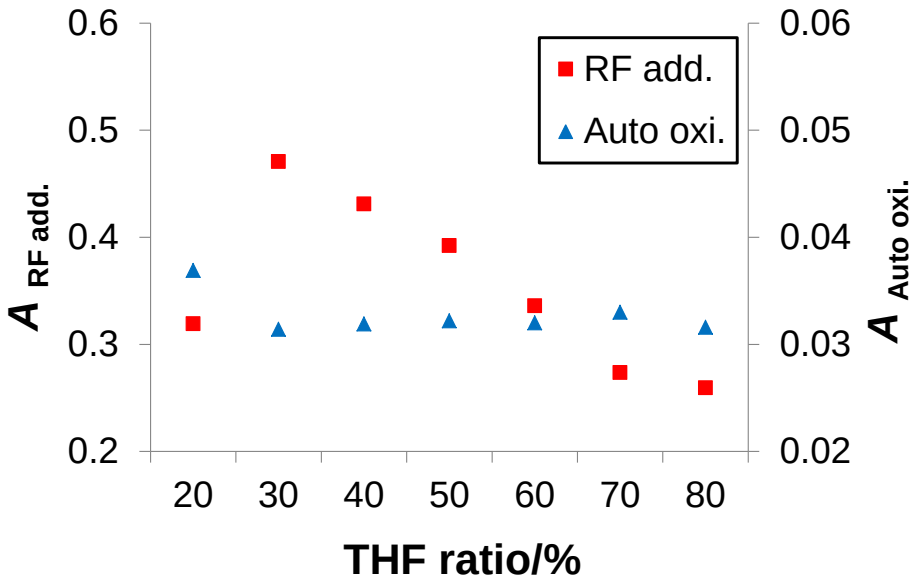

Figure 7. UV−Vis absorption intensity change (λ_{abs} = 565 nm) of **1-Zn** (5 μM) in THF:buffer (10 mM HEPES, pH = 7.4) upon absence (blue triangle) and presence of RF (20 equiv., red square). THF:buffer co-solvent was prepared in a range of 1:4−4:1 ratio. The UV−Vis absorbance was measured after aging for 2 h.

H_2O_2, OCl^-, $O_2^{\bullet-}$, $^{\bullet}OH$, and pyrophosphate (PPi) (Figure 9). The selective response of **1-Zn** toward flavins is mainly owing to its strong electron accepting ability. Moreover, the well-known biological photo-oxidants 6-biopterin and folic acid displayed much weaker oxidation abilities toward **1-Zn**.[18] The UV−Vis absorption intensity (λ_{max} = 565 nm) corroborates evidence for the selectivity of **1-Zn** toward flavins (Figure 9 inset). Competitive selectivity experiments (Figure 10) and colorimetric changes (Figure 11) give further evidence of high selectivity toward flavins. The impressive color change of **1-Zn** from colorless to reddish-brown is attributable to the adopted rhodamine-like structure. In dark conditions, the flavin-promoted oxidation rate of **1-Zn** (k_{obs} = 9.13 × 10^{-7} s^{-1}, $t_{1/2}$ = 210.9 h) is similar with the ambient-light driven

auto-oxidation rate (Figure 12). When the reaction mixture was subjected to UV lamp irradiation (Spectroline, ENF-260C, λ_{irr} = 365 nm, 6 W), the rate

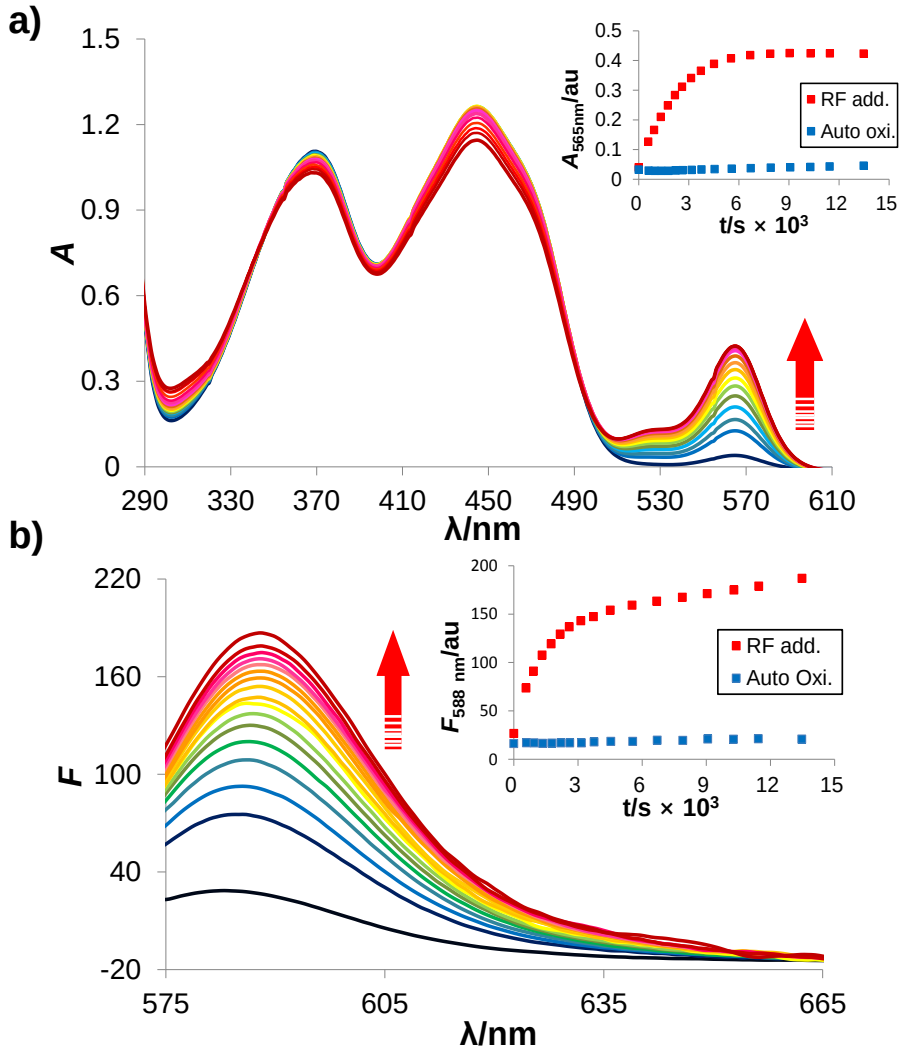

Figure 8. (a) Time-coursed UV−Vis absorption (a) and fluorescence (b) spectra of **1-Zn** (5 μM) upon the addition of RF (20 equiv.) in 3:7 THF:buffer (10 mM HEPES, pH = 7.4). The inset shows the absorption (panel a, λ_{abs} = 565 nm) and the fluorescence intensities (panel b, λ_{em} = 588 nm, λ_{ex} = 565 nm) of **1-Zn** (blue square) and those of accompanied with RF (red square).

constant was enhanced to k_{obs} = 3.67 × 10^{-3} s^{-1} ($t_{1/2}$ = 3.15 m). RF was also quantified in submicromolar concentration (0−1.0 μM), resulting in the detection limit of 7 × 10^{-8} M, which is sufficiently sensitive for biological applications (Figure 14). **1-Zn** worked in a broad pH range from 4.83 to 9.66 (Figure 13).

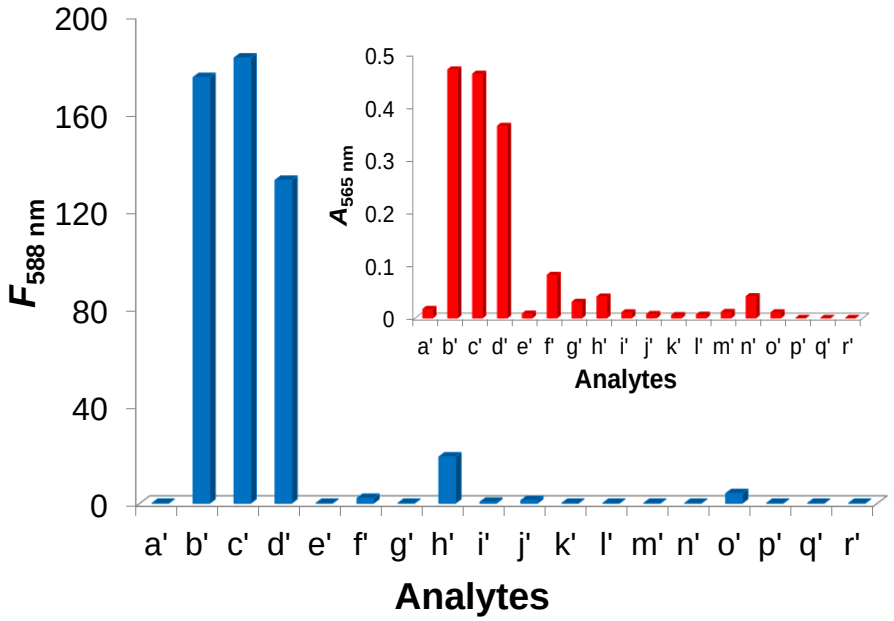

Figure 9. The bar diagram showing change in the fluorescence intensity of **1-Zn** in the presence of control (a'), RF, FMN, FAD (20 equiv.) (b'−d'), NAD^+, Fe^{II}, Fe^{III}, 6-biopterin, folic acid (100 equiv.) (e'−i'), GSSG (262 equiv.) (j'), H_2O_2, OCl^- (100 equiv.) (k'−l'), $O_2^{\bullet-}$ (560 equiv.) (m'), $OH^{\bullet}$, PPi (100 equiv.) (n'−o'). There are no fluorescent emission of RF, FMN, FAD (100 μM each) upon 565 nm excitation (p'−r'). The inset shows the corresponding absorption intensities (λ_{abs} = 565 nm) of **1-Zn**. The mixtures were shaken for 2 h at RT.

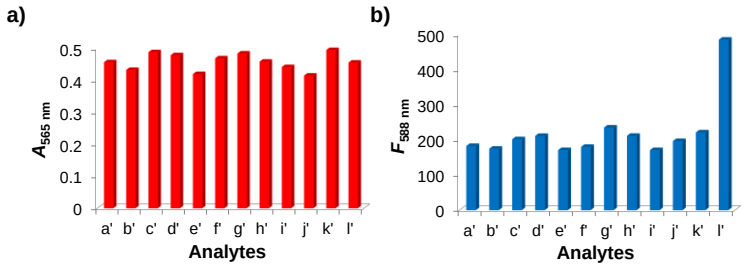

Figure 10. The bar diagram showing UV−Vis absorbance (a) and fluorescent response (b) of **1-Zn** (5 μM) to RF (20 equiv.) in the co-presence of different analytes: control (a'), NAD^+, Fe^{II}, Fe^{III}, 6-biopterin, folic acid (100 equiv.) (b'−f'), GSSG (262 equiv.) (g'), H_2O_2, OCl^- (100 equiv.) (h'−i'), $O_2^{\bullet-}$ (560 equiv.) (j'), $OH^{\bullet}$, PPi (100 equiv.) (k'−l'). After the addition of RF, various mixtures were shaken for 2 h at RT. DATA were acquired in 3:7 THF:Buffer (HEPES 10 mM, pH = 7.4). The excitation wavelength was 565 nm.

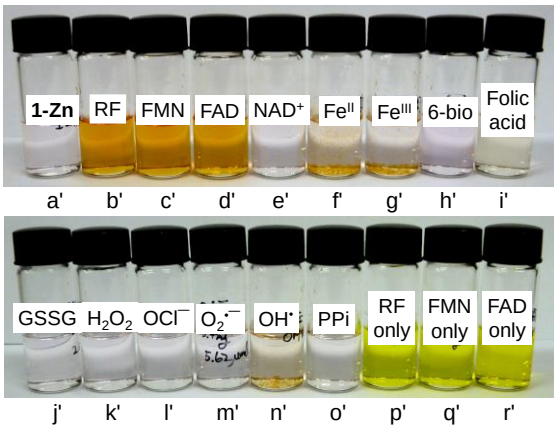

Figure 11. Change in color of **1-Zn** (5 μM) in the presence of different analytes in 3:7 THF:Buffer (HEPES 10 mM, pH = 7.4); **1-Zn** only (a'), RF, FMN, FAD (20 equiv.) (b'−d'), NAD^+, Fe^{II}, Fe^{III}, 6-biopterin, folic acid (100 equiv.) (e'−i'), GSSG (262 equiv.) (j'), H_2O_2, OCl^- (100 equiv.) (k'−l'), $O_2^{\bullet-}$ (560 equiv.) (m'), $^{\bullet}OH$, PPi (100 equiv.) (n'−o'), RF, FMN, FAD only (100 μM each) (p'−r'). After the addition of analytes, the mixtures were shaken for 2 h at RT.

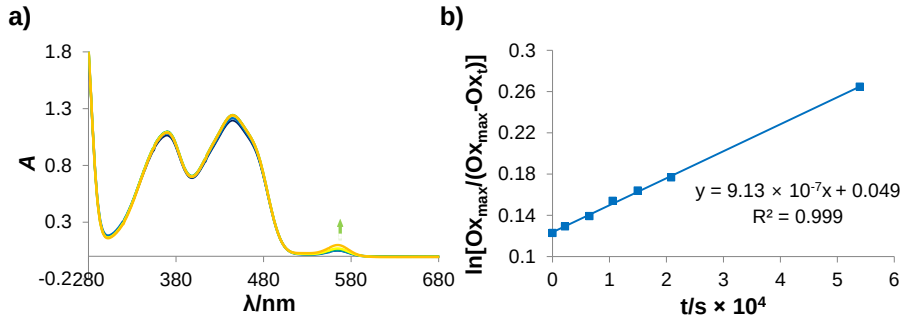

Figure 12. Flavin-promoted oxidation under dark condition. Time-coursed UV−Vis absorption spectra of **1-Zn** (5 μM) in the presence of RF (20 equiv.) (a) and its corresponding intensity at 565 nm in 3:7 THF:buffer (10 mM HEPES, pH = 7.4) (b). The rate constant was calculated to be k_{obs} = 9.13 × 10^{-7} s^{-1}.

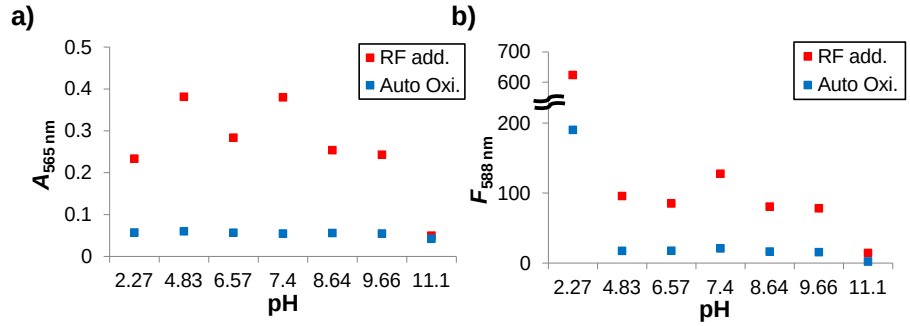

Figure 13. pH profiles showing change in UV−Vis absorbance (a) and fluorescence intensity (b) of **1-Zn** (5 μM) in the absence (blue square) and presence of RF (20 equiv., red square) in 1:1 THF:DI-water. The pH screening was performed in a range of 2.27−11.1. UV−vis absorption (λ_{abs} = 565 nm) and fluorescence emission (λ_{em} = 588 nm, λ_{ex} = 565 nm) were measured after aging for 2 h.

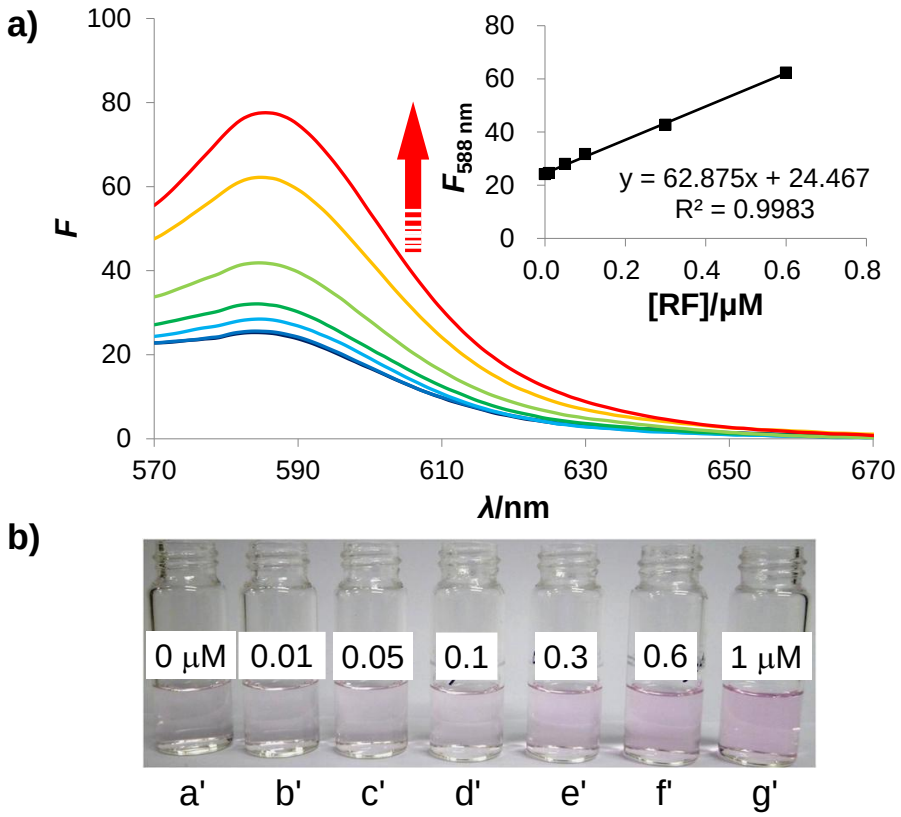

Figure 14. Fluorescence spectra of **1-Zn** (5 μM) in presence of varied concentration of RF (0−1.0 μM) in 3:7 THF:buffer (10 mM HEPES, pH = 7.4) (a) and their corresponding color change of **1-Zn** (b). The fluorescence was measured at 588 nm with excitation at 565 nm after shaking for 2 h. Inset shows linear plot of fluorescence intensity at lower concentration of RF (0−0.6 μM). Detection limit was determined to be 74.6 nM from 3σ/m in which σ is the standard deviation of background signal (n = 3) and m is the slope of linear plot.

2.5. HPLC study

The progress of flavin-promoted oxidation was examined using an analytical and preparative HPLC/UV−Vis spectrometer. The initial peak at τ = 6.7 min decreases with the concomitant generation of two new peaks at τ = 6.1 and 10.7 min. The peak at τ = 10.7 min is characterized by preparative HPLC/HRMS at **1**$_{ox}$ (m/*z* calculated for $C_{49}H_{48}N_5O_4$ 770.3706, observed 770.3695).[19] The increasing peak of λ_{abs} = 565 nm at the τ = 10.7 min also provides evidence for the formation of rhodamine-like structure. A well-known method identifies the peak at τ = 6.1 min as RFH_2 from reduction of RF by NADH, which shows the retention time similar with the result conducted by **1-Zn** and RF (Figures 15

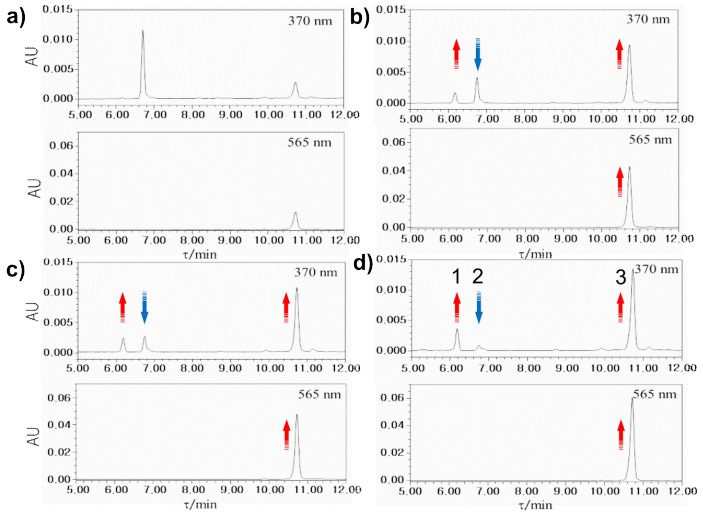

Figure 15. Time-coursed partial spectra of HPLC/UV−Vis experiment (top: λ_{abs} = 370 nm, bottom: λ_{abs} = 565 nm). **1-Zn** (10 μM) was mixed with RF (5 equiv.) in 1:1 THF:buffer (10 mM HEPES, pH = 7.4), and monitored after 0 h (a), 2.0 h (b), 3.0 h (c), 4.8 h (d). Labels on panel (d) show RF_{red} (1), **1-Zn** (2), and **1-Zn**$_{ox}$ (3), respectively.

and 16).[20]

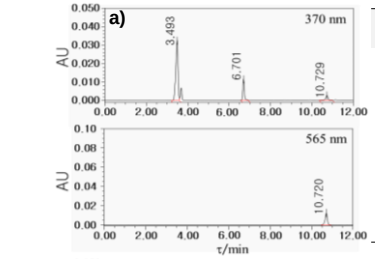

	τ/min	Area	Height
RF_2	3.493	245871	32788
RFH_2	6.166	817	149
1-Zn	6.701	60881	11386
1-Zn$_{ox}$ at 370 nm	10.729	21322	2706
1-Zn$_{ox}$ at 565 nm	10.720	95641	12475

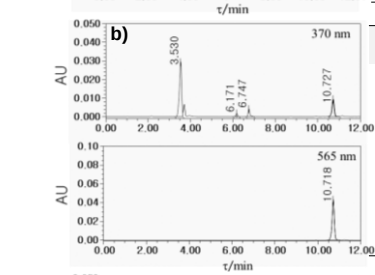

	τ/min	Area	Height
RF_2	3.530	217456	29417
RFH_2	6.171	9647	1722
1-Zn	6.747	24124	4152
1-Zn$_{ox}$ at 370 nm	10.727	67829	9371
1-Zn$_{ox}$ at 565 nm	10.718	308842	42810

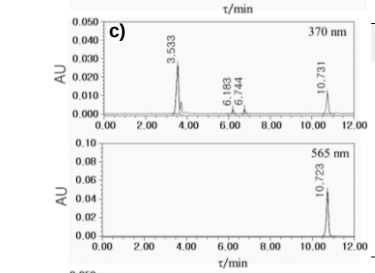

	τ/min	Area	Height
RF_2	3.533	200628	26218
RFH_2	6.183	12831	2288
1-Zn	6.744	13578	2539
1-Zn$_{ox}$ at 370 nm	10.731	75223	10629
1-Zn$_{ox}$ at 565 nm	10.723	337384	48118

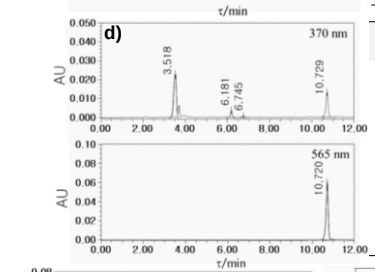

	τ/min	Area	Height
RF_2	3.518	203882	22840
RFH_2	6.181	20001	3558
1-Zn	6.745	4375	804
1-Zn$_{ox}$ at 370 nm	10.729	97286	13288
1-Zn$_{ox}$ at 565 nm	10.720	442882	60356

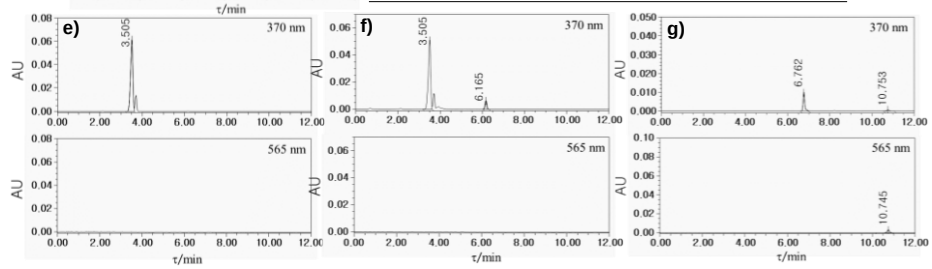

Figure 16. HPLC/UV−Vis full spectra (top line: 370 nm, bottom line: 565 nm) of **1-Zn** (10 μM) (a) after aging for 2 h (b), 3 h (c), 4.8 h (d) in the presence of RF (5 equiv.) in 1:1 THF:Buffer (HEPES 10 mM, pH 7.4), and their corresponding values. Panels (e−g) show RF (50 μM) (e), in presence of NADH (5.6 equiv.) after aging for 3.0 h (f), and **1** (10 μM) (g).

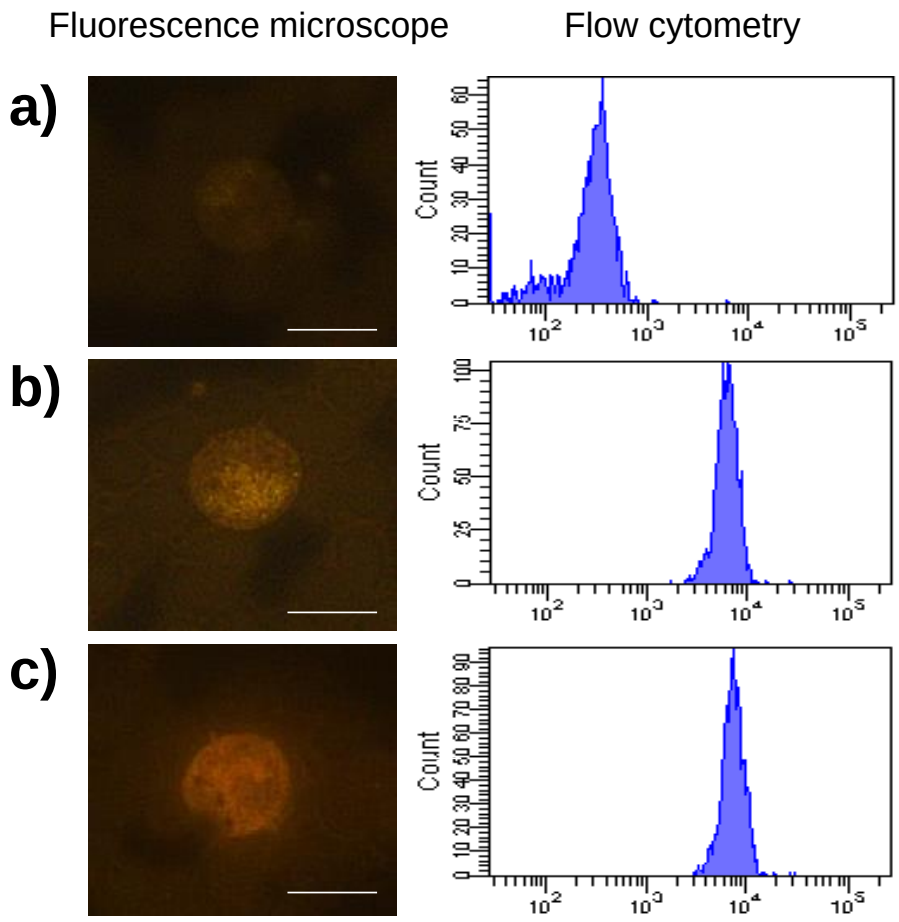

Figure 17. Fluorescence microscope images (left column) and its histograms (right column). Eosinophils were treated with three working solutions of diluent only (a), **2** (b), and **1-Zn** (c) in 3:7 THF:buffer (×1 saline-sodium citrate (SSC), pH = 7.4), followed by incubation for 20 min. The treated concentration of **2** and **1-Zn** was 5 μM. Mean fluorescence intensities (MFIs) were measured by gathering emissions of 564−606 nm with excitation at 488 nm (Argon-ion laser). MFIs are 295 (a), 6355 (b), and 7588 (c), respectively. Scale bar = 10 μm.

2.6. Imaging of eosinophils and differential diagnosis of eosinophilia.

Finally, **1-Zn** and **2** are successfully utilized in eosinophils imaging (*i.e.*, FAD-

rich cell).[12] Eosinophils show weak fluorescence in the absence of probes owing to the autofluorescence of FAD, but show bright red fluorescence upon the administration of **1-Zn** and **2**. The *x*-axis in flow cytometry histograms corroborates the increased fluorescence intensity caused by oxidation. All experiments were performed without a washing step, and **1-Zn** was found to be photo-stable during the cellular imaging experiments. Eosinophils stained with **2** emit weaker fluorescence intensity than those stained with **1-Zn** (Figure 17). Electrostatically favorable **1-Zn** is more practical than **2** for monitoring biologically active flavins.

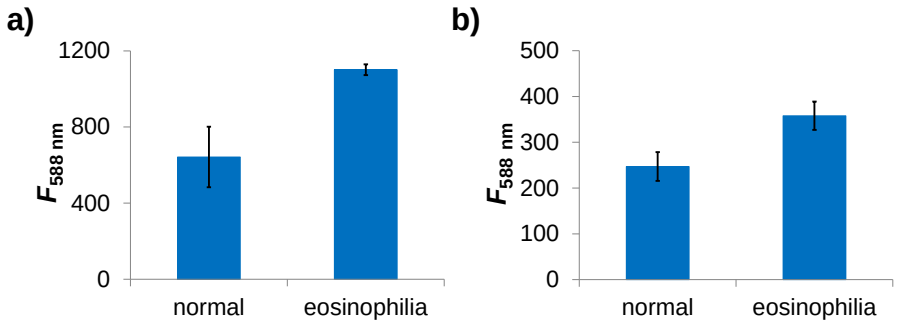

Figure 18. Fluorescence intensity of **2** (a) and **1-Zn** (b) (10 μM) in treated cell lysate solutions (42:98:60 lysate:buffer:EtOH, v/v, ×1 SSC buffer, pH = 7.4). Eosinophils account for 0.5−0.9% (normal sample) and 9.0−9.3% (eosinophilia sample) of leukocytes. Fluorescence emission was measured at 588 nm with excitation at 555 nm (cutoff: 570 nm) after shaking for 3 h. Four sets of each normal and eosinophilia human blood samples were tested in triplicates and then averaged. Averages with standard deviations are displayed.

1-Zn also showed a linear detection range (0−10 μM) upon addition of FAD, which shows **1-Zn** is able to detect FAD in diluted human serum (Figure 19). The *x*-intercept in Figure 19 shows the concentration of flavins in the original

sample solution, which is determined at 2×10^{-6} M. According to the previous reports, flavins cellular concentration, especially under varied physiological conditions is in a range of nanomolar to micromolar.[11,13a]

More importantly, eosinophilia samples (*i.e.*, eosinophils account for 9.0, 9.0, 9.3, 9.3% of leukocytes) are differentially diagnosed from normal samples (*i.e.*, eosinophils account for 0.5, 0.8, 0.8, 0.9% of leukocytes) with distinguishable fluorescence intensity that is allowed from **2** and **1-Zn** in cell lysate (Figure 18). These studies demonstrate the utility of the probe as suitable tools for flavin-linked studies in cells as well as human serum.

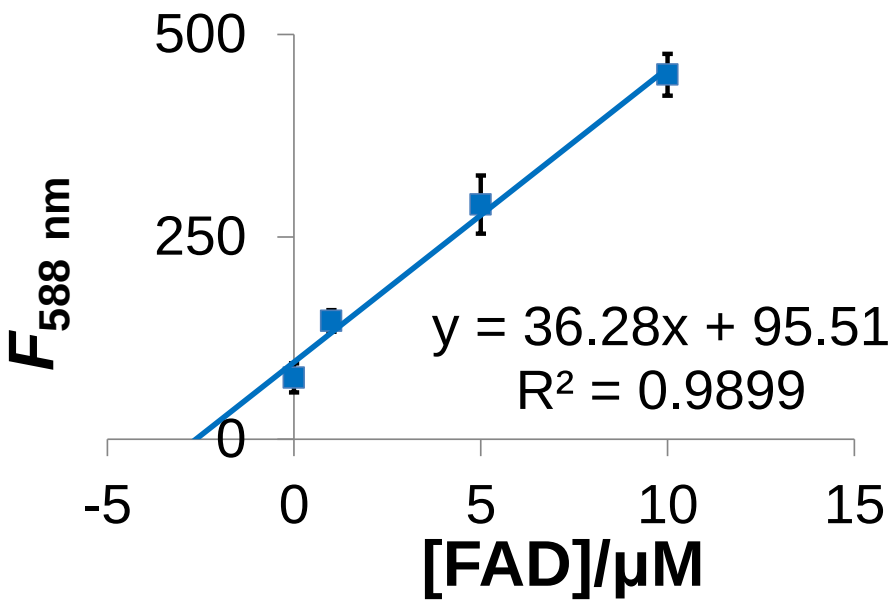

Figure 19. Fluorescence intensity change of **1-Zn** (5 μM) upon standard addition (FAD, 0−10 μM) in diluted human serum solution (12:7:21 EtOH:serum:buffer, ×1 SSC buffer, pH = 7.4). The fluorescence was measured at 588 nm with excitation at 555 nm after shaking for 3 h. The samples were tested in triplicates and averaged.

3. Conclusion

The electrostatic modification of the probe was simply performed by introduction of DPA on the coumarin. After Zn^{II} binding, the induced electrostatic force on the coumarin stabilized the vicinal [9*H*]xanthene ring, thereby lowering the driving forces for the auto-oxidation of **1-Zn**. The positive charge on the Zn^{II}-DPA moiety of **1-Zn** also promoted flavin-mediated oxidation, providing a favorable electrostatic environment for the reduction of isoalloxazine. Finally, **1-Zn** was applied to varied flavin-linked studies such as eosinophils imaging and differential diagnosis of eosinophilia using human blood cell lysate.

4. Experimental

4.1. General procedure

All fluorescence and UV−Vis absorption spectra were recorded by Jasco FP 6500, multimode plate reader (Molecular Devices, SpectraMax M2e), and Beckman coulter DU 800 spectrophotometers. All ^{1}H and ^{13}C NMR spectra were collected in deuterated solvent, and recorded on Bruker 300 and Varian 400 MHz spectrometer. All chemical shifts are reported in ppm value using the peak of residual proton signals of TMS as internal reference. DFT calculations were performed by B3LYP/6-31G level using program "Gaussian 09". HRMS data received directly from the Korea Basic Science Institute. The fluorescence imaging of cells was performed with fluorescence microscope (BX51, Olympus, Japan). The mean fluorescence intensities (MFIs) were measured using flow cytometer (FACSCantoII. Becton Dickinson, San Jose, USA) with FACSDiva program. HPLC analysis was performed on HECTOR-M C18 column (4.6 ×

150 mm, RS tech.) using HPLC system composed of binary HPLC pump (Waters 1525) and UV−Vis detector (Waters 2489). Semi-preparative HPLC was performed on HECTOR-M C18 column (21.2 × 150 mm, RS tech.). Cyclic voltammetry (CV) and differential pulse voltammetry (DPV) experiments were conducted with computer-controlled CH Instruments 660 Electrochemical Analyzer (CH Instruments, Inc., TX, USA). A time-correlated single photon counting (TCSPC) board (SPC-150, Becker & Hickl, Berlin, Germany) was used to measure the time-resolved fluorescence decay using 405 nm picosecond pulsed diode laser (LDH-P-C-405, Picoquant, Berlin, Germany). The emission wavelength 550 ± 5 nm of each flavin was extracted by using a bandpass filter (FB55010, Thorlabs Inc., Newton, NJ, USA). All analytes were purchased from Aldrich and TCI, and used as received. All solvents were analytical reagents from Duksan Pure Chemical Co., Ltd. The DMSO and THF for spectra detection was of HPLC reagent grade, without fluorescent impurity. De-ionized water was used in all studies.

4.2. Synthetic procedure

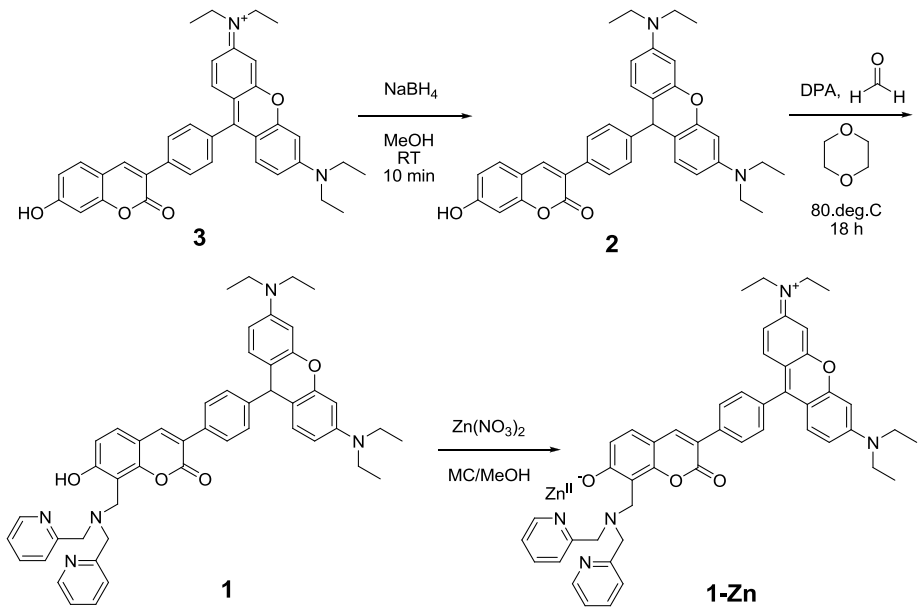

Scheme 3. Syntheses of probes **1**, **2**, and **1-Zn**

Synthesis of 2.To solution of compound **3** in MeOH was added excess amount of $NaBH_4$, and stirred for 10 min. The volatile solvent was evaporated under reduced pressure, and the resultant was purified by flash column chromatography with 50:1 MC:MeOH (v/v) as eluent. The column fractions were collected and solvent was removed under reduced pressure. The residue was further crystalized with MeOH, and then resulting solid was filtered to give light violet solid powder (56% yield). All processes were conducted within 1 h to minimize air-oxidation. Any detectable auto-oxidation was not observed in the solid state at least 2 years at room temperature. ^{1}H NMR (DMSO-d_6, 300 MHz) δ (ppm): 10.59 (s, 1H), 8.06 (s, 1H), 7.56−7.53 (m, 3H), 7.19 (d, J = 8.1 Hz, 2H), 6.85−6.78 (m, 3H), 6.73 (s, 1H), 6.36−6.33 (m, 4H), 5.08 (s, 1H), 3.29 (m, 8H, peaks were embedded in H_2O peak region), 1.09 (t, J = 6.9 Hz, 12H). ^{13}C NMR ($CDCl_3$, 75 MHz) δ (ppm): 161.8, 159.9, 154.9, 152.1, 148.5, 147.6,

140.4, 132.6, 130.4, 129.2, 128.5, 123.9, 113.8, 113.2, 111.8, 107.7, 102.8, 98.9, 77.2, 44.5, 42.6, 12.6. HRMS (FAB^+, m-NBA) *m/z* calculated for $C_{36}H_{36}N_2O_4$ 560.2675, observed 560.2670.

Synthesis of 1. To solution of formaldehyde (35% aqueous solution, 30 mg, 0.34 mmol) in 1,4-dioxane (1.5 mL) was slowly added 2,2´-dipicolylamine (47.82 mg, 0.24 mmol), and the reaction mixture was stirred for 6 h at RT. **2** (112 mg, 0.2 mmol) was then added to the stirred solution, and additional 0.5 mL of 1,4-dioxane was added. The mixture was stirred for 12 h at 70°C. The solvent was removed under reduced pressure, and the resulting mixture was purified by flash column chromatography with 50:1 MC:MeOH (v/v) as eluent. After evaporation of volatile solvent in vacuo, light violet crumbly solid was appeared in 81% yield. All purification processes were conducted within 1 h to minimize air-oxidation. Any detectable auto-oxidation was not observed in the solid state at least 2 years at room temperature. ^{1}H NMR (acetone-d_6, 300 MHz) δ (ppm): 8.56 (d, J = 4.5 Hz 2H), 7.95 (s, 1H), 7.77 (t, J = 7.5 Hz, 2H), 7.66 (d, J = 8.1 Hz, 2H), 7.49−7.44 (m, 3H), 7.29−7.25 (m, 4H), 6.91 (d, J = 9.0 Hz, 2H), 6.85 (d, J = 8.4 Hz, 2H), 6.40−6.38 (m, 4H), 5.12 (s, 1H), 4.10 (s, 2H), 4.05 (s, 4H), 3.42 (q, J = 6.9 Hz, 8H), 1.17 (t, J = 6.9 Hz, 12H). ^{13}C NMR (acetone-d_6, 75 MHz) δ (ppm): 162.1, 159.9, 158.2, 153.4, 152.1, 148.8, 148.7, 147.7, 140.6, 136.8, 133.3, 130.3, 128.6, 128.4, 127.8, 123.1, 122.3, 113.9, 111.9, 111.7, 109.9, 107.5, 98.4, 58.6, 47.4, 44.0, 42.4, 12.0. HRMS (FAB^+, m-NBA) *m/z* calculated for $C_{49}H_{50}N_5O_4$ 772.3863, observed 772.3866.

Synthesis of 1-Zn. To solution of **1** (13.9 mg, 18 μmol) in methylene chloride (0.5 mL) was added solution of $Zn(NO_3)_2{\cdot}6H_2O$ (5.89 mg, 19.8 μmol) in MeOH (0.5 mL). The mixture was stirred for 30 min at RT. The solvent was evaporated, and the residue was collected to obtain the desired product **1-Zn** without further

purification (light reddish solid, quantitative yield). ^{1}H NMR (acetone-d_6, 300 MHz) δ (ppm): 8.77 (d, J = 4.8 Hz 2H), 8.17 (t, J = 7.5 Hz 2H), 7.94 (s, 1H), 7.73−7.65 (m, 6H), 7.44 (d, J = 8.1 Hz 1H), 7.30 (d, J = 7.8 Hz 2H), 7.05 (br, 2H), 6.79 (d, J = 8.4 Hz, 1H), 6.65 (br, 4H), 5.26 (s, 1H), 4.56 (s, 1H), 4.51 (s, 1H), 4.29−4.26 (m, 2H), 4.10−4.06 (m, 2H), 3.49 (br, 8H), 1.19 (t, J = 6.9 Hz, 12H). HRMS (FAB^{+}, m-NBA) *m/z* calculated for $C_{49}H_{48}N_6O_7Zn$ 896.2876, observed 896.2866.

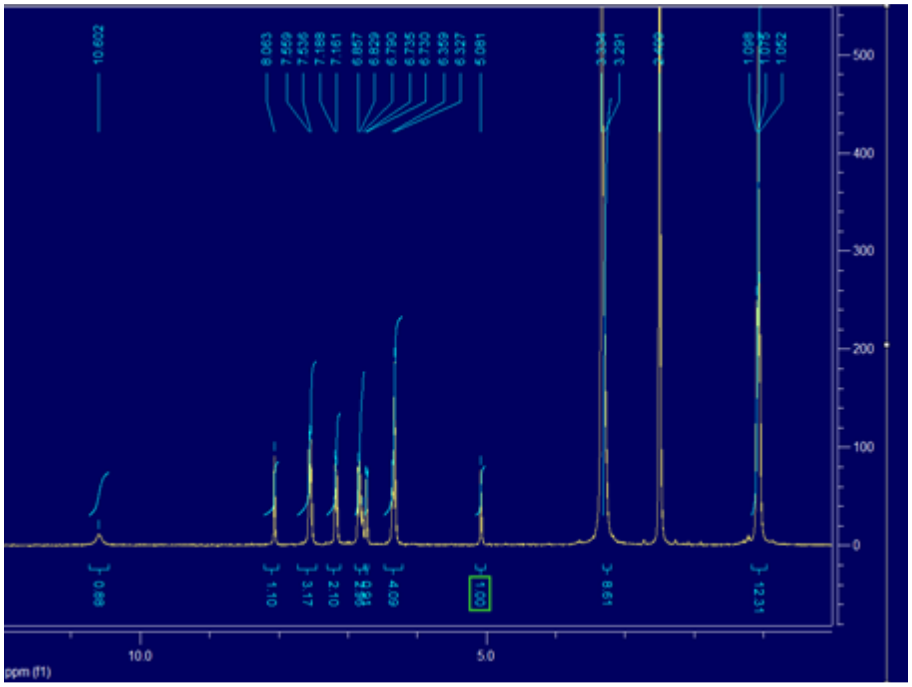

Figure 20. ^{1}H-NMR spectrum of **2**

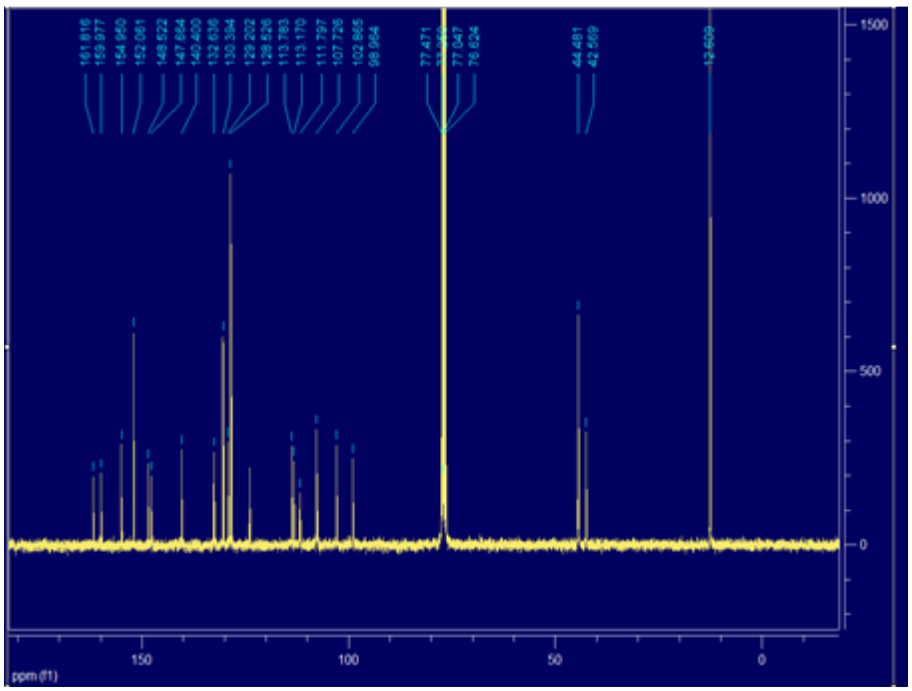

Figure 21. ^{13}C-NMR spectrum of **2**

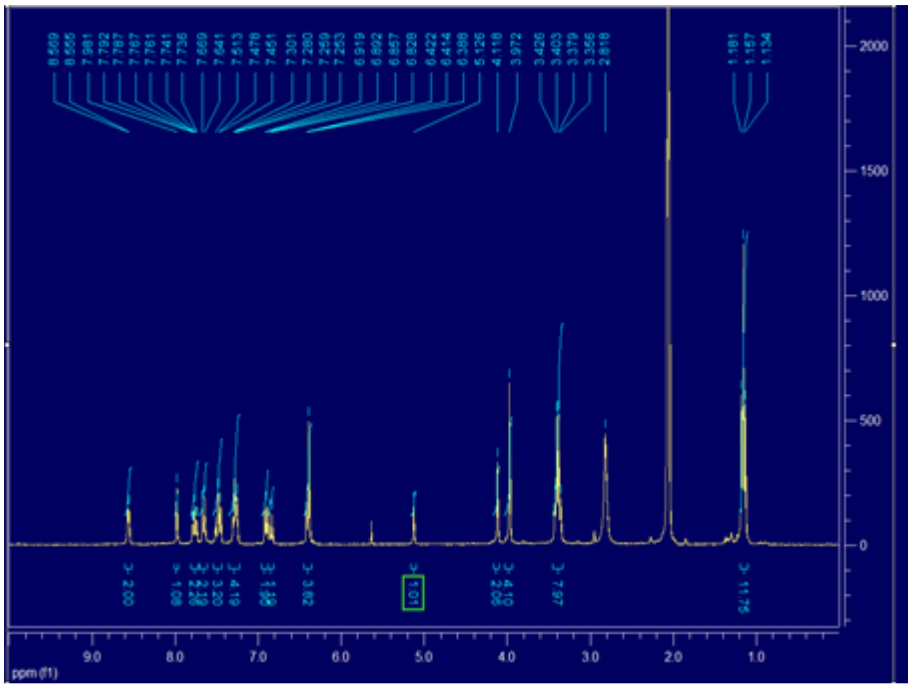

Figure 22. ^{1}H-NMR spectrum of **1**

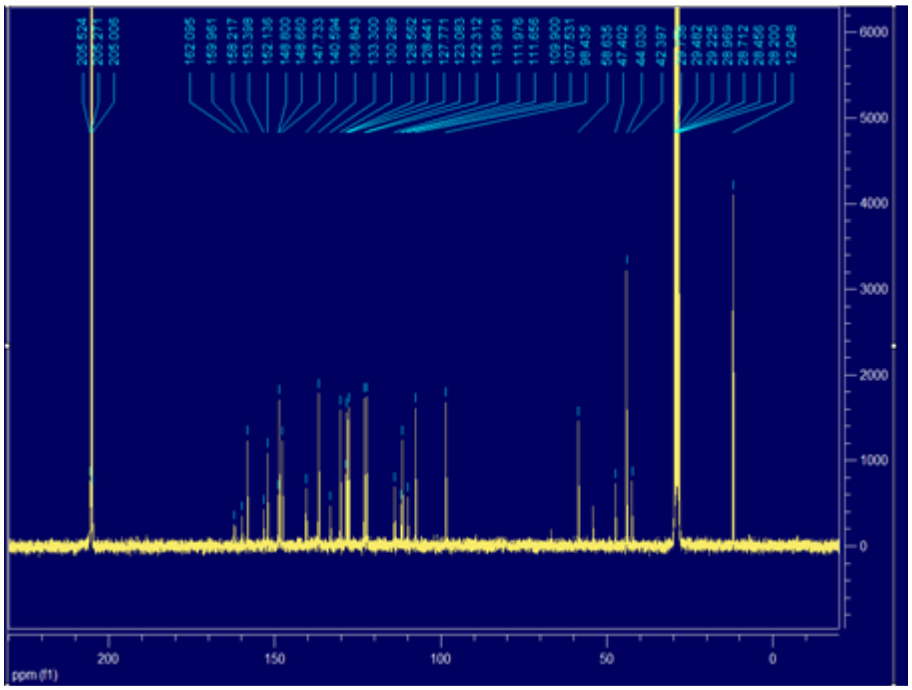

Figure 23. ^{13}C-NMR spectrum of **1**

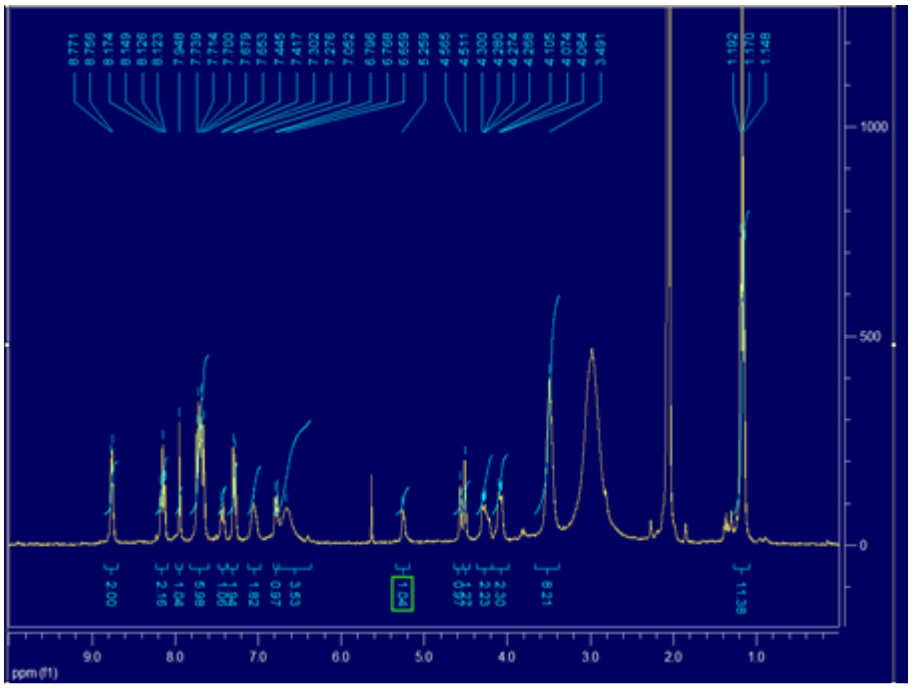

Figure 24. ^{1}H-NMR spectrum of **1-Zn**

4.3. Determination of reaction rate constant (*k*)

For auto-oxidation,

$$A \xrightarrow{k_1} C$$

$$-\frac{d[A]}{dt} = k_1[A]$$

$$-\int_{[A]_0}^{[A]_t} \frac{d[A]}{[A]} = \int_0^t k_1 \, dt$$

$$\ln \frac{[A]_0}{[A]_t} = k_1 t$$

For flavin-promoted oxidation,

$$A + B \xrightarrow{k_2} C$$

$$-\frac{d[A]}{dt} = k_2[A][B]$$

$$-\frac{d[A]}{dt} = k_{obs}[A] \qquad \because \text{ [B] = constant concentration}$$

$$-\int_{[A]_0}^{[A]_t} \frac{d[A]}{[A]} = \int_0^t k_{obs}\, dt$$

$$\ln \frac{[A]_0}{[A]_t} = k_{obs} t$$

For unimolecular reaction, $[A]_t + [C]_t = [C]_{max}$

$$k_x t = \ln \frac{[A]_0}{[A]_t} \approx \ln\left(1 + \frac{C_t}{C_{max} - C_t}\right) \qquad (x = 1 \text{ or obs}) \qquad (1)$$

In our case,

$[A]_t$ = concentration of probes (**1**, **2**, and **1-Zn**) unreacted after time elapse of 't' sec

[B] = concentration of flavins (RF, FMN, and FAD)

$[C]_t$ = concentration of probes in oxidized form after time elapse of 't' sec

$[C]_{max}$ = maximum concentration of probes in oxidized form

A_t, C_t, and C_{max} are UV−Vis absorbance (λ_{abs} = 565 nm) or fluorescence intensity (λ_{em} = 600 nm) of $[A]_t$, $[C]_t$, and $[C]_{max}$, respectively.

Using equation (1), the initial rate constants were calculated under ambient-light condition as tabulated in **Table 1 and 5**.

4.4. Kinetic study

Auto-oxidation. Kinetic study for auto-oxidation was performed with 1 μM of probes (**1**, **2**, and **1-Zn**) in 4:6 ACN:buffer (10 mM HEPES, pH = 7.4) under ambient light condition. The solvent condition was determined by considering two factors of solubility and the oxidation rate. The solvent condition of 3:7 THF:buffer (10 mM HEPES, pH = 7.4) showed too much slow auto-oxidation to sense the signal change in UV−Vis absorbance or fluorescence emission. The rate constant was measured under 1st order reaction kinetics and derived at 298, 318, and 333 K by using multimode plate reader (Molecular Devices, SpectraMax M2e). Eyring equation allowed to get kinetic parameters ($\Delta H^{\ddagger}$, $\Delta S^{\ddagger}$, and $\Delta G^{\ddagger}$) of the probes on the auto-oxidation.

***Flavin-promoted oxidation*.** To solution of probes (5 μM, 2 mL), 20 μL of 10 mM stock solutions of flavins (RF, FMN, FAD) were added, and monitored by using UV−Vis spectrometer (Beckman coulter DU 800) under ambient-light condition. The experiment was performed in 3:7 THF:buffer (10 mM HEPES, pH = 7.4) in which the auto-oxidation was minimized. Rate constant was measured under pseudo-1st order reaction condition, because flavin in reduced form rapidly returns to its original form, thereby the flavin concentration is remained.

4.5. Photo-physical properties of 1-Zn

Stock solution of **1-Zn** was diluted to 5 μM in 3:7 THF:buffer (10 mM HEPES, pH = 7.4). Time-dependent absorbance and fluorescence changes of **1-Zn** in the presence of RF (20 equiv.) were monitored by UV−Vis spectrometer (λ_{abs} = 565 nm, Beckman coulter DU 800) and fluorescence spectrometer (λ_{ex} = 565

nm, λ_{em} = 588 nm, Jasco FP 6500). For the selectivity and competitive selectivity experiments, varied analytes were prepared as shown in Table 6.

Table 6. Preparation of stock solutions and working solutions of **1-Zn** and various oxidants

Stock and working solutions	Preparation	Stoichio-metry to **1-Zn**
5 mM of **1-Zn** stock solution	2 μmole of **1-Zn** in 0.4 mL of THF	
5 μM of **1-Zn** working solution	1000-fold dilution in 3:7 THF:buffer (HEPES 10 mM, pH = 7.4)	
RF, FMN, FAD	20 μL of 10 mM flavins stock solution into 2 mL of 5 μM **1-Zn** solution	20 equiv.
NAD^+, 6-biopterin, folic acid	100 μL of 10 mM each stock solution into 2 mL of 5 μM **1-Zn** solution	100 equiv.
Fe^{II}, Fe^{III}, H_2O_2, OCl^-, PPi	10 μL of 100 mM each stock solution into 2 mL of 5 μM **1-Zn** solution	100 equiv.
$O_2^{\bullet-}$ [a]	0.4 mg of KO_2 as solid into 2 mL of 5 μM **1-Zn** solution	560 equiv.
GSSG [a]	1.6 mg of GSSG as solid into 2 mL of 5 μM **1-Zn** solution	262 equiv.
$^{\bullet}OH$ [b]	10 μL of 100 mM Fe^{II} stock solution into 2 mL of 500 μM H_2O_2 solution, following by addition of 2 μL of 5 mM **1-Zn** stock solution	20 equiv.

[a] The reagent was added as solid into 5 μM **1-Zn** solution.
[b] $^{\bullet}OH$ was prepared by the method of Fenton's reagent.

4.6. HPLC analysis.

HPLC analysis was performed on HECTOR-M C18 column (4.6 × 150 mm, RS tech.) using HPLC system composed of binary HPLC pump (Waters 1525) and UV−Vis detector (Waters 2489). Eluent flow rate was determined to be 1 mL/min with the following mobile phase condition: from 1:9 CH_3CN:CF_3COOH_{aq} (0.1%) at 0 min to 9:1 CH_3CN:CF_3COOH_{aq} (0.1%) at 20 min, gradient. Semi-preparative HPLC was performed on HECTOR-M C18 column (21.2 × 150 mm, RS tech.) with 7 mL/min of eluent flow rate. The obtained fractions were collected, processed in basic work-up, and injected into high resolution mass spectrometer (HRMS).

4.7. Electrochemical study.

All solutions for electrochemical experiments were prepared in aqueous buffered condition (10 mM HEPES, pH = 7.4). Each working solution of flavins (1 mM) was mixed with ZnDPA (0−5 mM), after deoxygenated by purging with high purity N_2 gas at RT. Cyclic voltammetry (CV) and differential pulse voltammetry (DPV) experiments were conducted with computer-controlled CH Instruments 660 Electrochemical Analyzer (CH Instruments, Inc., TX, USA). Glassy carbon working electrode (3.0 mm dia.) was used after polishing with porous alumina (Buehler, IL, USA) on a felt pad following sonication for 5 min in 1:1 mixed solution of deionized water and absolute ethanol, and then applied in conjunction with Pt auxiliary electrode and Ag/AgCl (3 M KCl) reference electrode.

4.8. Time-resolved fluorescence spectroscopy.

A time-correlated single photon counting (TCSPC) board (SPC-150, Becker & Hickl, Berlin, Germany) was used to measure the time-resolved fluorescence decay with a time channel of 48.9 ps. A 405 nm picosecond pulsed diode laser (LDH-P-C-405, Picoquant, Berlin, Germany) was irradiated to each sample in 3:7 THF:buffer (10 mM HEPES, pH = 7.4) solution. The emission wavelength 550 ± 5 nm of each flavin was extracted by using a bandpass filter (FB55010, Thorlabs Inc., Newton, NJ, USA). The emission from probe molecules is negligible in this spectral region.

All tests with human samples were performed after Institutional Review Board (IRB) approval.

4.9. Flow cytometry.

50 μL of human blood samples, diagnosed as eosinophilia (30.0%), were anticoagulated with dipotassium ethylene diamine tetraacetate (K_2EDTA). And then red blood cells (RBCs) were lysed using lysing solution (Becton Dickinson, San Diego, USA). After washing with 2 mL total volume of saline, the sediment was suspended with three types of working solutions (5 μM of **1-Zn**, **2**, and diluent only). The blood samples mixed with working solutions were incubated for 20 minutes at RT, and diluted with 2 mL of saline. The prepared samples were read with flow cytometer (FACSCantoII. Becton Dickinson, San Jose, USA) with FACSDiva program. The eosinophils were gated using forward scatter (FSC) and side scatter (SSC) properties of the cells and mean fluorescence intensities (MFIs) were measured by gathering emissions of 564−606 nm with excitation at 488 nm.

4.10. Fluorescence microscopy.

The blood smears were prepared using the same blood specimen. All slides were air dried at room temperature, then fixed with 70% ethanol for 5 minutes and air dried. 100 μL of three working solutions (5 μM of **1-Zn**, **2**, and diluent only) were spread on the blood smears and covered with cover glasses and incubated for 20 minutes at RT. The images of blood cells were captured using fluorescence microscope (BX51, Olympus, Japan).

4.11. Cell lysate test.

The methods for preparation of eosinophil lysate are described in detail elsewhere.[21] Two types of peripheral blood samples (50 μL each) were anticoagulated using K_2EDTA. The RBCs were lysed using lysing solution (Becton Dickinson, San Diego, USA). After washing with 2 mL of saline, the sediment was suspended in Ripa buffer (0.6 mL, Sigma Aldrich). Following incubation in ice for 20 min, the eosinophil lysates were centrifuged at 13,000 rpm for 15 min. Resulting supernatants were collected and diluted with ethanol and buffer (×1 SSC, pH = 7.4) (42:98:60 supernatant:buffer:EtOH, v/v). The resulting solution was mixed with probes (**1-Zn** and **2**), and then fluorescence intensity changes were examined by multimode plate reader (Molecular Devices, SpectraMax M2e). Fluorescent emission was measured at 588 nm with excitation at 555 nm with cutoff at 570 nm after shaking for 3 h. Four sets of each normal (0.5, 0.8, 0.8, 0.9%) and eosinophilia (9.0, 9.0, 9.3, 9.3%) human blood samples were tested in triplicates and averaged. The background signals were subtracted from the obtained signals.

5. References and notes

(1) Ayer, D. E. *Trends Cell. Biol.* **1999**, *9*, 193-198.

(2) (a) Moonen, C. T. W.; Vervoort, J.; Müller, F. In *flavins and flavoproteins*; Robert C. Bray, P. C. E., Ed.; Walter de Gruyter & Co: Berlin, 1984, p 493-496; (b) Xu, D.; Kohli, R. M.; Massey, V. *Proc. Natl. Acad. Sci. USA* **1999**, *96*, 3556-3561; (c) Zhou, Z.; Swenson, R. P. *Biochemistry* **1995**, *34*, 3183-3192; (d) Zhou, Z.; Swenson, R. P. *Biochemistry* **1996**, *35*, 12443-12454; (e) Zhou, Z.; Swenson, R. P. *Biochemistry* **1996**, *35*, 15980-15988.

(3) (a) Poolman, B.; Spitzer, J. J.; Wood, J. M. *BBA-Biomembranes* **2004**, *1666*, 88-104; (b) Biemans-Oldehinkel, E.; Mahmood, N. A. B. N.; Poolman, B. *Proc. Natl. Acad. Sci. USA* **2006**, *103*, 10624-10629.

(4) de Silva, A. P.; Gunaratne, H. Q. N.; Habib-Jiwan, J.-L.; McCoy, C. P.; Rice, T. E.; Soumillion, J.-P. *Angew. Chem. Int. Ed.* **1995**, *34*, 1728-1731.

(5) Huxley, A. J. M.; Schroeder, M.; Nimal Gunaratne, H. Q.; de Silva, A. P. *Angew. Chem. Int. Ed.* **2014**, *53*, 3622-3625.

(6) (a) Breinlinger, E.; Niemz, A.; Rotello, V. M. *J. Am. Chem. Soc.* **1995**, *117*, 5379-5380; (b) Breinlinger, E. C.; Keenan, C. J.; Rotello, V. M. *J. Am. Chem. Soc.* **1998**, *120*, 8606-8609; (c) Breinlinger, E. C.; Rotello, V. M. *J. Am. Chem. Soc.* **1997**, *119*, 1165-1166.

(7) (a) Miller, E. W.; Lin, J. Y.; Frady, E. P.; Steinbach, P. A.; Kristan, W. B.; Tsien, R. Y. *Proc. Natl. Acad. Sci. USA* **2012**, *109*, 2114-2119; (b) Woodford, C. R.; Frady, E. P.; Smith, R. S.; Morey, B.; Canzi, G.; Palida, S. F.; Araneda, R. C.; Kristan, W. B.; Kubiak, C. P.; Miller, E. W.; Tsien, R. Y. *J. Am. Chem. Soc.* **2015**, *137*, 1817-1824.

(8) Oien, N. P.; Nguyen, L. T.; Jernigan, F. E.; Priestman, M. A.; Lawrence,

D. S. *Angew. Chem. Int. Ed.* **2014**, *53*, 3975-3978.

(9) (a) Maiti, S.; Pezzato, C.; Garcia Martin, S.; Prins, L. J. *J. Am. Chem. Soc.* **2014**, *136*, 11288-11291; (b) Maiti, S.; Prins, L. J. *Chem. Commun.* **2015**, *51*, 5714-5716.

(10) Chen, J.; Liao, D.; Wang, Y.; Zhou, H.; Li, W.; Yu, C. *Org. Lett.* **2013**, *15*, 2132-2135.

(11) Heikal, A. A. *Biomark. Med.* **2010**, *4*, 241−263.

(12) Mayeno, A. N.; Hamann, K. J.; Gleich, G. J. *J. Leukoc. Biol.* **1992**, *51*, 172-175.

(13) (a) Barile, M.; Giancaspero, T. A.; Brizio, C.; Panebianco, C.; Indiveri, C.; Galluccio, M.; Vergani, L.; Eberini, I.; Gianazza, E. *Curr. Pharm. Design* **2013**, *19*, 2649−2675; (b) McKinley, M. C.; McNulty, H.; McPartlin, J.; Strain, J. J.; Scott, J. M. *Eur. J. Clin. Nutr.* **2002**, *56*, 850−856; (c) Jusko, W. J.; Lewis, G. P. *Am. J. Clin. Nutr* **1972**, *25*, 265−268.

(14) (a) The quantum yield was determined using Rhodamine 6G (Φ_f = 0.94 in ethanol) as a standard; (b) Fischer, M.; Georges, J. *Chem. Phys. Lett.* **1996**, *260*, 115−118; (c) Lavis, L. D.; Raines, R. T. *ACS Chem. Biol.* **2008**, *3*, 142-155.

(15) (a) Meade, T. J.; Gray, H. B.; Winkler, J. R. *J. Am. Chem. Soc.* **1989**, *111*, 4353-4356; (b) Zhou, J. S.; Rodgers, M. A. J. *J. Am. Chem. Soc.* **1991**, *113*, 7728-7734.

(16) Rhee, H.-W.; Choi, H.-Y.; Han, K.; Hong, J.-I. *J. Am. Chem. Soc.* **2007**, *129*, 4524-4525.

(17) (a) Berezin, M. Y.; Achilefu, S. *Chem. Rev.* **2010**, *110*, 2641-2684; (b) Lakowicz, J. R. *Principles of Fluorescence Spectroscopy*; 3rd ed.; Springer: Baltimore, MD, 2006; Chapter 9.

(18) Fukuzumi, S.; Tanii, K.; Tanaka, T. *J. Chem. Soc., Chem. Commun.* **1989**,

816−818.

(19) We presume that Zn^{II}-decomplexation of **1-Zn$_{ox}$** may be caused by acidic eluent condition.

(20) Haynes, R. K.; Chan, W.-C.; Wong, H.-N.; Li, K.-Y.; Wu, W.-K.; Fan, K.-M.; Sung, H. H. Y.; Williams, I. D.; Prosperi, D.; Melato, S.; Coghi, P.; Monti, D. *ChemMedChem* **2010**, *5*, 1282-1299.

(21) Ackerman, S. J.; Loegering, D. A.; Venge, P.; Olsson, I.; Harley, J. B.; Fauci, A. S.; Gleich, G. J. *J. Immunol.* **1983**, *131*, 2977-2982.

PART II.

The Combination of Probe and Graphene Oxide for Electrostatics-Driven Sensing Platform for Pyrophosphate Recognition

Background

1. Introduction

Pyrophosphate (PPi) is a biologically meaningful target because PPi is released from many cellular metabolisms such as DNA and RNA polymerization,[1] synthesis of cyclic AMP,[2] and the attachment of a given amino acid to a particular tRNA in gene expression,[3] catalyzed by DNA and RNA polymerase, adenylate cyclase, and aminoacyl-tRNA synthetase, respectively (Figure 1). These enzymatic activities are closely linked to the etiology of specific diseases.[4] Additionally, intracellular PPi levels have been considered as an important indicator in diagnostics.[5] Therefore, the development of a selective and sensitive detection method for PPi has been the main focus across diverse fields including bio-medicinal chemistry and diagnostics. While there are many traditional methods,[6] fluorescent chemosensors have received considerable

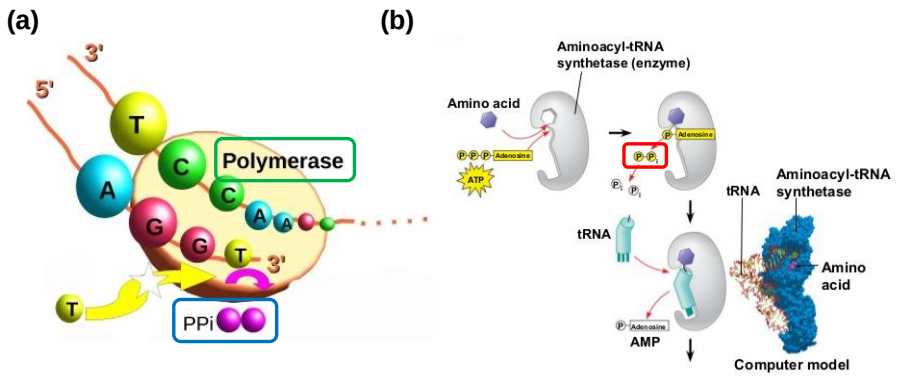

Figure 1. The depicted polymerase chain reaction (a) and the attachment of a given amino acid to a particular tRNA (b) (adopted from Friedberg, I. *et al.*, doi: 10.1371/journal.pcbi.1000667. and http://www.slideshare.net/veneethmathew/17-lecture-translation), respectively.

attention owing to their versatile and sensitive features such as their simple and rapid manner, suitability for high-throughput screening, and most importantly, usefulness for cellular imaging.[7] In particular, fluorescent probes in conjunction with Zn^{2+}–coordinated dipicolylamine (bisZnDPA) ligand have revealed high affinity toward phosphate derivatives owing to the strong coordination of Zn^{2+}–phosphate. Especially, pre-organized phenoxo-bridged binuclear bisZnDPA units have derived selective recognition for PPi over other phosphate derivatives.[8] However, almost bisZnDPA based fluorescent probes suffer from the deficient selectivity for PPi in the excess amount of other phosphate derivatives such as nucleoside triphosphates (nucleotides, NTPs), as is required for bio-analytical assays in which a small amount of PPi is released from a large amount of NTPs. Therefore, the highly sensitive and selective PPi probe is prerequisite for the application to real-time monitoring of the enzymatic reactions.

The integration of functionalized nanomaterial and technology with biology and chemistry is a current trend for developing new analytical tools.[9] For decades, carbon materials have garnered tremendous interest in various research fields such as nano-electronics, sensors, capacitors, and composite reinforcement, owing to their exceptional optoelectronic and physical properties such as transparency, supreme mechanical strength, good thermal conductivity, and high charge mobility.[10] In particular, graphene oxide (GO), chemically exfoliated from oxidized graphite, offers a new class of solution-dispersible polyaromatic platform for biosensor and drug delivery systems because GO has versatile features such as water solubility, amphiphilicity, surface functionalizability, and fluorescence quenching ability.[11] These fascinating characteristics of GO are mainly derived from its unique chemical

structures, which are composed of aromatic domains and oxygen containing hydrophilic functional groups that are negatively charged in physiological condition. Therefore, GO can undergo a complex interplay of π-π stacking/hydrophobic and electrostatic interaction with aromatic species, such as a nucleobase of NTPs and an aromatic side chain of amino acids,[12] and positively charged species[13] that provide GO-molecular probe hybridized nanocomposites.

Varieties of fluorescent dye labeled single-stranded DNA (ssDNA) and peptides have been successfully developed for the detection of DNA,[14] proteins,[15] small molecules,[16] and metal ions.[17] In these sensing concepts, high fluorescence quenching efficiency of GO as well as differentiated binding forces between GO and probes, upon before and after the target binding, are employed to achieve simple and sensitive detection. The best-known strategy is the structural change of ssDNA upon binding of complementary target ssDNA where the binding forces between GO and ssDNA are much stronger than that between GO and double-stranded DNA (dsDNA). While the exposed nucleobases in ssDNA adsorb strongly with the GO surface, nucleobases in dsDNA are effectively hidden in helical structure, which prevents the direct interaction of nucleobases with a GO surface.[14] Therefore, when ssDNA probes, bound to the GO surface in fluorescence quenching, are hybridized with its complementary target ssDNA, the formed dsDNA is detached from GO in recovered fluorescence (Figure 2).

In addition, GO biosensing platforms have been applied to enzyme activity assay, which is associated with catalytic reactions of DNAs, such as protein kinase,[18] endonuclease/methyl transferase,[19] exonuclease,[20] and telomerase.[21] The target enzymes have been extended to several important proteases such as

trypsin,[22] thrombin,[23] and metalloproteinase-2.[24] In addition to applications as a sensing platform, GO sheet has been successfully utilized for gene[25] and drug delivery[26] into cells by complexation with corresponding molecules through electrostatic interaction and covalent conjugation. Furthermore, GO derivatives have been utilized for photothermal therapy, originated from thermal relaxation after their strong absorption of near-IR (NIR) irradiation, which is inducible for oxidative stress, mitochondrial depolarization, and caspase activation resulting in apoptotic and necrotic cell death.[27]

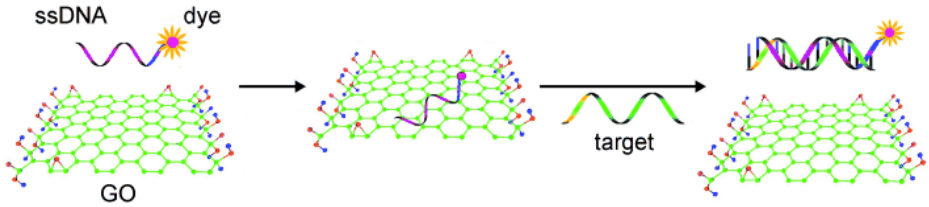

Figure 2. Schematic representation of GO based sensor for ssDNA detection. This figure is adapted from Yang, H.-H. *et al.*, *Angew. Chem. Int. Ed.* **2009**, *48*, 4785−4787.

GO is one of the most promising materials for biosensors and therapeutics. However, much work remains to be developed in reliable characterization methods that will aid in unambiguous structural identification as well as synthetic procedures that lead to relatively uniform products. Although several challenging issues remain, recent reports have shown that the convergence of GO and the traditional method could provide improved performances in recognizing various analytes, monitoring of enzyme activity, and delivering drugs. Sections 2 and 3 are a review of PPi chemosensors and recently developed GO-based sensing systems. It will be helpful for devising a new

prototype of PPi detection method in combination of GO-based nanotechnology and supramolecular chemistry.

2. Chemosensors for pyrophosphate

Selective recognition of PPi is a challenging task, requiring careful design of the sensing system. Generally, there are three different common approaches to PPi chemosensors, which adopt conventional hydrogen bonding interactions,[28] supramolecular complexation with Zn^{2+}-coordinated (bisZnDPA) ligand,[8,29] and displacement of metal-phosphate complex after the event.[30] Among them, the most popular approach is the bisZnDPA ligand-based strategy to achieve good sensitivity and selectivity for PPi over other phosphate species. Sections 2.1 and 2.2 focus on a strategy based on bisZnDPA. Subsequently, a new prototype of PPi detection method in use of conjugated polymers,[31] nanoparticles,[32] and quantum dots,[33] as alternative approaches for the small molecular probes is described.

2.1. BisZnDPA ligand-based chemosensors

In 2003[34] and 2004,[8] the Hong group demonstrated for the first time the phenoxo-bridged bisZnDPA ligand (**1**) as a good receptor for the selective and sensitive recognition of PPi over other anions. The X-ray crystal structure showed that four oxygen anions of PPi bind to the Zn^{2+} core of bisZnDPA bridging the two Zn^{2+} sites, thus forming two hexacoordination of Zn^{2+} ion. The signal change of probes was attributed to a weakening of the bond between phenolate oxygen and Zn^{2+} upon binding PPi, resulting in an increase of internal charge transfer (ICT) from the phenolate oxygen to fluorophore to turn on fluorescence (Figure 3a).

In 2007, the Hong group examined the synergistic effect of metal coordination and hydrogen bonding to improve the binding affinity and selectivity toward PPi.[35] Four amides introduced to bisZnDPA (**2**) improved binding affinity to PPi via additional binding force of the hydrogen bond (Figure 3b). This approach clearly shows that careful modification of bisZnDPA certainly has the potential to improve sensing performances.

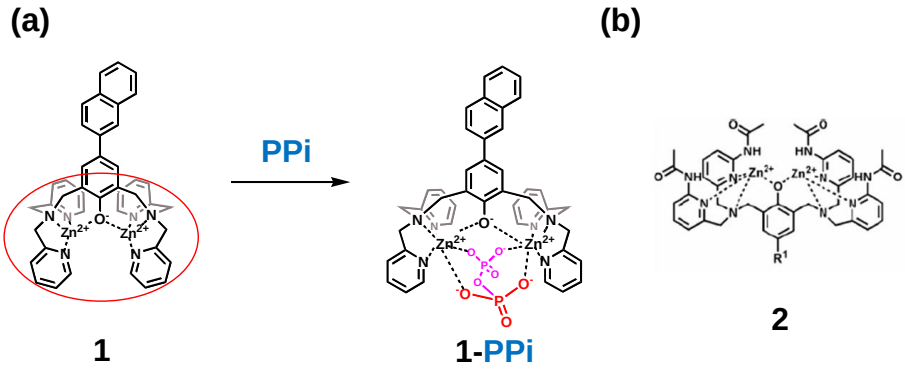

Figure 3. (a) Binding mode of **1** and PPi. Red circle indicates bisZnDPA. (b) Introduction of amides to improve binding affinity to PPi.

In 2011, the Pang group reported an excited state intramolecular proton transfer (ESIPT) based fluorescent probe for PPi.[29a] The 2-hydroxyl group of probe **3** can bind to a nearby Zn^{2+} site, resulting in blocked ESIPT. Upon PPi addition, the Zn^{2+} site moves away from the 2-hydroxyl group to tightly bind PPi forming the binuclear ZnDPA ligand structure, which leaves a free hydroxyl group for ESIPT. Therefore, probe **3** undergoes a large bathochromic shift (98 nm) as a result of the keto emission arising from ESIPT (Figure 4). Probe **3** was also capable of detecting PPi that was released from dNTPs in a PCR experiment.

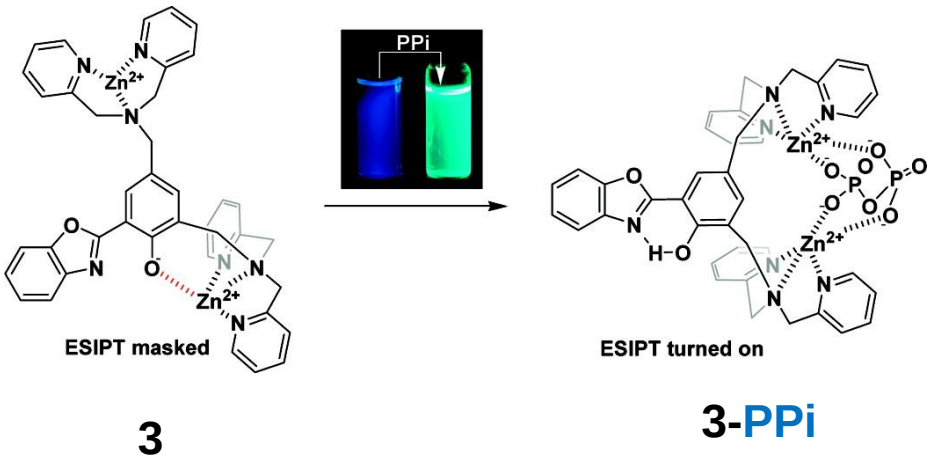

Figure 4. Proposed ESIPT Turn on Mechanism. This figure is adapted from Pang, Y. *et al.*, *Org. Lett.* **2011**, *13*, 1362−1365.

In 2011, the Hong group reported an ensemble system composed of probe **1** and boronic acid derivative (**4**) as a fluorescence displacement assay for the selective and differential sensing of PPi and NTPs.[29c] The addition of PPi to the ensemble system (**1**-**4**) induced a remarkable fluorescence enhancement, as a result of the formation of the **1**-PPi complex with concomitant displacement of **4**. In contrast, addition of ATP, GTP, CTP and UTP to the ensemble induced almost complete fluorescence quenching. This different fluorescence response with NTPs was attributed to the formation of ternary complexes (**1**-NTP-**4**) where bisZnDPA of **1** coordinated the triphosphate of the NTPs and the boronic acid moiety of **4** reacted with the OH groups of the sugar to form the corresponding boronate (Figure 5). However, these experiments require a high pH condition (10.5) in respect to the reactivity of boronic acid and sugar.

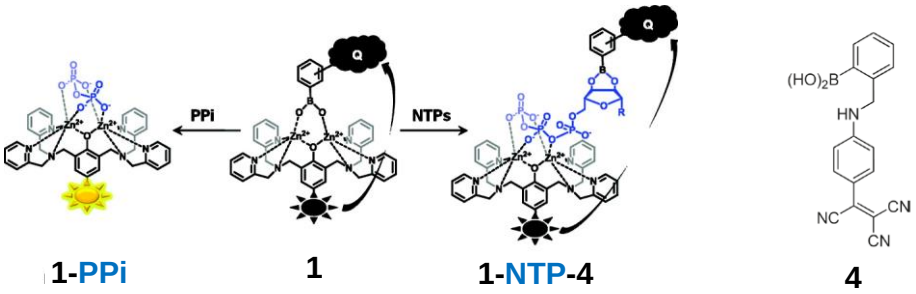

Figure 5. Design concept for discrimination between PPi and NTPs. Possible structures formed as a result of binding between probe **1** and PPi (left) and between probe **1**, quencher **4**, and NTPs (right). This figure is adapted from Hong, J.-I. *et al., J. Org. Chem.* **2011**, *76*, 417−423.

2.2. Recent approach for PPi detection in combination of nanotechnology

In 2010, the Schanze group reported the cationic polymer, poly(phenylene-ethynylene) bearing polyamine side chains (polymer **5**), which is prepared for a PPi sensing system performed at pH 6.5.[31] Upon the addition of PPi, polymer **5** displayed a decrease in the absorption band at 400 nm with the appearance of a new band at 430 nm, concurrently with the event in quenching of the original emission (433–455 nm) while a new emission band appeared at 550 nm. The red shifts in absorption as well as the blue to green emission change were attributed to the ability of PPi to crosslink the polymer chains, thus inducing polymer aggregation (Figure 6). However, Pi and other anions are unable to induce interpolymer interactions, while ADP and ATP show some interference.

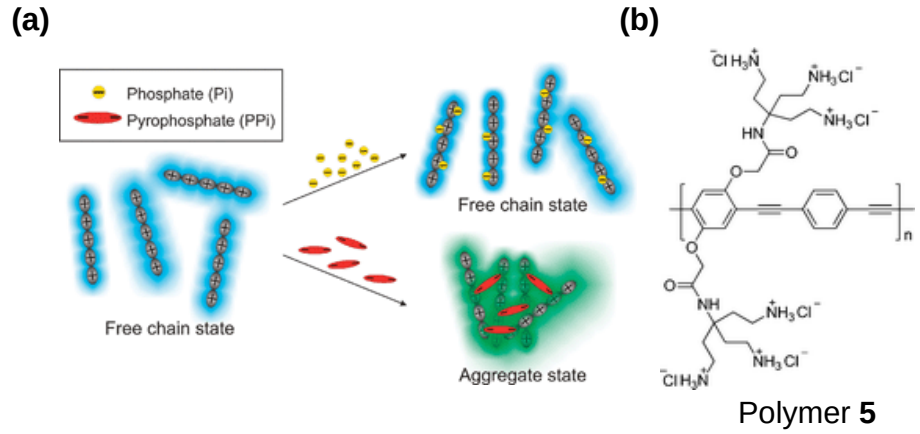

Figure 6. (a) Schematic illustration of PPi-induced polymer aggregation. (b) Cationic poly(phenylene-ethynylene) with branched polyamine side groups (polymer **5**). This figure is adapted from Schanze, K. S. *et al.*, *Chem. Commun.* **2010**, *46*, 6075−6077.

In 2011, the Ahn group reported a microarray-chip system based on polydiacetylenes (PDAs) liposomes that allow use of fluorescence turn-on signaling for phosphate-containing molecules (Figure 7).[29b] The prepared PDA liposomes showed selective colorimetric changes from blue to purple only for Pi and PPi in solution state. In a microarray-chip based assay, the enhancement of red fluorescence was detected only for PPi addition, while addition of Pi did not result in any change. ATP and AMP in the solution study, showed blue to purple color changes, which caused precipitation. The enhanced selectivity for the chip array over the solution state was attributed to the increased rigidity of the binding sites, where two Zn^{2+} sites can provide a better binding site for PPi than Pi.

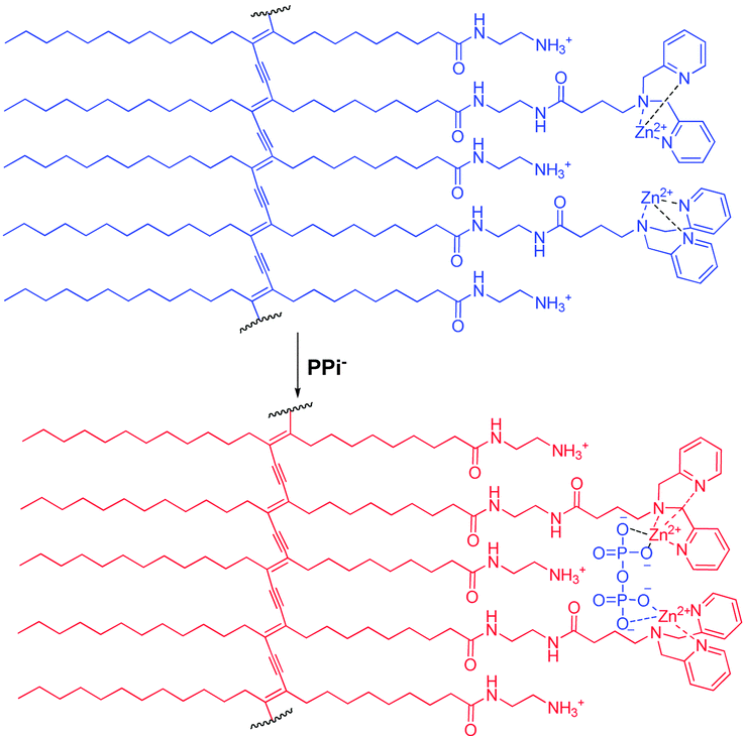

Figure 7. Proposed mechanism for the PPi induced colorimetric change of ZnDPA PDAs. This figure is adapted from Ahn, K. H. *et al.*, *Chem. – Asian J.* **2011**, *6*, 122−127.

In 2013, the Han group developed a competitive assay system consisting of 11-mercaptoundecylphosphoric acid functionalized gold nanoparticles (Phos-AuNPs) as a reporter unit and ZnDPA as a receptor unit for the selective recognition of PPi.[32] Upon the addition of ZnDPA, the Phos-AuNPs are converted to nano-aggregates as a result of ZnDPA interbinding to the phosphate groups, resulting in a visible color change from red to blue. The addition of PPi to an aqueous solution of the nano-ensemble returned the color back to red, which means that the nano-ensemble was re-dispersed into the Phos-AuNPs and ZnDPA-PPi complex (Figure 8).

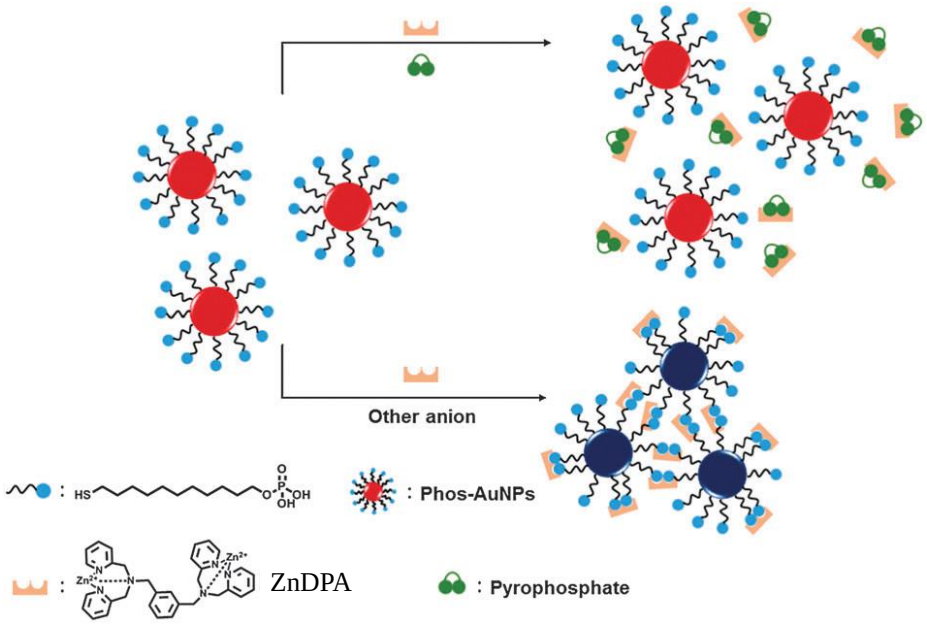

Figure 8. Schematic representation of the colorimetric probe for PPi using a competition assay. This figure is adapted from Han, M. S. *et al.*, *Chem. Commun.* **2013**, *49*, 152−154.

3. GO-based sensing systems

GO is a promising nanomaterial for use in biosensors because of its unique ability of remarkable water-solubility and biocompatibility as well as its super fluorescence quenching property. The convergence of graphene with biomolecules or small molecular probes possesses great potential for developing novel biosensors with improved performance. Sections 3.1 and 3.2 describe selected examples for examining a GO-based sensing strategy.

3.1. π-π stacking/hydrophobic interaction-driven GO-probe sensing platform

In 2011, the Li group described a simple but effective strategy for investigating T4 polynucleotide kinase (PNK) activity, coupled in λ exonuclease (λ exo) cleavage reaction as well as the FRET between dye-labeled DNA and GO.[18] Hybridized dsDNA-FAM was phosphorylated by PNK and then immediately cleaved by λ exo to generate ssDNA-FAM, resulting in its fluorescence quenching by the addition of GO. While λ exo exhibits a slow cleavage rate to dsDNA with an intact 5′-hydroxyl end in absence of PNK, dsDNA-FAM shows its original fluorescence emission because of the adsorption of dsDNA onto GO as weak and unstable in comparison with ssDNA. The sensitive detection of

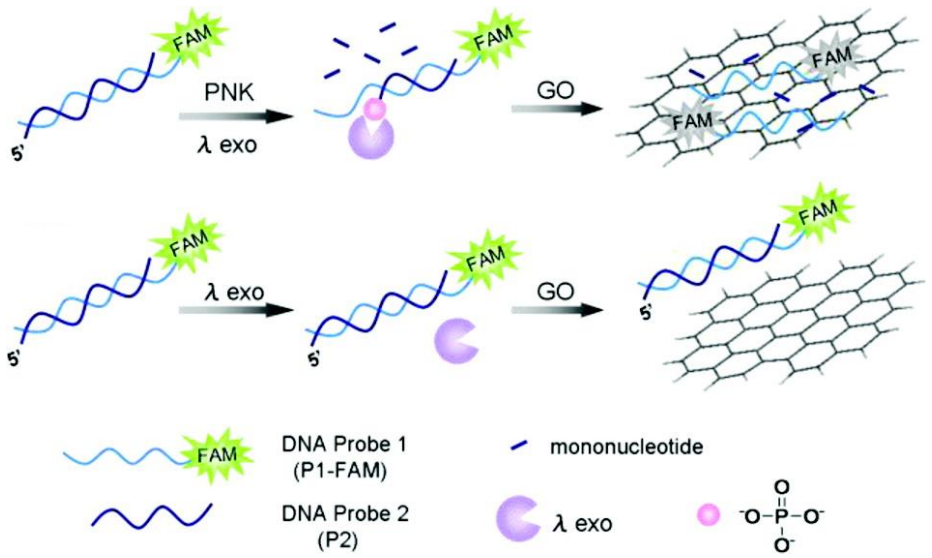

Figure 9. Schematic representation of GO based platform for PNK Activity and inhibition analysis. This figure is adapted from Yang, H.-H. *et al.*, *Anal. Chem.* **2011**, *83*, 8396−8402.

PNK activity was achieved due to the extraordinary fluorescence quenching ability of GO (Figure 9).

In 2011, the Min group reported a new method of endonuclease/methyltransferase activity assay based on the preferential binding of ssDNA over dsDNA to GO.[19] Substrate DNA is designed to possess a double-stranded part in conjunction with fluorophore as a signal unit concomitantly with a nuclease substrate and a single-stranded part for anchoring the DNA to the GO surface via strong noncovalent binding. Endonuclease-mediated DNA hydrolysis induced the release of the dsDNA part from GO, recovering the fluorescence of the labeled dye. Furthermore, the strategy was employed in a DNA methyltransferase activity assay in which the DNA strands methylated by methyltransferase cannot be hydrolyzed by endonuclease (Figure 10).

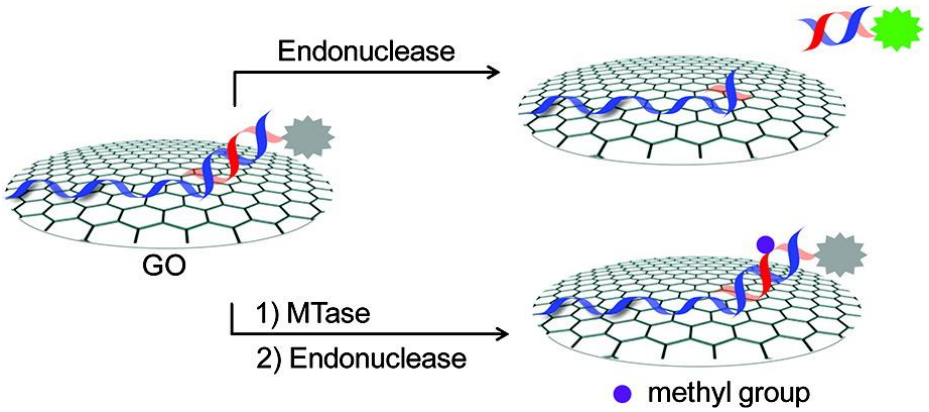

Figure 10. Strategy for endonuclease/methyltransferase activity assays based on fluorescence quenching by GO. This figure is adapted from Min, D.-H. *et al., Anal. Chem.* **2011**, *83*, 8906−8912.

In 2011, the Ye group designed a novel GO-based biosensing platform using a fluorophore-labeled peptide as a probe to demonstrate its utility for thrombin assay, where the fluorophore-labeled peptide has the thrombin sensitive core domain (dPhe-Pro-Arg-Gly).[23] When the fluorophore-labeled peptide is incubated with GO, it undergoes π-π stacking/hydrophobic interaction with the large hydrophobic basal plane of GO via aromatic and hydrophobic residues, and also forms an electrostatic function with ionizable edges via charged and polar residues (Lys and Arg) to form a strong energy- or charge-transfer complex. In the presence of thrombin, the core domain of peptide is specifically recognized and subsequently hydrolyzed, releasing a fluorophore-linked peptide segment from GO, thereby recovering fluorescence of the fluorophore. This in turn enables the real-time monitoring of thrombin activity (Figure 11).

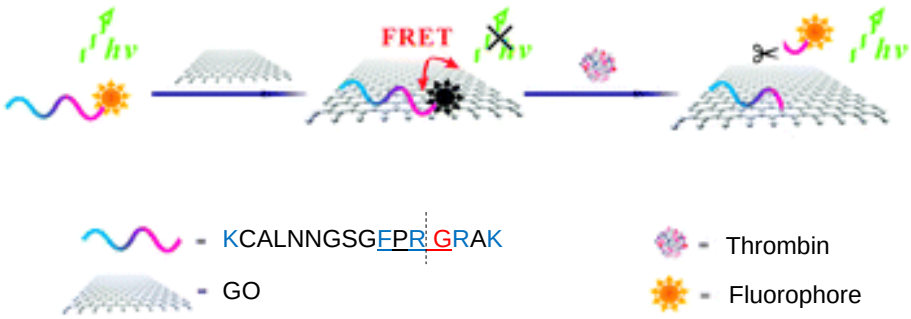

Figure 11. Schematic illustration of the peptide-GO bioconjugate as a sensing platform to monitor the proteolytic activity of thrombin. The peptide was labeled with fluorescein isothiocyanate. The cleavage point at Arg–Gly bonds is indicated by a dashed line. This figure is adapted from Ye, B.-C. *et al.*, *Chem. Commun.* **2011**, *47*, 2399−2401.

3.2. Electrostatics-driven GO-probe sensing platform

In 2010, the Loh group reported a simple ion-exchange strategy for DNA detection by using electrostatics-driven complex (PNP^+GO^-) in enhanced performances.[13a] The sensing principle is a thermodynamically favorable ion-complex formation of PNP^+DNA^- in comparison to the default state of PNP^+GO^-. In other words, DNA is a supercharged molecule, and therefore, PNP^+ has a greater ionic attraction for DNA than the weakly charged GO, and thus ion exchange can proceed. Additionally, PNP^+GO^- showed highly specific interactions with DNA in comparison to other biomolecules (RNA, proteins,

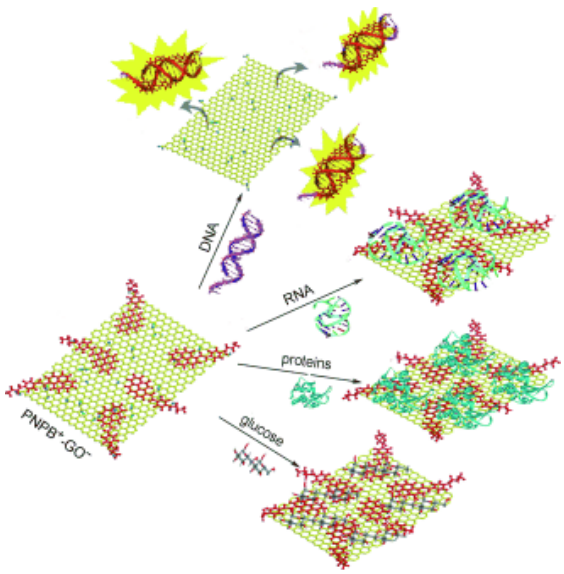

Figure 12. Sensing by PNP^+GO^-. DNA can complex efficiently with PNP^+ to form ionic complex PNP^+DNA^-, and thus switches on the fluorescence. Other biomolecules undergo π–π stacking on GO but do not remove PNP^+ from GO, and thus fluorescence remains quenched. This figure is adapted from Loh, K. P. *et al.*, *Angew. Chem. Int. Ed.* **2010**, *49*, 6549−6553.

carbohydrates), which allows selective and rapid detection of DNA in biological mixtures (Figure 12).

In 2011, the Zhang group described a new fluorescent method for trypsin activity assay.[22] The positively charged fluorescein-labeled peptide composed of six arginine residues (Arg_6-FAM) undergoes electrostatic interaction with GO composed of a negatively charged edge, thereby quenching in fluorescence. Upon the presence of trypsin, Arg_6-FAM can be hydrolyzed into small fragments, and accordingly, the fluorescein dye is dissociated from GO, gradually leading to fluorescence recovery (Figure 13).

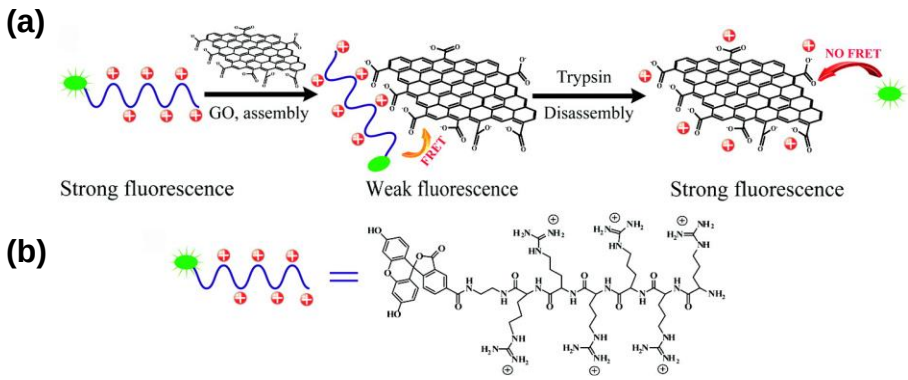

Figure 13. (a) Illustration of the design rationale for the fluorescence turn-on assay for trypsin with the ensemble of GO and Arg_6-FAM and (b) Chemical structure of Arg_6-FAM. This figure is adapted from Zhang, D. *et al., ACS Appl. Mater. Interfaces* **2011**, *3*, 1175−1179.

4. Concluding remarks

Although there are many reports for the PPi detection method, the selectivity for PPi over NTPs is still an elusive issue. Therefore, it is necessary to find alternative means of PPi detection, such as, the combination of the traditional

approaches with new technology using nanomaterials and nanotechnology. As mentioned above, GO undergoes complex interplay of π-π stacking/hydrophobic interaction with nucleobase of NTPs, which is never the case for PPi. This in turn could be causally linked to the differentiation of PPi and NTPs in respect to their binding affinity because PPi and NTPs are structurally similar, but with a small difference on the nucleoside (nucleobase and ribose). In other words, cooperation of the PPi selective probe and GO could be a promising method for discriminating PPi from NTPs; the fluorescent probe exhibits responses upon binding PPi or NTPs, while GO undergoes complex interplay with NTPs alone, which could interrupt NTPs' binding to the probe unit. In this regard, a positively charged bisZnDPA in conjunction with a fluorophore would be an ideal form for developing a GO-probe conjugate system in favor of the desired highly selective PPi detection.

5. References

(1) Ronaghi, M. *Genome Res.* **2001**, *11*, 3-11.

(2) G A Robinson; R W Butcher, a.; Sutherland, E. W. *Annu. Rev. Biochem.* **1968**, *37*, 149-174.

(3) Wang, L.; Schultz, P. G. *Angew. Chem. Int. Ed.* **2005**, *44*, 34-66.

(4) (a) Yao, P.; Fox, P. L. *EMBO Mol. Med.* **2013**, *5*, 332-343; (b) Trifunovic, A.; Wredenberg, A.; Falkenberg, M.; Spelbrink, J. N.; Rovio, A. T.; Bruder, C. E.; Bohlooly-Y, M.; Gidlof, S.; Oldfors, A.; Wibom, R.; Tornell, J.; Jacobs, H. T.; Larsson, N.-G. *Nature* **2004**, *429*, 417-423; (c) Park, S. G.; Schimmel, P.; Kim, S. *Proc. Natl. Acad. Sci. USA* **2008**, *105*, 11043-11049.

(5) (a) Doherty, M.; Belcher, C.; Regan, M.; Jones, A.; Ledingham, J. *Ann. Rheum. Dis.* **1996**, *55*, 432-436; (b) Timms, A. E.; Zhang, Y.; Russell, R. G. G.;

Brown, M. A. *Rheumatology* **2002**, *41*, 725-729.

(6) (a) Schimmel, P. R.; Söll, D. *Annu. Rev. Biochem.* **1979**, *48*, 601-648; (b) França, L. T. C.; Carrilho, E.; Kist, T. B. L. *Q. Rev. Biophys.* **2002**, *35*, 169-200.

(7) Sundberg, S. A. *Curr. Opin. Biotechnol.* **2000**, *11*, 47-53.

(8) Lee, D. H.; Kim, S. Y.; Hong, J.-I. *Angew. Chem. Int. Ed.* **2004**, *43*, 4777-4780.

(9) (a) Kong, J.; Franklin, N. R.; Zhou, C.; Chapline, M. G.; Peng, S.; Cho, K.; Dai, H. *Science* **2000**, *287*, 622-625; (b) Geim, A. K. *Science* **2009**, *324*, 1530-1534.

(10) (a) Liu, Y.; Dong, X.; Chen, P. *Chem. Soc. Rev.* **2012**, *41*, 2283-2307; (b) Shim, S. H.; Kim, K. T.; Lee, J. U.; Jo, W. H. *ACS Appl. Mater. Inter.* **2012**, *4*, 4184-4191; (c) Georgakilas, V.; Otyepka, M.; Bourlinos, A. B.; Chandra, V.; Kim, N.; Kemp, K. C.; Hobza, P.; Zboril, R.; Kim, K. S. *Chem. Rev.* **2012**, *112*, 6156-6214.

(11) Chung, C.; Kim, Y.-K.; Shin, D.; Ryoo, S.-R.; Hong, B. H.; Min, D.-H. *Acc. Chem. Res.* **2013**, *46*, 2211-2224.

(12) (a) Wang, F.; Liu, C.; Fan, Y.; Wang, Y.; Li, Z. *Chem. Commun.* **2014**, *50*, 8161-8163; (b) Wang, C.; Yu, P.; Guo, S.; Mao, L.; Liu, H.; Li, Y. *Chem. Commun.* **2016**, *52*, 5629-5632; (c) Zhang, H.; Jia, S.; Lv, M.; Shi, J.; Zuo, X.; Su, S.; Wang, L.; Huang, W.; Fan, C.; Huang, Q. *Anal. Chem.* **2014**, *86*, 4047-4051.

(13) (a) Balapanuru, J.; Yang, J.-X.; Xiao, S.; Bao, Q.; Jahan, M.; Polavarapu, L.; Wei, J.; Xu, Q.-H.; Loh, K. P. *Angew. Chem. Int. Ed.* **2010**, *49*, 6549-6553; (b) Xu, Y.; Malkovskiy, A.; Pang, Y. *Chem. Commun.* **2011**, *47*, 6662-6664; (c) Li, Y.; Duan, Y.; Zheng, J.; Li, J.; Zhao, W.; Yang, S.; Yang, R. *Anal. Chem.* **2013**, *85*, 11456-11463.

(14) Lu, C.-H.; Yang, H.-H.; Zhu, C.-L.; Chen, X.; Chen, G.-N. *Angew. Chem. Int. Ed.* **2009**, *48*, 4785-4787.

(15) Chang, H.; Tang, L.; Wang, Y.; Jiang, J.; Li, J. *Anal. Chem.* **2010**, *82*, 2341-2346.

(16) (a) Pu, Y.; Zhu, Z.; Han, D.; Liu, H.; Liu, J.; Liao, J.; Zhang, K.; Tan, W. *Analyst* **2011**, *136*, 4138-4140; (b) He, Y.; Wang, Z.-G.; Tang, H.-W.; Pang, D.-W. *Biosens. Bioelectron.* **2011**, *29*, 76-81.

(17) (a) Huang, W. T.; Shi, Y.; Xie, W. Y.; Luo, H. Q.; Li, N. B. *Chem. Commun.* **2011**, *47*, 7800-7802; (b) Wen, Y.; Xing, F.; He, S.; Song, S.; Wang, L.; Long, Y.; Li, D.; Fan, C. *Chem. Commun.* **2010**, *46*, 2596-2598; (c) Zhao, X.-H.; Kong, R.-M.; Zhang, X.-B.; Meng, H.-M.; Liu, W.-N.; Tan, W.; Shen, G.-L.; Yu, R.-Q. *Anal. Chem.* **2011**, *83*, 5062-5066.

(18) Lin, L.; Liu, Y.; Zhao, X.; Li, J. *Anal. Chem.* **2011**, *83*, 8396-8402.

(19) Lee, J.; Kim, Y.-K.; Min, D.-H. *Anal. Chem.* **2011**, *83*, 8906-8912.

(20) Lee, J.; Min, D.-H. *Analyst* **2012**, *137*, 2024-2026.

(21) Peng, L.; Zhu, Z.; Chen, Y.; Han, D.; Tan, W. *Biosens. Bioelectron.* **2012**, *35*, 475-478.

(22) Gu, X.; Yang, G.; Zhang, G.; Zhang, D.; Zhu, D. *ACS Appl. Mater. Inter.* **2011**, *3*, 1175-1179.

(23) Zhang, M.; Yin, B.-C.; Wang, X.-F.; Ye, B.-C. *Chem. Commun.* **2011**, *47*, 2399-2401.

(24) Feng, D.; Zhang, Y.; Feng, T.; Shi, W.; Li, X.; Ma, H. *Chem. Commun.* **2011**, *47*, 10680-10682.

(25) (a) Feng, L.; Zhang, S.; Liu, Z. *Nanoscale* **2011**, *3*, 1252-1257; (b) Bao, H.; Pan, Y.; Ping, Y.; Sahoo, N. G.; Wu, T.; Li, L.; Li, J.; Gan, L. H. *Small* **2011**, *7*, 1569-1578.

(26) Yang, X.; Zhang, X.; Liu, Z.; Ma, Y.; Huang, Y.; Chen, Y. *J. Phys. Chem. C* **2008**, *112*, 17554-17558.

(27) Markovic, Z. M.; Harhaji-Trajkovic, L. M.; Todorovic-Markovic, B. M.; Kepić, D. P.; Arsikin, K. M.; Jovanović, S. P.; Pantovic, A. C.; Dramićanin, M. D.; Trajkovic, V. S. *Biomaterials* **2011**, *32*, 1121-1129.

(28) (a) Sokkalingam, P.; Kim, D. S.; Hwang, H.; Sessler, J. L.; Lee, C.-H. *Chem. Sci.* **2012**, *3*, 1819-1824; (b) Caltagirone, C.; Bazzicalupi, C.; Isaia, F.; Light, M. E.; Lippolis, V.; Montis, R.; Murgia, S.; Olivari, M.; Picci, G. *Org. Biomol. Chem.* **2013**, *11*, 2445-2451.

(29) (a) Chen, W.-H.; Xing, Y.; Pang, Y. *Org. Lett.* **2011**, *13*, 1362-1365; (b) Kim, K. M.; Oh, D. J.; Ahn, K. H. *Chem.-Asian J.* **2011**, *6*, 122-127; (c) Lee, J. H.; Jeong, A. R.; Jung, J.-H.; Park, C.-M.; Hong, J.-I. *J. Org. Chem.* **2011**, *76*, 417-423.

(30) (a) Tsay, O. G.; Manjare, S. T.; Kim, H.; Lee, K. M.; Lee, Y. S.; Churchill, D. G. *Inorg. Chem.* **2013**, *52*, 10052-10061; (b) Lohani, C. R.; Kim, J.-M.; Chung, S.-Y.; Yoon, J.; Lee, K.-H. *Analyst* **2010**, *135*, 2079-2084; (c) Zhu, W.; Huang, X.; Guo, Z.; Wu, X.; Yu, H.; Tian, H. *Chem. Commun.* **2012**, *48*, 1784-1786; (d) Li, Y.; Dong, X.; Zhong, C.; Liu, Z.; Qin, J. *Sens. Actuators B* **2013**, *183*, 124-128.

(31) Zhao, X.; Schanze, K. S. *Chem. Commun.* **2010**, *46*, 6075-6077.

(32) Kim, S.; Eom, M. S.; Kim, S. K.; Seo, S. H.; Han, M. S. *Chem. Commun.* **2013**, *49*, 152-154.

(33) Noipa, T.; Ngamdee, K.; Tuntulani, T.; Ngeontae, W. *Spectrochim. Acta A* **2014**, *118*, 17-23.

(34) Lee, D. H.; Im, J. H.; Son, S. U.; Chung, Y. K.; Hong, J.-I. *J. Am. Chem. Soc.* **2003**, *125*, 7752-7753.

(35) Lee, J. H.; Park, J.; Lah, M. S.; Chin, J.; Hong, J.-I. *Org. Lett.* **2007**, *9*, 3729-3731.

Section 1.

Graphene oxide-probe conjugate system for the selective detection of pyrophosphate

Abstract

A highly selective detection of pyrophosphate (PPi) over nucleoside triphosphates (NTPs) has been accomplished by introduction of graphene oxide (GO) sheets to the molecular recognition system. This system was readily applied to real-time monitoring of DNA polymerase chain reaction (PCR) that requires the highly sensitive and selective manner for PPi detection.

1. Introduction

In challenges of the post-genome era, the development of the pyrophosphate (PPi) detection method with high selectivity and sensitivity has been a resurgent topic because PPi is a natural concomitant of DNA polymerase chain reaction (PCR) and gene expression catalyzed by DNA polymerases[1] and aminoacyl-tRNA synthetases,[2] respectively. These enzymatic activities are causally linked to the etiology of common genetic diseases, and therefore their monitoring is now an indispensable technique in therapeutic and diagnostic research.[3] While there are typical methods such as gel electrophoresis[4] and isotope labelling,[5] PPi monitoring in the fluorescent detection method is desired for the end-user laboratories owing to its simple and sensitive manner which is feasible for high throughput screening.[6] For decades, binuclear Zn^{2+}–coordinated dipicolylamine (bisZnDPA) ligand has been extensively utilized for PPi detection, owing to its high affinity toward phosphate derivatives. Especially,

the pre-organized phenoxo-bridged bisZnDPA unit has presented a notable selectivity toward PPi.[7] However, bisZnDPA-based probes upon presence of excess amount of phosphate derivatives such as nucleoside triphosphates (NTPs, nucleotides) suffer from low selectivity for PPi, as is required for real-time monitoring of the enzymatic reactions that involve NTPs, where a small amount of PPi is usually present in a large amount of NTPs. Herein, an advanced method is described for a highly selective PPi detection for which the functionalized nanomaterial and technology are combined with the supramolecular recognition chemistry.

Graphene oxide (GO) has elicited widespread attention as a fluorescent sensing platform because of its remarkable water-solubility, biocompatibility, and fluorescence quenching ability.[8] GO bears an aromatic domain and is negatively charged in a physiological condition. Therefore, GO undergoes a complex interplay of π-π stacking/hydrophobic interaction and electrostatic interaction both with aromatic species (a nucleobase of NTPs and an aromatic side chain of amino acids)[9] and positively charged molecules[10] to form an energy- or charge-transfer complex. Thus, a fluorophore (aromatic compound) in conjunction with a positively charged ligand would be feasible to create the GO-probe conjugate system. In addition, cooperation of the selective recognition ability of the bisZnDPA ligand and the versatile features of GO could be a promising method to exert a different effect on PPi and NTPs in respect to their binding affinity; the bisZnDPA based-probe exhibits fluorescence responses depending on the PPi (or NTPs) concentration, while GO undergoes complex interplay with NTPs,[9] which interrupts NTPs' binding to bisZnDPA. In this regard, new fluorescent probe **1** in which BisZnDPA is directly linked to coumarin fluorophore (6,8-bis(zinc^{2+}-dipicolylamine)-7-

hydroxy-3-*p*-tolyl-coumarin), is designed to present the GO-probe conjugate (GO-**1**) system for this work.

The sensing concept is guided by the modulation of electrostatic interaction between GO and probe **1** before and after PPi recognition. A fluorescence of **1** was markedly emerged when PPi was added to the electrostatically attractive patch (GO-**1**), which originates from a *charge inversion* in probe **1** upon binding PPi (**1**-PPi), concomitantly resulting in Columbic repulsion between GO and **1**-PPi (Scheme 1). Additionally, ionic strength modulation of a solution gives rise to subtle changes of sensitivity and increases the PPi selectivity over NTPs. Consequently, this concept was successfully applied to PCR monitoring, which requires a highly selective manner for PPi detection.

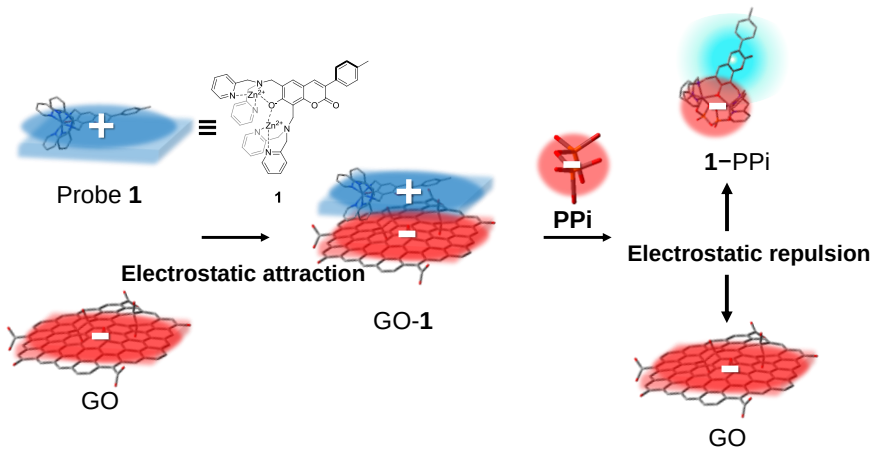

Scheme 1. Schematic representation of the proposed mechanism of PPi detection.

2. Data and results

The binuclear Zn^{2+} complex (bisZnDPA) of probe **1** was easily introduced by two simple steps: Mannich reaction of coumarin derivative (**3**) with dipicolylamine in the presence of formaldehyde to give **2**, which was then the Zn^{2+}-complexation of **2** by addition of an aqueous solution of $Zn(NO_3)_2$ (2

equiv.) for presenting probe **1** (Scheme 2).

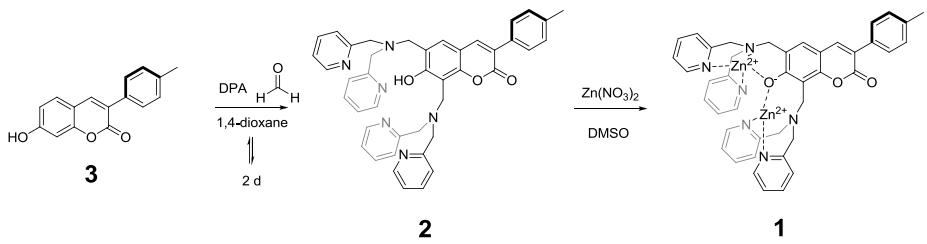

Scheme 2. Synthesis of probe **1**

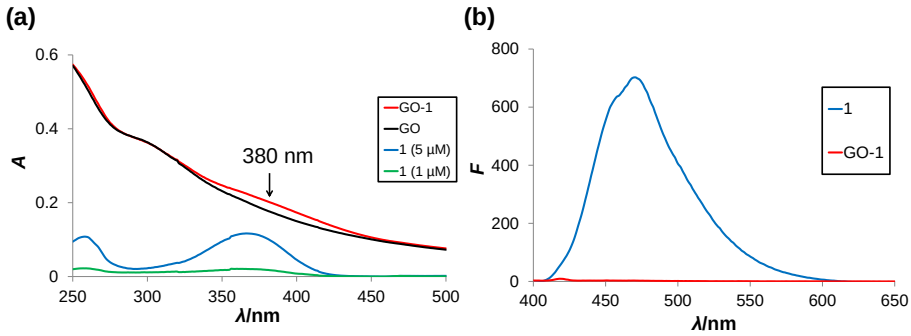

Figure 1. (a) UV−Vis. spectra of **1** (green line for 1 μM and blue line for 5 μM), GO (black line), and GO + probe **1** (red line) in 10 mM HEPES buffer (pH = 7.4). (b) Fluorescence spectra of **1** (1 μM) before (blue line) and after GO addition (0.001wt%, red line).

After the combination of GO and probe **1**, the strong interplay between GO and **1** (GO-**1**) was evidently monitored by spectroscopic changes of **1**. GO-**1** shows a slightly broadened and red shifted ($\Delta\lambda_{max}$ = 13 nm) absorption band compared to the coumarin's absorption (λ_{max} = 367 nm, probe **1**), due to the aromatic stacking of GO and **1**.[10a] The fluorescence of **1** was also completely quenched by adsorbed GO due to the strong photoinduced electron or energy transfer between **1** and GO (Figure 1).[9-10] X-ray photoelectron spectroscopy (XPS) was employed to give further evidence for a GO-probe **1** conjugate form.

The survey of GO-**1** exhibited two detectable peaks of Zn2p centred at 1020.6 and 1043.6 eV, served from probe **1**, while GO showed no detectable signal.[11] After treatment of PPi solution (10 μM), the corresponding peaks disappeared due to desorption of probe **1** from GO after PPi binding (**1**-PPi) (Figure 2). Ultraviolet photoelectron spectroscopy (UPS) showed a lower work function of GO-**1** (3.97 eV) than that of the intact GO (4.27 eV),[12] suggesting the π−π stacking between GO and probe **1** (Figure 3).[13] These photoelectron spectroscopic data confirm the formation of GO-probe **1** conjugate.

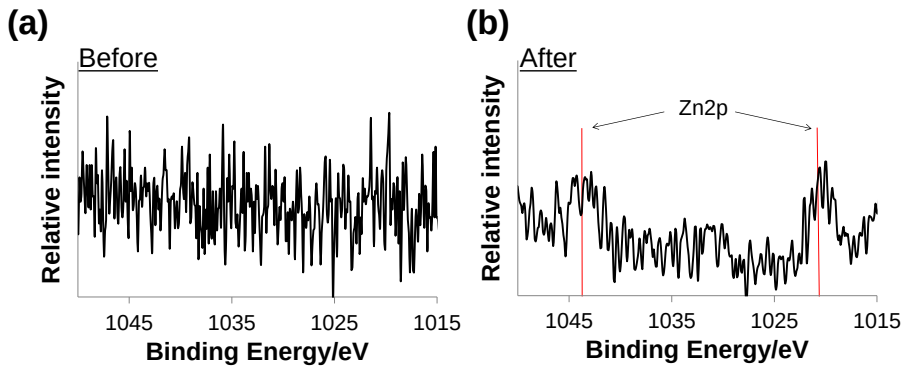

Figure 2. XPS spectra of the Zn2p region before and after probe **1** adsorption onto GO. The samples was carefully washed with deionized water for 3 times after the sample preparation by drop-casting method on silicon wafer.

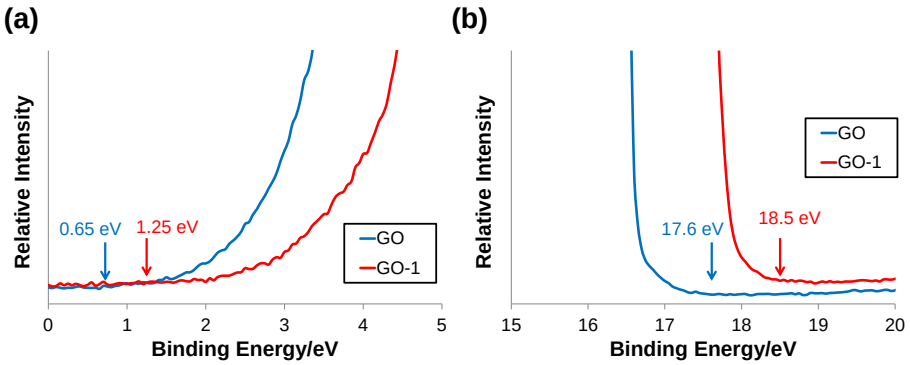

Figure 3. UPS spectra taken from GO and GO-**1** films.

The spectral behaviour of GO-**1** toward PPi was investigated in 10 mM HEPES buffer (pH = 7.4, HEPES = 2-[4-(2-hydroxy-ethyl)-1-piperazinyl]ethanesulfonic acid) by using fluorescence spectroscopy. Upon PPi titration, the fluorescence of probe **1** (1 μM) gradually increased at λ_{max} = 470 nm, which is attributed to the probe (**1**-PPi) desorption from GO as a result of the changed electrostatic forces (Figure 4a). An outstanding sensitivity as a detection limit of 9×10^{-8} M was assisted by the quenching effect of GO in favor of the large ON/OFF ratio (ΔF = 394.8) upon PPi recognition (8 equiv.) (Figures 4b and 5), which is approximately 263.2-fold larger than the value obtained from the probe only system (**1** only) (ΔF = 1.5, quenching process) (Figure 6). There was no significant change of fluorescence intensity of GO-**1** upon treatment with excess amount (30 equiv.) of other anions such as acetic acid (OAc^-), N_3^-, Cl^-, CO_3^{2-}, citrate, and more importantly inorganic phosphate (Pi) and NTPs (ATP, GTP, CTP, TTP, UTP) (Figure 4b). The competitive selectivity studies further demonstrate the highly selective response for PPi (Figure 7). Other GO-probe conjugates formed with the control probes, a mononuclear Zn^{2+} complex (GO-**4**), a non Zn^{2+}-coordinated compound (GO-**2**), and a coumarin molecule without BisZnDPA (GO-**3**), exhibited essentially no fluorescence response to the PPi addition (Figures 8 and 9, and Chart 1). These results demonstrate that the GO-probe conjugate system is preferable to the probe only system in respect to the sensitive response and the complementary binding of bisZnDPA, which is an integral part of the sensing mechanism for the selective detection of PPi.

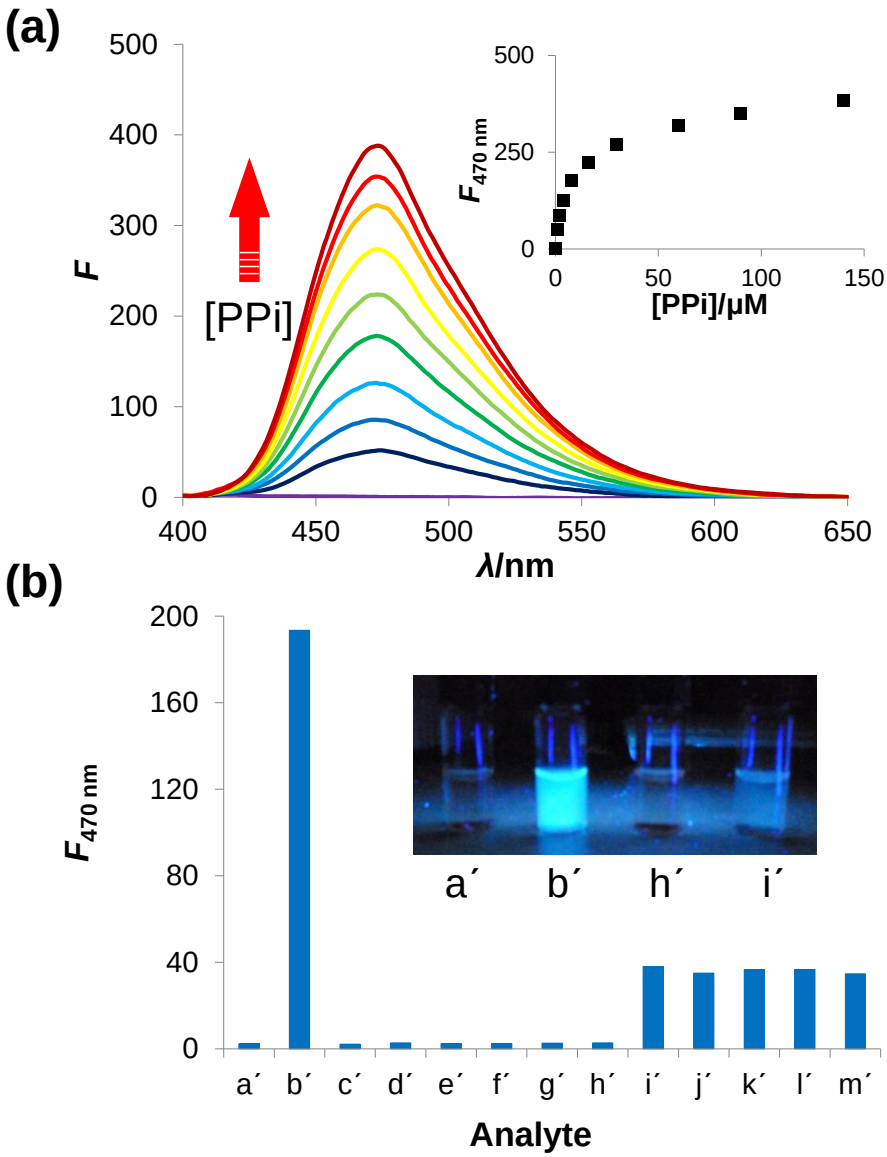

Figure 4. (a) Fluorescence spectra of GO-**1** (1 μM) against concentration of PPi in 10 mM HEPES buffer (pH = 7.4). The inset shows the fluorescence intensity at 470 nm upon the PPi titration. (b) The bar diagram shows changes in the fluorescence intensity of GO-**1** (1 μM) in the presence of various anions (30 equiv.) such as (a') control (GO-**1**), (b') PPi (8 equiv.), (c') OAc^-, (d') N_3^-, (e') Cl^-, (f') CO_3^{2-}, (g') citrate, (h') Pi, (i') ATP, (j') GTP, (k') CTP, (l') TTP, (m') UTP. The excitation wavelength was 367 nm. The inset is the photograph showing fluorescence in vials (a', b', h', and i') under UV hand lamp irradiation (λ_{ex} = 365 nm, 6 W).

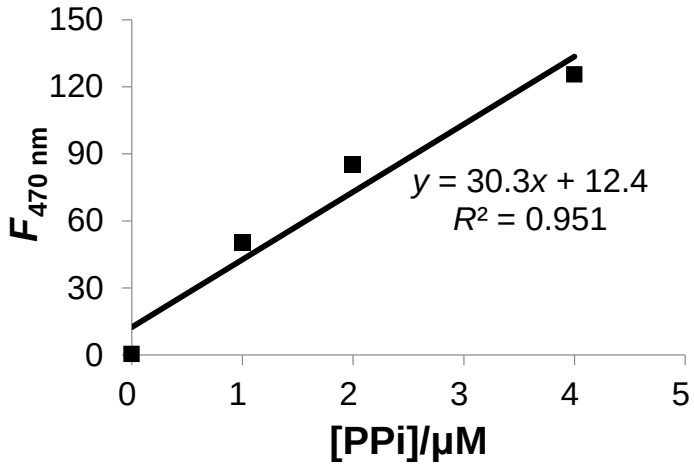

Figure 5. Fluorescence intensity of GO-**1** showing linear dependence at lower concentrations of PPi (1−5 μM) in 10 mM HEPES buffer (pH = 7.4). Detection limit was determined to be 9×10^{-8} M, which was obtained from $3\sigma/30.3\times10^{-6}$, where σ is the standard deviation of background signal (n = 3).

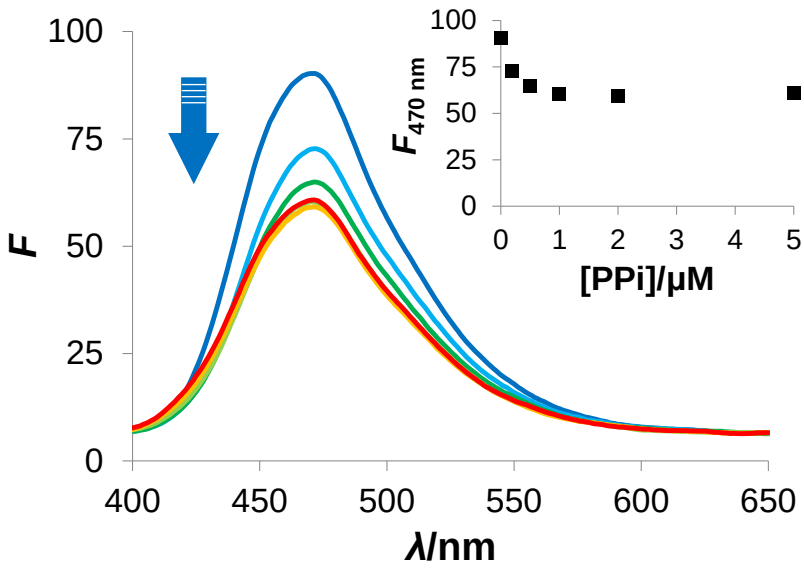

Figure 6. Fluorescence spectra of **1** (1 μM) against concentration of PPi (0.1−5.0 μM) in 10 mM HEPES buffer (pH = 7.4). The inset shows the fluorescence intensity at 470 nm upon the PPi titration. The excitation wavelength is 367 nm.

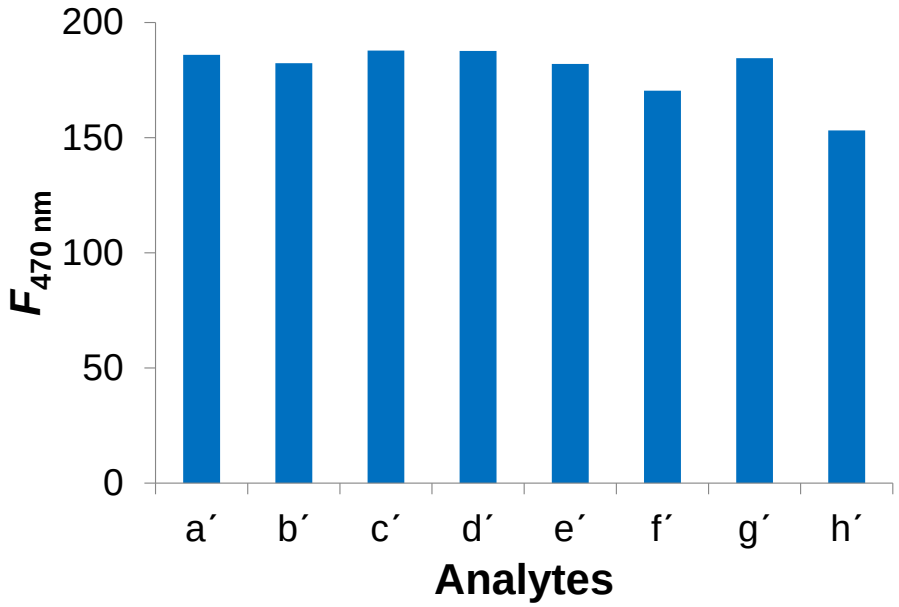

Figure 7. The bar diagram showing the fluorescence response of GO-**1** (1 μM) to PPi (8 equiv.) in the co-presence of other anions (30 equiv., sodium salt): (a') control (GO-**1**) (b') OAc^-, (c') N_3^-, (d') Cl^-, (e') CO_3^{2-}, (f') citrate, (g') Pi, (h') ATP. DATA were acquired in 10 mM HEPES (pH = 7.4). The excitation wavelength was 367 nm.

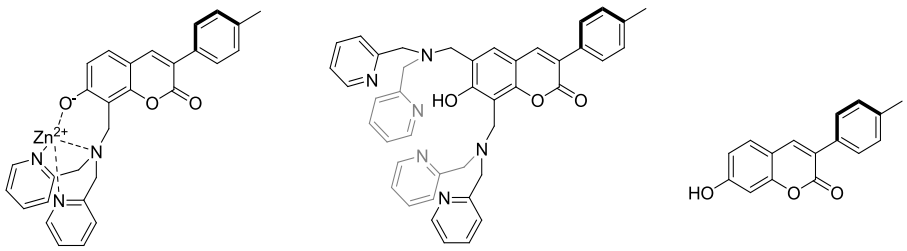

4 **2** **3**

Chart 1. Control probes, mononuclear Zn^{II} complex (**4**), non Zn^{II}-coordinated compound (**2**), and a coumarin molecule without bisZnDPA (**3**).

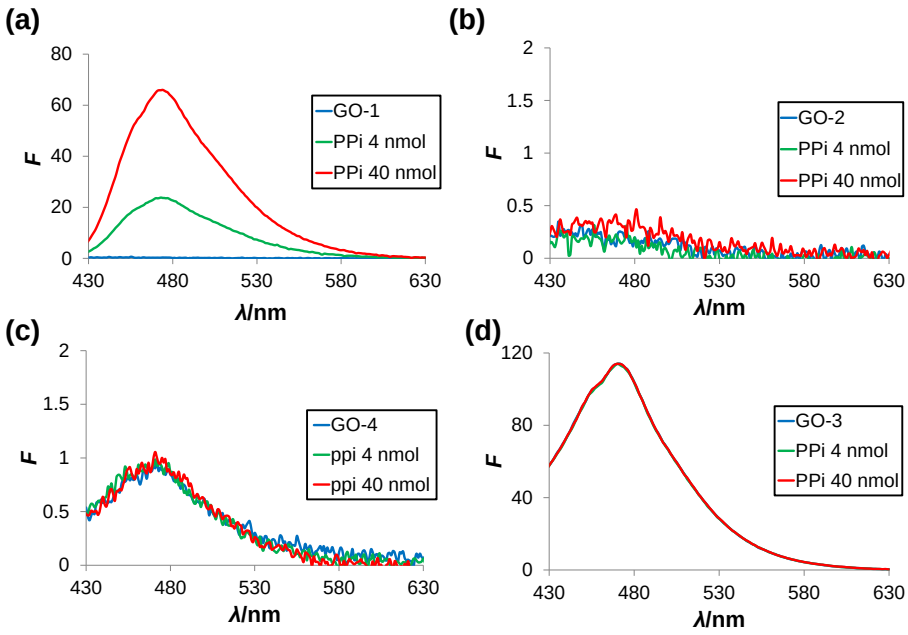

Figure 8. Fluorescence spectra of GO-probe conjugates (1 μM) upon PPi addition (2, 20 μM): GO-**1** (a), GO-**2** (b), GO-**4** (c), GO-**3** (d).

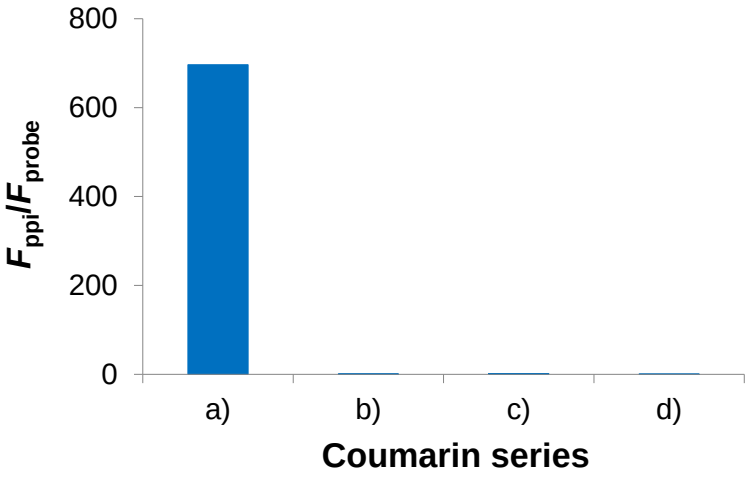

Figure 9. Fluorescence intensity ratio of GO-probe conjugates before (F_{probe}) and after the PPi addition (F_{PPi}, [PPi] = 20 μM): GO-**1** (a), GO-**2** (b), GO-**4** (c), GO-**3** (d). The fluorescence intensity (470 nm) was measured with excitation at 367 nm.

To understand the mechanism of selectivity for PPi over NTPs, a systematic study was performed to investigate the effect of ionic strength in tuning of the binding affinities of PPi and ATP (Table 1). The ionic strength influences the intermolecular interactions of GO and NTPs such as π-π stacking/hydrophobic and electrostatic interaction.[14] In other words, in higher ionic strength solution, the ions can effectively screen the negative charges of both GO and NTPs, thereby decreasing the electrostatic repulsion between the carboxylate of GO and triphosphate of NTPs, while increasing the π-π stacking/hydrophobic interaction between the aromatic region of GO and nucleobase of NTPs. That is, NTPs can be strongly stacked on GO in higher ionic strength. This in turn could trigger the selective response to PPi over NTPs because in this situation, the NTPs could not approach probe **1**. Or, if probe **1** has ever bound to NTP, the complex (**1**-NTP) could not depart from the GO sheet due to the interaction of the nucleobase and GO, whereby the fluorescence could not be recovered fully. However, Figure 10 shows that the gap of binding affinity of PPi and ATP

Table 1. Binding constants [a] of GO-**1** [b] for PPi and the gap of the fluorescence intensity upon the addition of PPi and ATP [c] in varied ionic strength conditions [d]

Ionic strength (I_{HEPES})	K_a	$\Delta F_{PPi/ATP}$
1 mM	$4.39 \pm 1.80 \times 10^4$	13.2-fold
10 mM	$8.60 \pm 4.80 \times 10^4$	5.66-fold
50 mM	$3.11 \pm 2.58 \times 10^5$	2.76-fold

[a] K_a/M^{-1}

[b] 1 μM in 10 mM HEPES buffer (pH = 7.4)

[c] The fluorescence intensity was measured upon the addition of 140 μM of PPi and ATP, respectively. (λ_{ex} = 367 nm, λ_{em} = 470 nm)

[d] The ionic strength was modulated by the concentration of HEPES.

decreases in higher ionic strength, but rather increase in lower ionic strength, which is opposite to our assumption. Thus, it appears that simply considering the π-π stacking/hydrophobic interaction of a nucleobase and GO is not sufficient to describe the mechanism of selectivity.

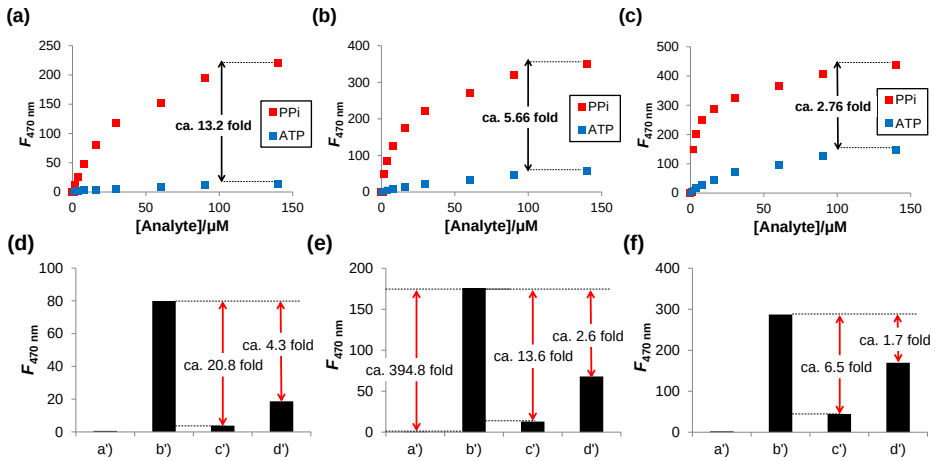

Figure 10. (a−c) PPi (red square) and ATP (blue square) titration curves of GO-**1** (1 μM) conducted in 1 mM (a), 10 mM (b), and 50 mM (c) HEPES buffer (pH = 7.4). (d−f) Fluorescence intensities (λ_{em} = 470 nm) of GO-**1** (1 μM) in 1 mM (d), 10 mM (e), and 50 mM (f) HEPES buffer (pH = 7.4) after the addition of PPi and ATP; GO-**1** (a'), GO-**1** + 8 μM of PPi (b'), GO-**1** + 8 μM of ATP (c'), GO-**1** + 140 μM of ATP (d').

Instead, the steric effect of the bulky side of NTPs (nucleobase and ribose) is considered. An increasing ionic strength (I_{NaCl} = 0−100 mM) can screen the charged sites of GO and **1**, leading to a decrease in their Coulombic attraction[15] and thereby gradually recovering the fluorescence of **1**, as depicted in Figure 11. Thus, higher ionic strength may render probe **1** to become less in contact with GO concomitantly allowing the BisZnDPA to be exposed toward solution

phase, like the membrane–cytosol interface where osmosensing takes place.[16] This orientation increases the binding affinity both of PPi and ATP toward probe **1** (Figure 10). Conversely, the adsorption of probe **1** onto GO becomes more compact in lower ionic strength, where BisZnDPA could be covered with charged functional groups on the GO sheet. Thus, the sterically hindered binding site may control the binding affinity of PPi and NTPs. In other words, the major reason for the selectivity is the steric effect in the bulky tail of NTPs. This prevents its approach into the crowded bisZnDPA, which is never the case for PPi. Therefore, as the ionic strength is decreased (*i.e.*, as bisZnDPA becomes more covered by functional groups on GO), PPi is effectively distinguished from NTPs.

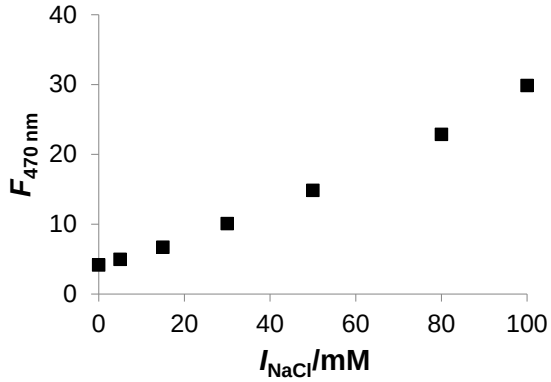

Figure 11. Fluorescence intensity (λ_{em} = 470 nm) change of GO-**1** (1 μM) upon the variation of NaCl ionic strength ([I_{NaCl}] = 0−100 mM) in 10 mM HEPES buffer (pH = 7.4) (in the absence of PPi).

Additionally, the PPi titration experiment was performed in the co-presence of an excess amount of ATP (140 equiv.). Upon the addition of ATP, the background signal of GO-**1** lightly increased. However, subsequent addition of PPi into the ATP solution led to a further increase in fluorescence with a

detection limit at micromolar concentrations (Figure 12). The best detection limit (LOD = 2×10^{-6} M) was obtained from lower ionic strength solution (1 mM HEPES buffer), owing to the weak background signal upon the excess amount of ATP and responsible for a large ON/OFF ratio upon the subsequent PPi addition (Figure 12).

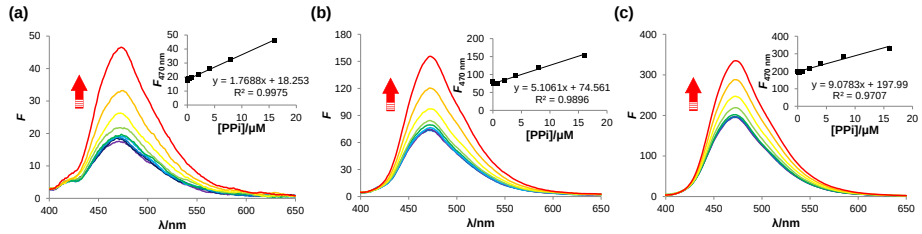

Figure 12. Fluorescence spectra of GO-**1** (1 μM) upon PPi titration (0.1 μM−16 μM) in excess amount of ATP (140 μM) in 1 mM (a), 10 mM (b), and 50 mM (c) HEPES buffer (pH = 7.4). Detection limit was determined to be 2.1 μM for (a), 3.5 μM for (b), and 4.7 μM for (c), which were obtained from 3σ/slope, where σ is the standard deviation (n = 3) of the fluorescence intensity upon the presence of ATP (140 μM).

Finally, GO-**1** was applied to fluorescence monitoring of PCR, which requires a highly sensitive and selective response for PPi over dNTPs. The band intensity on gel electrophoresis shows the degree of DNA extension, which is proportional to the concentration of PPi released from PCR.[4] Upon the addition of PCR product (2 μL of 10−15 cycles) into the GO-**1** solution, the fluorescence intensity (λ_{max} = 470 nm) increased in a linear fashion up to 2.9-fold relative to a negative control (PCR without DNA template), showing the same trend with the band intensity on gel electrophoresis (Figures 13 and 14). The result indicates that GO-**1** could be a new alternative for PCR monitoring in an easily

accessible manner.

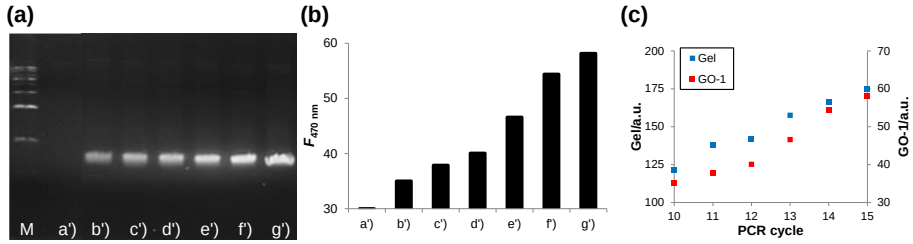

Figure 13. (a) Gel electrophoresis of finished PCR mixtures. M is the standard bp ladder. (b) Fluorescence intensity of GO-**1** at 470 nm upon the addition of finished PCR product (2 μL of 10−15 cycles) in 10 mM HEPES buffer (pH = 7.4): The enzymatic reaction was performed without template DNA for 15 cycles (a'), and with template DNA for 10 cycles (b'), 11 cycles (c'), 12 cycles (d'), 13 cycles (e'), 14 cycles (f'), 15 cycles (g'). (c) The fluorescence intensity of each DNA band from gel electrophoresis (blue square) was compared with that of GO-**1** upon the addition of the PCR mixture (red square). The mean fluorescence intensity of DNA band was determined by the Adobe Photoshop CS6 software.

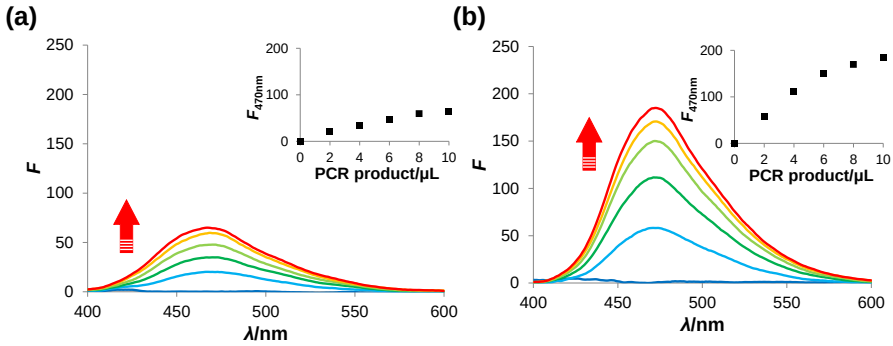

Figure 14. Fluorescence spectra of GO-**1** (1 μM) upon the addition of finished PCR product (2−10 μL) in 10 mM HEPES buffer (pH = 7.4). The enzymatic reaction was performed without (a) and with template DNA for 15 cycles (b). The inset shows the fluorescence intensity at 470 nm. The excitation wavelength is 367 nm. Panel (a) shows the slight increase in fluorescence of GO-**1** as a result of the probe's response to dNTPs in PCR mixture.

3. Conclusion

In conclusion, the rationally designed probe **1** readily allowed the complex interplay with GO, providing the ideal model for the electrostatics-driven PPi detection method. The combination of the probe and GO led to the excellent selectivity toward PPi, remarkably, even in an excess amount of ATP. Consequently, GO-**1** was successfully applied to PCR monitoring. This sensing platform not only has a potential use in other enzymatic assays that release PPi, but also can be readily applied to other anion detection in conjunction with corresponding ligand.

4. Experimental

4.1. General procedure

All fluorescence and UV−Vis absorption spectra were recorded with Jasco FP 6500 and Beckman coulter DU 800 spectrophotometers. All ^{1}H and ^{13}C NMR spectra were collected in $CDCl_3$ or DMSO-d_6 on a Bruker 300 MHz spectrometer. All chemical shifts are reported in ppm value using the peak of residual proton signals of TMS as an internal reference. HRMS, XPS, and UPS data received directly from The National Center for Inter-University Research Facilities (NCIRF), Research Institute of Advanced Materials, and Korea Basic Science Institute, respectively. In a UPS experiment, the energy of emitted electrons is given by $E_{kin,h\nu} = E(h\nu) - E_{bin}$, where $E_{kin,h\nu}$ is the kinetic energy of the emitted electron, $E(h\nu)$ is the photon energy (21.22 eV for the HeI line), and E_{bin} is the binding energy of the electron before excitation. All chemicals were purchased from Aldrich and TCI, and then used as received. All solvents were analytical reagents from Duksan Pure Chemical Co., Ltd. The DMSO for spectra detection was of HPLC reagent grade, without fluorescent impurity. De-ionized water (DI water) was used in all studies.

4.2. Synthesis of probes

Compound **3** was prepared by the literature method[17] and synthesis of **2** and **1** is described below.

Synthesis of 2. To a solution of 37% aqueous formaldehyde solution (2.53 mL, 30 mmol) in 1,4-dioxane (60 mL) was added 2,2'-dipicolylamine (5.4 mL, 30 mmol), and the reaction mixture was stirred for 5 h at 50°C. After then, 2.9 g of the compound **3** (11.5 mmol) was added to the reaction mixture. After stirring for 2 days at 110°C, the reaction mixture was cooled down to room temperature (RT), and the solvent was evaporated under reduced pressure. The crude product was purified by flash column chromatography using

MeOH:CH_2Cl_2 (from 0:100 to 3:100, gradient) as eluent to give the desired product (yellow crumbly solid) in 65% yield. ^{1}H NMR (DMSO-d_6, 300 MHz): δ 12.79 (br, 1H), 8.51 (d, 2H, *J* = 4.2 Hz), 8.48 (d, 2H, *J* = 4.5 Hz), 8.11 (s, 1H), 7.75−7.61 (m, 7H), 7.56−7.49 (m, 4H), 7.27−7.22 (m, 6H), 4.01 (s, 2H), 3.88 (s, 4H), 3.82 (s, 4H), 3.77 (s, 2H), 2.35 (s, 3H); ^{13}C NMR ($CDCl_3$, 75 MHz): δ 161.1, 160.4, 159.3, 158.7, 152.8, 148.9, 148.7, 140.4, 138.0, 136.8, 136.6, 132.5, 129.1, 128.4, 128.3, 123.3, 123.2, 123.2, 122.8, 122.1, 122.1, 111.7, 110.5, 59.9, 59.9, 53.5, 47.6, 21.3; HRMS (FAB$^+$, m-NBA) $[M+H]^+$ calculated for $C_{42}H_{39}N_6O_3$ 675.3078, observed 675.3070.

Synthesis of 1. To a solution of **2** in DMSO (10 mM, 0.5 mL) was added 0.5 mL of $Zn(NO_3)_2{\cdot}6H_2O$ stock solution in DMSO (20 mM). After aging for 30 min at RT, the resulting solution was used as a stock solution of **1** (5 mM) without further purification (Greenish solution, quantitative yield).[18] ^{1}H NMR (DMSO-d_6, 300 MHz): δ ; 8.54 (br, 4H), 7.98 (d, 4H, *J* = 6.6 Hz), 7.84 (s, 1H), 7.60−7.52 (m, 6H), 7.40 (br, 4H), 7.25 (d, 2H, *J* = 8.1 Hz), 7.19 (s, 1H), 4.39−4.09 (m, 8H), 3.84 (s, 2H), 3.72 (s, 2H), 2.33 (s, 3H); HRMS (FAB$^+$, m-NBA) $[M+2NO_3^-]^+$ calculated for $C_{42}H_{37}N_8O_9Zn_2$ 925.1266, observed 925.1264.

Synthesis of 5. Compound **5** was obtained from the same procedure of **2** with half equivalent of the reagents (15 mmol, each formaldehyde and 2,2'-dipicolylamine) in 75% yield (yellow crumbly solid). ^{1}H NMR ($CDCl_3$, 300 MHz): δ 8.61 (d, 2H, *J* = 4.5 Hz), 7.73 (s, 1H), 7.70 (td, 2H, *J* = 1.5 Hz, *J* = 7.5 Hz), 7.62 (d, 2H, *J* = 8.1 Hz), 7.41 (d, 2H, *J* = 7.8 Hz), 7.36 (d, 2H, *J* = 8.4 Hz), 7.28−7.24 (m, 2H), 7.22 (t, 2H, *J* = 6.9 Hz), 6.92 (d, 2H, *J* = 8.7 Hz), 4.18 (s, 2H), 3.97 (s, 4H), 2.41 (s, 3H); ^{13}C NMR ($CDCl_3$, 75 MHz): δ 161.9, 160.4, 157.9, 153.3, 148.8, 140.4, 138.2, 137.0, 132.4, 129.1, 128.3, 128.2, 123.3,

123.3, 122.4, 114.5, 112.1, 110.0, 59.9, 47.8, 21.3; HRMS (FAB$^+$, m-NBA) $[M+H]^+$ calculated for $C_{29}H_{26}N_3O_3$ 464.1974, observed 464.1972.

Synthesis of 4. To a solution of **5** in DMSO (10 mM, 0.5 mL) was added 0.5 mL of $Zn(NO_3)_2 \cdot 6H_2O$ stock solution in DMSO (10 mM). After aging for 30 min at RT, the resulting solution was used as a stock solution of 4 (5 mM) without further purification (Greenish solution, quantitative yield). ^{1}H NMR (DMSO-d_6, 300 MHz): 8.72 (d, 2H, J = 5.1 Hz), 8.19 (s, 1H), 8.13 (t, 2H, J = 7.5 Hz), 7.67−7.59 (m, 7H), 7.28 (d, 2H, J = 8.1 Hz), 6.96 (br, 1H), 4.43 (d, 2H, J = 16.2 Hz), 4.02 (s, 2H), 3.87 (d, 2H, J = 15.9 Hz), 2.35 (s, 3H); HRMS (FAB$^+$, m-NBA) $[M]^+$ calculated for $C_{29}H_{24}N_3O_3Zn$ 526.1109, observed 526.1111.

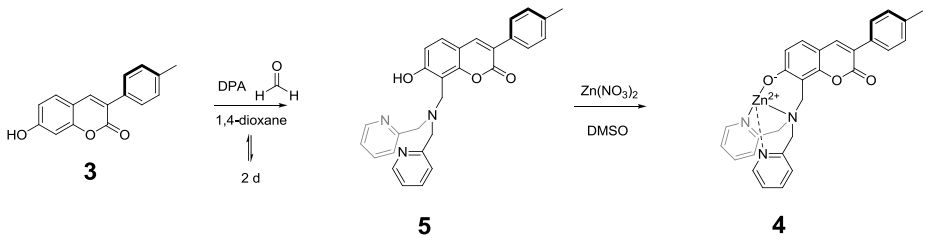

Scheme 3. Synthesis of probe **4**

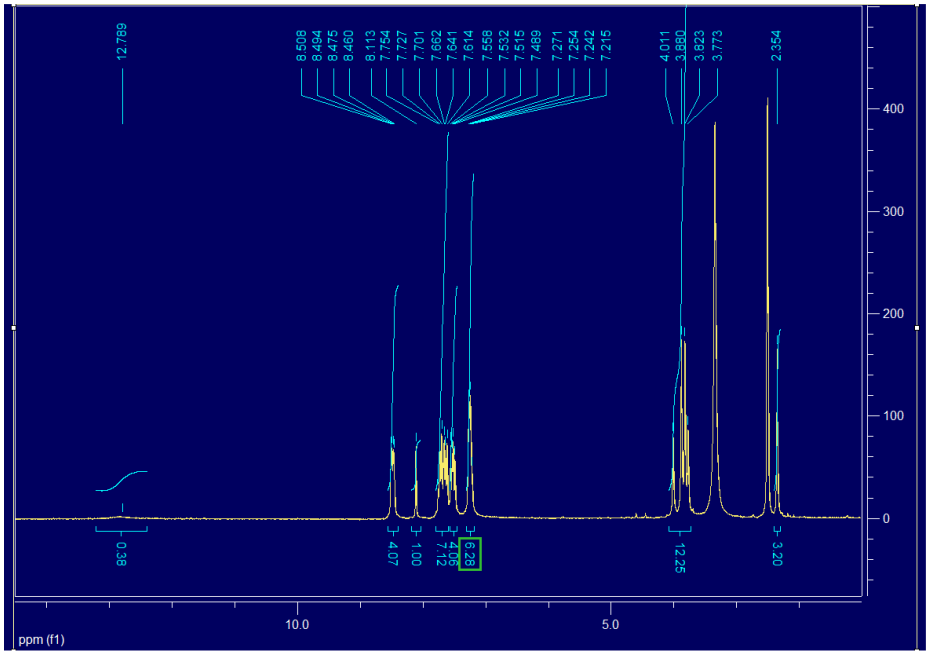

Figure S12. ^{1}H-NMR spectrum of **2**.

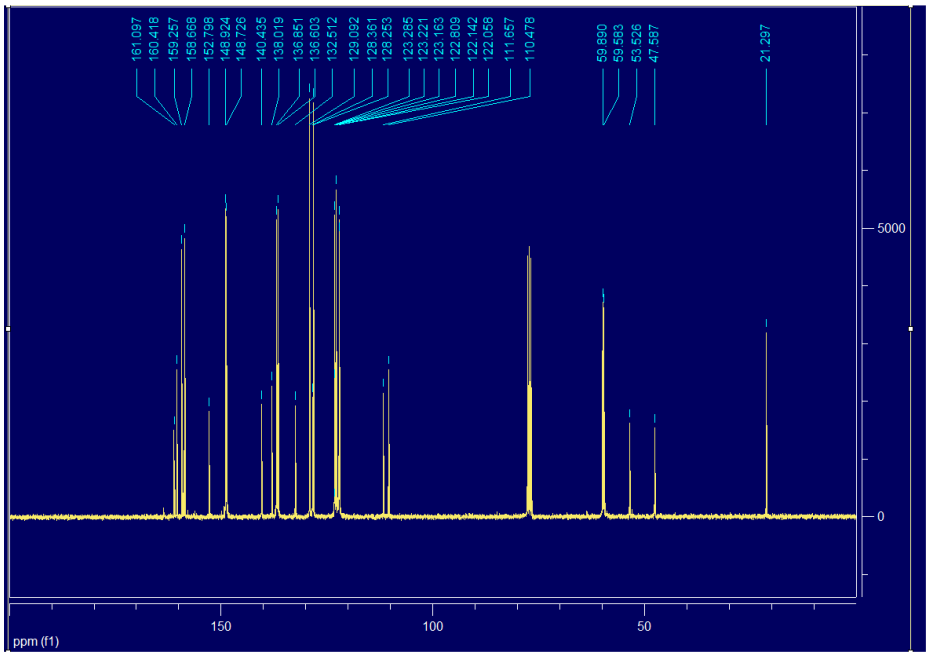

Figure S13. ^{13}C-NMR spectrum of **2**.

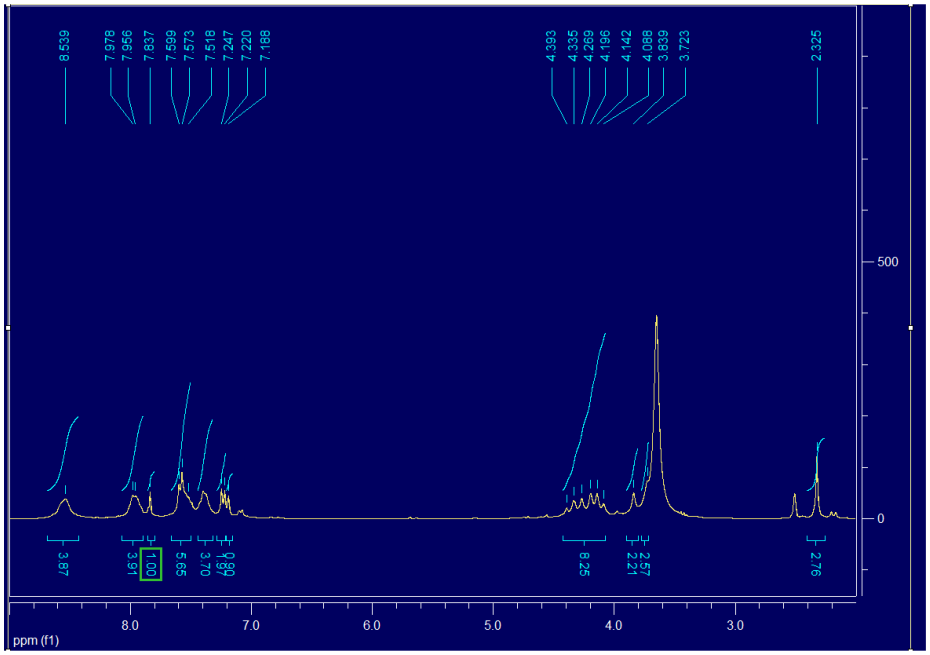

Figure S14. ^{1}H-NMR spectrum of **1**.

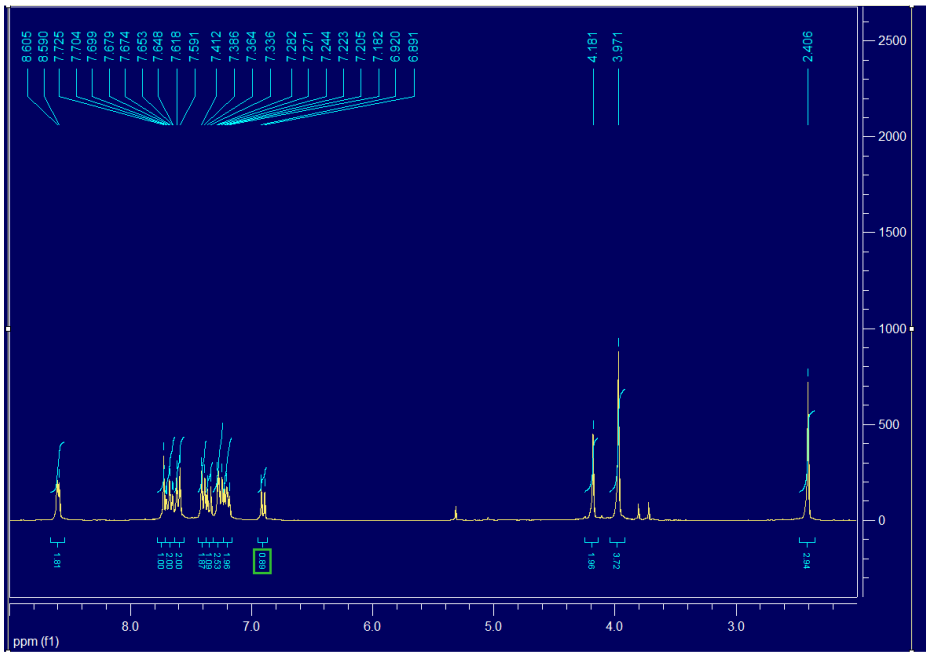

Figure S15. ^{1}H-NMR spectrum of **5**.

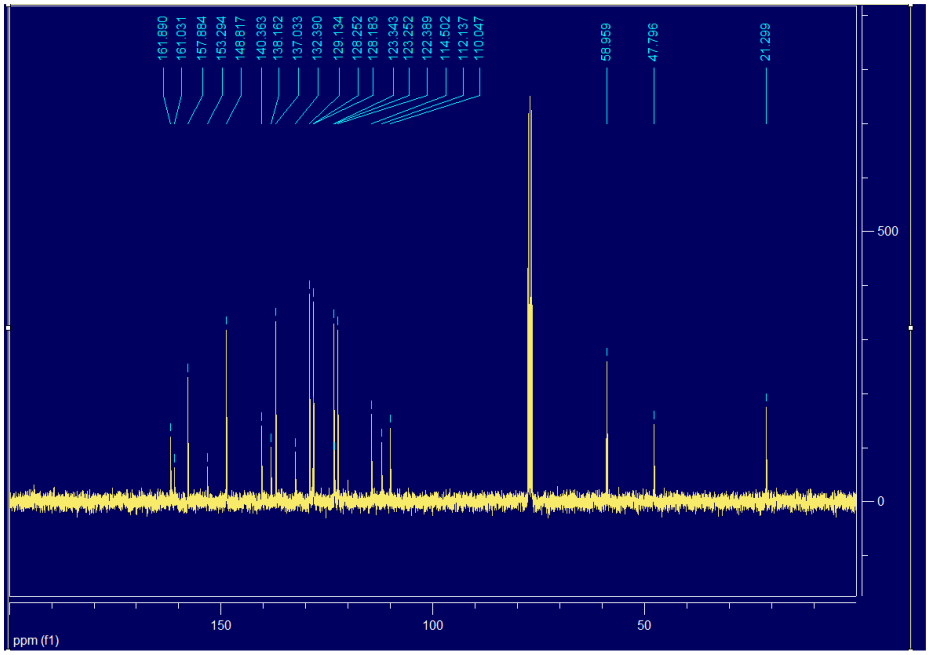

Figure S16. ^{13}C-NMR spectrum of **5**.

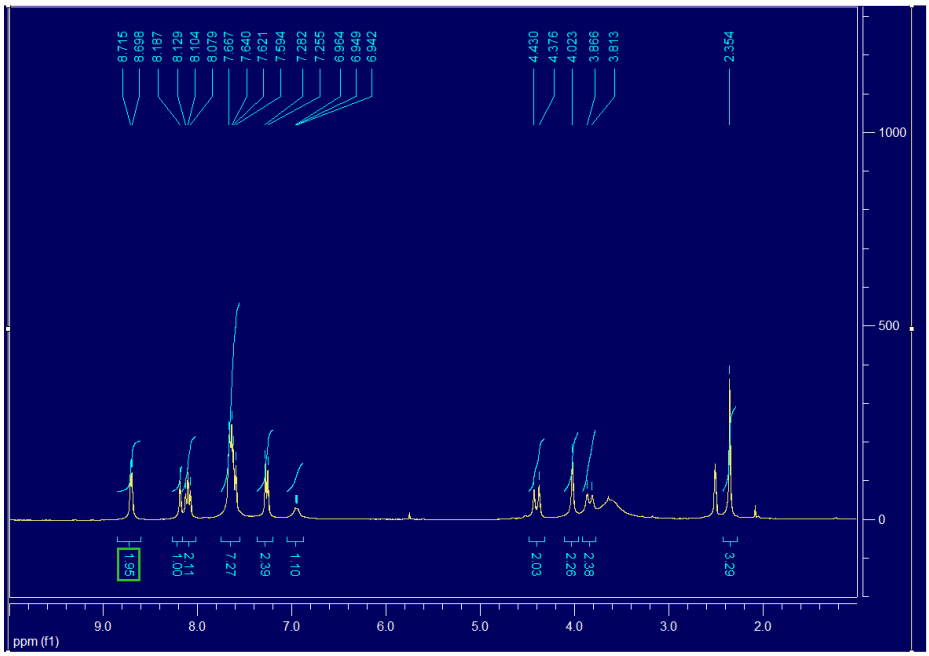

Figure S17. ^{1}H-NMR spectrum of **4**.

4.3. Preparation of GO-1 and spectroscopic measurement

The GO sheet was purchased from Sigma Aldrich. A stock solution of GO (0.1wt%) was obtained by sonicating the final product of GO for 2 h in EtOH:H_2O (1:1) solution. The mixture solution of GO and probe **1** was obtained by the addition of 100 μL of the GO stock solution (0.1wt%) to 10 mL of probe **1** solution (1 μM), and the mixture was shaken for 5 min to make a homogeneous solution. Then the mixture was centrifuged for 30 min at 4000 rpm. Resulting supernatants were collected, and aged for 2 d. Analytes was added to the GO-**1** solution (1 μM) in HEPES buffer (pH = 7.4), and the fluorescence intensity was measured with excitation at 367 nm (slit width: 5×3 nm, sensitivity: high).

4.4. Polymerase chain reaction monitoring

The primers of *C2_EGFP* (Forward primer: 5'-GAACAAGGATCCGTGAGCAAGGGCGAGGAGCT-3'; Reverse primer: 5'-CCGTAACTCGAGCGGTACAGCTCGTGCATGGC-3') was purchased from MACROGEN for the experiment of DNA amplification. The PCR was performed with the following components in a PCR micro centrifuge tube: Lyophilized HS Taq PCR Master Mix (TaKaRa), 0.2 μM final concentration of each primer, 100 ng of template DNA and 23 μL of nuclease free water. The thermal cycling program with Mastercycler started at 95°C for 2 min, then 30 s denaturation at 95°C, 45 s annealing at 55°C, 55 s elongation at 72°C and a final elongation at 72°C for another 5 m. The PCR was repeated for 10 to 15 cycles. After PCR, the reaction mixture was cooled down to room temperature. The PCR product (2−10 μL of 10−15 cycles) was added into 1 mL of GO-**1** (1

μM) in 10 mM HEPES buffer (pH = 7.4). The fluorescence change was measured at 470 nm and gel electrophoresis of PCR products was carried out on 1% agarose gel to compare the existence of amplified DNA bands and the corresponding fluorescence changes. The amplified DNA on gel electrophoresis was stained by ethidium bromide (20 μg/tube). The DNA band image was then imported into the Adobe Photoshop CS6 software to digitize the changes in fluorescence, and the mean fluorescence intensity was determined from the image histogram.

4.5. Determination of binding constant (K_a)

For reaction,

$$H + G \underset{}{\overset{K_a}{\rightleftharpoons}} HG$$

$$K_a = \frac{[HG]}{[H][G]}$$

$$K_a = \frac{[HG]}{([H]_0 - [HG])[G]} \qquad \because \ [H]_0 = [H] + [HG]$$

$$[HG] = \frac{K_a[G][H]_0}{1 + K_a[G]} \tag{1}$$

$$[G]_0 - [G] = \frac{K_a[G][H]_0}{1 + K_a[G]} \qquad \because \ [HG] = [G]_0 - [G] \tag{2}$$

, where

[H] = concentration of GO-**1** in equilibrium state

[G] = concentration of PPi in equilibrium state

[HG] = concentration of PPi bound GO-**1** in equilibrium state

$[H]_0$ = initial concentration of GO-**1**

$[G]_0$ = the added PPi concentration into the GO-**1** solution

From the equation (2), we can obtain the relation of [G] and $[G]_0$.

$$K_a[G]^2 + ([H]_0K_a - [G]_0K_a + 1)[G] - [G]_0 = 0 \quad (3)$$

From the equation (3),

$$[G] = \frac{-([H]_0K_a - [G]_0K_a + 1) + \sqrt{([H]_0K_a - [G]_0K_a + 1)^2 + 4K_a[G]_0}}{2K_a} \quad (4)$$

From the equations (1) and (4),

$$f_{(x)} = a\left[1 - \frac{2}{1 - [H]_0K_a + [G]_0K_a + \sqrt{([H]_0K_a - [G]_0K_a + 1)^2 + 4K_a[G]_0}}\right][H]_0 + c \quad (5)$$

, where *a* and *c* are arbitrary constants.

The equation (5) was applied to a nonlinear regression method using Sigma plot 8.0.[19]

5. References

(1) Ronaghi, M. *Genome Res.* **2001**, *11*, 3-11.

(2) (a) Wang, L.; Schultz, P. G. *Angew. Chem. Int. Ed.* **2005**, *44*, 34-66; (b) Park, S. G.; Ewalt, K. L.; Kim, S. *Trends Biochem. Sci* **2005**, *30*, 569-574.

(3) (a) Trifunovic, A.; Wredenberg, A.; Falkenberg, M.; Spelbrink, J. N.; Rovio, A. T.; Bruder, C. E.; Bohlooly-Y, M.; Gidlof, S.; Oldfors, A.; Wibom, R.; Tornell, J.; Jacobs, H. T.; Larsson, N.-G. *Nature* **2004**, *429*, 417-423; (b) Park, S. G.; Schimmel, P.; Kim, S. *Proc. Natl. Acad. Sci. USA* **2008**, *105*, 11043-11049; (c) Yao, P.; Fox, P. L. *EMBO Mol. Med.* **2013**, *5*, 332-343.

(4) França, L. T. C.; Carrilho, E.; Kist, T. B. L. *Q. Rev. Biophys.* **2002**, *35*, 169-200.

(5) (a) Schimmel, P. R.; Söll, D. *Annu. Rev. Biochem.* **1979**, *48*, 601-648; (b) Beebe, K.; Waas, W.; Druzina, Z.; Guo, M.; Schimmel, P. *Anal. Biochem.* **2007**, *368*, 111-121.

(6) (a) Sundberg, S. A. *Curr. Opin. Biotechnol.* **2000**, *11*, 47-53; (b) Wu, Y.-W.; Alexandrov, K.; Brunsveld, L. *Nat. Protocols* **2007**, *2*, 2704-2711.

(7) (a) Lee, D. H.; Kim, S. Y.; Hong, J.-I. *Angew. Chem. Int. Ed.* **2004**, *43*, 4777-4780; (b) Kim, S. K.; Lee, D. H.; Hong, J.-I.; Yoon, J. *Acc. Chem. Res.* **2008**, *42*, 23-31; (c) Lee, H. N.; Xu, Z.; Kim, S. K.; Swamy, K. M. K.; Kim, Y.; Kim, S.-J.; Yoon, J. *J. Am. Chem. Soc.* **2007**, *129*, 3828-3829; (d) Lee, S.; Yuen, K. K. Y.; Jolliffe, K. A.; Yoon, J. *Chem. Soc. Rev.* **2015**, *44*, 1749-1762; (e) Shin, I.-S.; Bae, S. W.; Kim, H.; Hong, J.-I. *Anal. Chem.* **2010**, *82*, 8259-8265; (f) Chen, W.-H.; Xing, Y.; Pang, Y. *Org. Lett.* **2011**, *13*, 1362-1365.

(8) Chung, C.; Kim, Y.-K.; Shin, D.; Ryoo, S.-R.; Hong, B. H.; Min, D.-H. *Acc. Chem. Res.* **2013**, *46*, 2211-2224.

(9) (a) Lu, C.-H.; Yang, H.-H.; Zhu, C.-L.; Chen, X.; Chen, G.-N. *Angew. Chem. Int. Ed.* **2009**, *48*, 4785-4787; (b) Wang, F.; Liu, C.; Fan, Y.; Wang, Y.; Li, Z. *Chem. Commun.* **2014**, *50*, 8161-8163; (c) Wang, C.; Yu, P.; Guo, S.; Mao, L.; Liu, H.; Li, Y. *Chem. Commun.* **2016**, *52*, 5629-5632; (d) Zhang, H.; Jia, S.; Lv, M.; Shi, J.; Zuo, X.; Su, S.; Wang, L.; Huang, W.; Fan, C.; Huang, Q. *Anal. Chem.* **2014**, *86*, 4047-4051.

(10) (a) Balapanuru, J.; Yang, J.-X.; Xiao, S.; Bao, Q.; Jahan, M.; Polavarapu, L.; Wei, J.; Xu, Q.-H.; Loh, K. P. *Angew. Chem. Int. Ed.* **2010**, *49*, 6549-6553; (b) Xu, Y.; Malkovskiy, A.; Pang, Y. *Chem. Commun.* **2011**, *47*, 6662-6664; (c) Gu, X.; Yang, G.; Zhang, G.; Zhang, D.; Zhu, D. *ACS Appl. Mater. Inter.* **2011**, *3*, 1175-1179.

(11) Biesinger, M. C.; Lau, L. W. M.; Gerson, A. R.; Smart, R. S. C. *Appl. Surf. Sci.* **2010**, *257*, 887-898.

(12) Ellis, A. V.; Al-deen, A.; Dalal, H.; Andersson, G. G. *J. Phys. Chem. C* **2013**, *117*, 21312-21319.

(13) Kabe, R.; Feng, X.; Adachi, C.; Müllen, K. *Chem.-Asian J.* **2014**, *9*, 3125-3129.

(14) Wu, M.; Kempaiah, R.; Huang, P.-J. J.; Maheshwari, V.; Liu, J. *Langmuir* **2011**, *27*, 2731-2738.

(15) Hu, Y.; Guo, T.; Ye, X.; Li, Q.; Guo, M.; Liu, H.; Wu, Z. *Chem. Eng. J.* **2013**, *228*, 392-397.

(16) (a) Poolman, B.; Spitzer, J. J.; Wood, J. M. *BBA-Biomembranes* **2004**, *1666*, 88-104; (b) Biemans-Oldehinkel, E.; Mahmood, N. A. B. N.; Poolman, B. *Proc. Natl. Acad. Sci. USA* **2006**, *103*, 10624-10629.

(17) Lin, W.; Yuan, L.; Cao, Z.; Feng, Y.; Song, J. *Angew. Chem. Int. Ed.* **2010**, *49*, 375−379.

(18) Rhee, H.-W.; Lee, S. H.; Shin, I.-S.; Choi, S. J.; Park, H. H.; Han, K.; Park, T. H.; Hong, J.-I. *Angew. Chem. Int. Ed.* **2010**, *49*, 4919-4923.

(19) Anslyn, E. V.; Dougherty, D. A. *Modern Physical Organic Chemistry*; University Science Books: Sausalito, CA, 2004, p 216−218.

PART III.

Push-pull π-conjugated Probes for

Paper Strip Test and Bioimaging

Background

1. Introduction

Chemosensors, which could be termed as chromogenic and fluorogenic probes, are described as a host or a reagent that can selectively bind or interact with analyte accompanied by change in its photophysical properties on the basis of structural changes.[1] They are an attractive and versatile research tool that has lately received enormous attention from modern research areas such as monitoring environmental pollution, ensuring food safety, observing cellular metabolism, and aiding in disease surveillance.[2] In the development of chemosensors, their photophysical properties can be easily and subtly controlled based on simple structural modification via synthetic processes to serve as a versatile molecular platform for corresponding applications. For example, a push-pull π-conjugated system applied on chemosensors gives rise to a large spectral change when the π-electron flow is designed to be broken upon target recognition, which is frequently used in development of chemosensors for a ratiometric and colorimetric detection in field test.[3] When focusing on live cell and tissue imaging, the use of a long wavelength excitation and emission have clear advantages over that of shorter wavelength because long wavelength light can penetrate deeper into tissues and prevent the interference of background signals derived from cellular autofluorescence. A straightforward method to access red-shifted absorption and emission is to extend the π-conjugation of the chemosensor with push-pull substituent pairs.[4] Part III describes a story about the discovery made on a push-pull π-conjugated structure of chemosensors that facilitate their practical applications to strip tests and cellular imaging.

2. Paper strip tests using chemosensors

Paper strip tests are convenient, cost-effective, and simple to use.[5] In particular, paper strips based on colorimetric and fluorometric determination have been commonly adopted in favor of direct observation by the naked-eye without the aid of any equipment, which is indeed reliable for convenient and rapid on-site detections. Among them, dipstick and lateral flow platforms can be simply prepared by immersing filter paper into a solution of chemosensors and vice versa. In this case, a chemosensor, of which target recognition induces a large spectral change, makes it helpful for precise analysis.[3,6] There are already some excellent review papers that deal with the details of device fabrication and microfluidic platforms,[5] Section 2.1 concentrates on a design strategy of chemosensors in which a push-pull π-electron system is adopted to induce large spectral changes upon chemical reaction with a target for practical applications for dipstick strips.

2.1. Paper strip test based colorimetric and fluorometric determination of bisulfite and cyanide

Michael addition between bisulfite (HSO^{3-}) and α,β-unsaturated ketone is usually used in sensing mechanism of colorimetric and fluorometric chemosensors for HSO^{3-}.[3a,6a-c] For example, Michael addition of HSO^{3-} to the synthetic probe **BICO**, consisting of a coumarin unit and benzimidazole linked through α,β-unsaturated ketone, shortens the π-conjugation and blocks the intramolecular charge transfer process (ICT) of **BICO**, which result in large spectral changes. **BICO** showed a dramatic color change from red to colorless (from 492 to 396 nm) and fluorescence change (from 622 to 460 nm).[3a] The test

strips onto which **BICO** was imposed also tested and showed color change from red to blue under UV irradiation, which are consistent with that in solution (Figure 1).

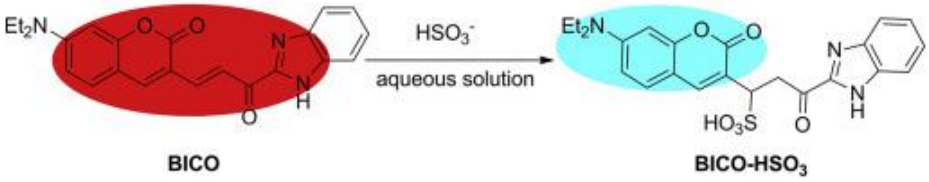

Figure 1. Proposed reaction mechanism of **BICO** for HSO^{3-}. This figure is adapted from Zhao, B.-X. *et al.*, *Anal. Chem. Acta* **2015**, *888*, 138−145.

Many of systems for cyanide (CN^-) detection commonly rely on its nucleophilic property to produce observable changes in physicochemical performances.[3b,6d-g] The reaction between the synthetic probe (**SB1**) and CN^- induced a large hypsochromic shift in absorption ($\Delta\lambda_{abs}$ = 96 nm) together with a fluorescence quenching, and simultaneously providing color changes from orange to colorless under ambient light exposure and from red to colorless under UV irradiation, due to the blocking of the push-pull π-electron flow from the diethylamino group to the dicyanovinyl group.[3b] Furthermore, the **SB1**-based test strips were easily fabricated and showed a clear color change from orange to colorless while potential competitors (other anions) exerted no considerable influence on the test strips, which is consistent with the solution test (Figure 2).

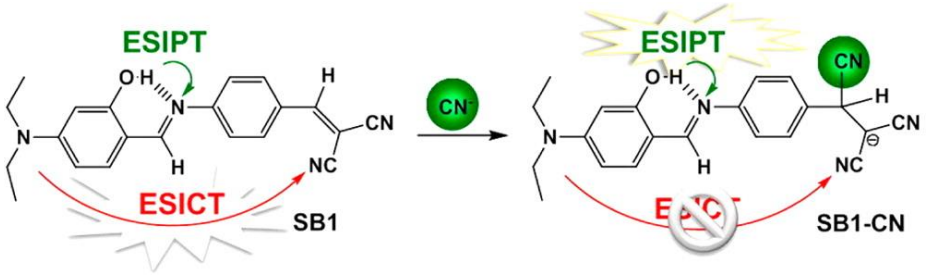

Figure 2. Proposed reaction mechanism of **SB1** for CN^-. This figure is adapted from Chen, K.-Y. *et al., Anal. Chem.* **2014**, *86*, 4648−4652.

3. Bioimaging experiment using chemosensors

For the bioimaging experiment, chemosensors of long wavelength emission (> 600 nm) have clear advantages over that of shorter wavelength because long wavelength light can penetrate deeper into tissues that makes it an attractive and less expensive alternative to classical radioisotope detection methods for molecular imaging.[4,7] Section 3.1 describes two examples of *in vitro* and *in vivo* imaging experiment in use of two near-infrared (NIR) fluorophores, cyanine and dicyanomethylene-4*H*-pyran.

3.1. Cyanine and dicyanomethylene-4*H*-pyran fluorophores for *in vitro* and *in vivo* imaging

Cyanine dyes induces fluorescence in the long wavelength region owing to a polymethine π-electron system with a donor−acceptor pair between two nitrogen atoms, where one nitrogen atom with lone pair electrons as a donor moiety and a second positively charged nitrogen atom as an acceptor is bridged by a polymethine chain.[4b] By using a nitroazo-substituted heptamethine probe (**MitoGP**), a highly selective detection of the mitochondrial GSH (mGSH) and its cellular imaging were successfully performed, where the nitroazo was

introduced as a GSH-selective reaction unit as well as a fluorescence quencher.[7b] The mGSH removed the nitroazo group from heptamethine fluorophore, exhibiting a dramatic fluorescence ON at the NIR region (λ_{max} = 810 nm) with a remarkable bathochromic shift ($\Delta\lambda_{em}$ = 46 nm), while **MitoGP** displayed no significant fluorescence changes upon presence of other biothiols (cysteine and homocysteine). A cellular imaging experiment clearly displayed that the fluorescence intensity of **MitoGP** depends on the mGSH concentration (Figure 3).

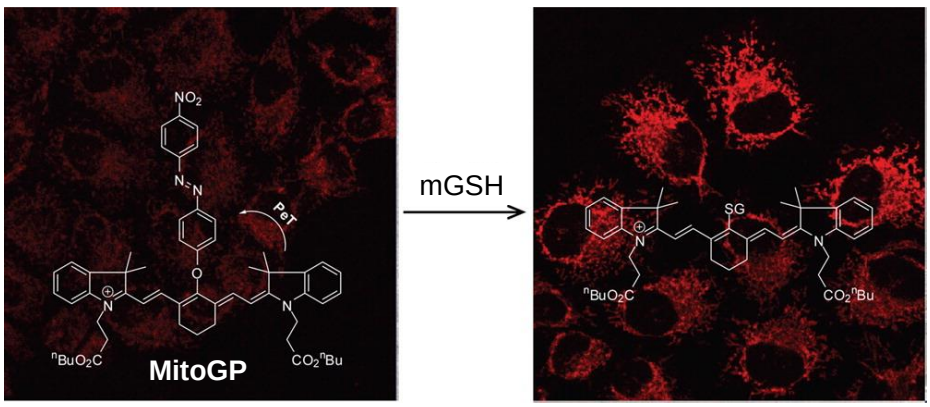

Figure 3. Proposed sensing mechanism for mGSH of **MitoGP**. This figure is adapted from Kim, H.-J. *et al., J. Am. Chem. Soc.* **2014**, *136*, 7018−7025.

Dicyanomethylene-4*H*-pyran (DCM) derivatives could perform controllable emission in the NIR region with large spectral shifts via tuning electron-donor ability of a phenol group, which offers such critical features as excellent imaging contrasts.[7c] By using a DCM-based probe (**DCM-*β*gal**) consisting of a *β*-galactosidase-responsive unit, real-time fluorescent tracking of *β*-galactosidase activity *in vitro* and *in vivo* was successfully performed.[7d] Enzymatic cleavage of the *β*-galactosidase-responsive unit leaves a free-phenol group providing favorable donor–π–acceptor characteristics, thereby increasing

the ICT effect and resulting in a new emission band in the NIR region (λ_{max} = 685 nm) with a large bathochromic shift ($\Delta\lambda_{em}$ = 185 nm). **DCM-*β*gal** also allowed for in situ and *in vivo* visualization of *β*-galactosidase activity in human colorectal tumor-bearing nude mice (Figure 4).

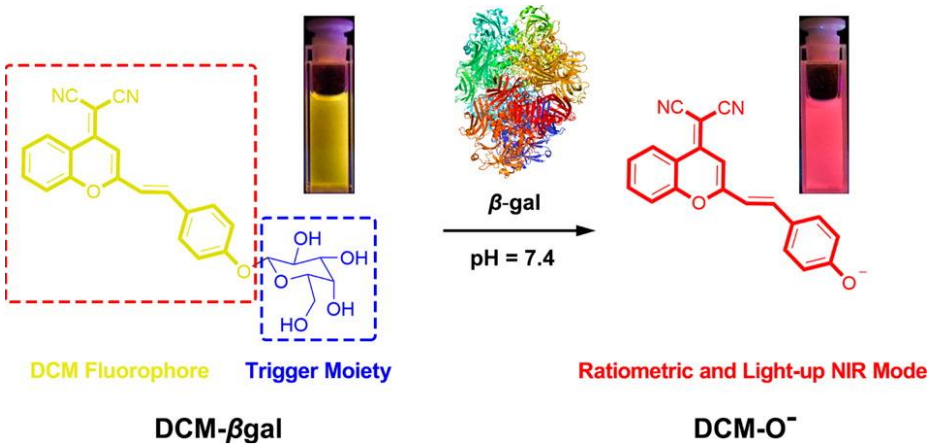

Figure 4. Proposed sensing mechanism for β-galactosidase enzymatic activation of **DCM-*β*gal**. This figure is adapted from Zhu, W.-H. *et al., J. Am. Chem. Soc.* **2016**, *138*, 5334−5340.

4. Concluding remarks

There is no doubt that the combination of the above reaction mechanisms with a rationally functionalized fluorochrome is an effective strategy to develop chromogenic and fluorogenic probes useful for various fields such as in-field tests and bioimaging. In particular, when preparing paper strips for quantitative analysis, an internal referencing system can provide a built-in correction for environmental effects and should be considered, because the quantifying process of colors, in which conversion of the camera image data into the defined RGB color spaces (e.g., CIE 1931) is involved, is influenced by external light

sources (e.g., ambient light, sun light, or smartphone LED light), giving measurement errors. For this purpose, a two-point referencing system by determining the ratio of the intensity at colored sites to a fixed intensity would be a candidate method to compensate for possible errors.[8] For bio-imaging studies, more probes with NIR features, which possesses the advantages favorable for *in vivo* imaging, should be exploited because most of the existing NIR probes are derived from cyanine dyes and suffer from poor stability. Therefore, new NIR probes with high stability and quantum yield as well as good water solubility are still desired for wider and deeper analytical use in the bio-medical research fields.

5. References

(1) (a) Li, X.; Gao, X.; Shi, W.; Ma, H. *Chem. Rev.* **2014**, *114*, 590-659; (b) Wu, J.; Kwon, B.; Liu, W.; Anslyn, E. V.; Wang, P.; Kim, J. S. *Chem. Rev.* **2015**, *115*, 7893-7943; (c) Kim, E.; Lee, Y.; Lee, S.; Park, S. B. *Acc. Chem. Res.* **2015**, *48*, 538-547; (d) Aron, A. T.; Ramos-Torres, K. M.; Cotruvo, J. A.; Chang, C. J. *Acc. Chem. Res.* **2015**, *48*, 2434-2442.

(2) (a) Khakh, B. S.; North, R. A. *Nature* **2006**, *442*, 527-532; (b) Nolan, E. M.; Lippard, S. J. *Chem. Rev.* **2008**, *108*, 3443-3480; (c) Grate, J. W.; Egorov, O. B.; O'Hara, M. J.; DeVol, T. A. *Chem. Rev.* **2008**, *108*, 543-562; (d) Carter, K. P.; Young, A. M.; Palmer, A. E. *Chem. Rev.* **2014**, *114*, 4564-4601.

(3) (a) Dai, X.; Zhang, T.; Du, Z.-F.; Cao, X.-J.; Chen, M.-Y.; Hu, S.-W.; Miao, J.-Y.; Zhao, B.-X. *Anal. Chim. Acta* **2015**, *888*, 138-145; (b) Lin, W.-C.; Fang, S.-K.; Hu, J.-W.; Tsai, H.-Y.; Chen, K.-Y. *Anal. Chem.* **2014**, *86*, 4648-4652; (c) Zhang, W.; Liu, X.; Zhang, H.; Feng, C.; Liu, C.; Yu, M.; Wei, L.; Li, Z. *J. Mater. Chem. C* **2015**, *3*, 8248-8254.

(4) (a) Kowada, T.; Maeda, H.; Kikuchi, K. *Chem. Soc. Rev.* **2015**; (b) Karton-Lifshin, N.; Albertazzi, L.; Bendikov, M.; Baran, P. S.; Shabat, D. *J. Am. Chem. Soc.* **2012**, *134*, 20412-20420; (c) Umezawa, K.; Matsui, A.; Nakamura, Y.; Citterio, D.; Suzuki, K. *Chem. Eur. J.* **2009**, *15*, 1096-1106.

(5) (a) Yetisen, A. K.; Akram, M. S.; Lowe, C. R. *Lab Chip* **2013**, *13*, 2210-2251; (b) Kumar, A. A.; Hennek, J. W.; Smith, B. S.; Kumar, S.; Beattie, P.; Jain, S.; Rolland, J. P.; Stossel, T. P.; Chunda-Liyoka, C.; Whitesides, G. M. *Angew. Chem. Int. Ed.* **2015**, *54*, 5836-5853; (c) Yamada, K.; Henares, T. G.; Suzuki, K.; Citterio, D. *Angew. Chem. Int. Ed.* **2015**, *54*, 5294-5310.

(6) (a) Tian, H.; Qian, J.; Sun, Q.; Bai, H.; Zhang, W. *Anal. Chim. Acta* **2013**, *788*, 165-170; (b) Tian, H.; Qian, J.; Sun, Q.; Jiang, C.; Zhang, R.; Zhang, W. *Analyst* **2014**, *139*, 3373-3377; (c) Sun, Y.; Zhao, D.; Fan, S.; Duan, L.; Li, R. *J. Agric. Food. Chem.* **2014**, *62*, 3405-3409; (d) Kim, S.-H.; Hong, S.-J.; Yoo, J.; Kim, S. K.; Sessler, J. L.; Lee, C.-H. *Org. Lett.* **2009**, *11*, 3626-3629; (e) Peng, M.-J.; Guo, Y.; Yang, X.-F.; Wang, L.-Y.; An, J. *Dyes Pigm.* **2013**, *98*, 327-332; (f) Hong, S.-J.; Yoo, J.; Kim, S.-H.; Kim, J. S.; Yoon, J.; Lee, C.-H. *Chem. Commun.* **2009**, 189-191; (g) Zhou, X.; Lv, X.; Hao, J.; Liu, D.; Guo, W. *Dyes Pigm.* **2012**, *95*, 168-173.

(7) (a) Zhang, D.; Martin, V.; Garcia-Moreno, I.; Costela, A.; Perez-Ojeda, M. E.; Xiao, Y. *Phys. Chem. Chem. Phys.* **2011**, *13*, 13026-13033; (b) Lim, S.-Y.; Hong, K.-H.; Kim, D. I.; Kwon, H.; Kim, H.-J. *J. Am. Chem. Soc.* **2014**, *136*, 7018-7025; (c) Wu, X.; Sun, X.; Guo, Z.; Tang, J.; Shen, Y.; James, T. D.; Tian, H.; Zhu, W. *J. Am. Chem. Soc.* **2014**, *136*, 3579-3588; (d) Gu, K.; Xu, Y.; Li, H.; Guo, Z.; Zhu, S.; Zhu, S.; Shi, P.; James, T. D.; Tian, H.; Zhu, W.-H. *J. Am. Chem. Soc.* **2016**, *138*, 5334-5340.

(8) Ashokkumar, P.; Weißhoff, H.; Kraus, W.; Rurack, K. *Angew. Chem. Int.*

Ed. **2014**, *53*, 2225-2229.

Section 1.

Paper strip based fluorometric determination of cyanide with internal reference

Abstract

The rapid, selective, and sensitive determination of cyanide anion (CN^-) using a simple paper strip is highly attractive because cyanide is acutely lethal to living organisms via all routes of administration, including alcohol consumption and inhaling cigarette smoke. Here, a synthetic probe **1** was designed for the selective determination of cyanide. The probe displays rapid and large blue spectral change ($\Delta\lambda_{abs}$ = 148 nm, $\Delta\lambda_{em}$ = 165 nm) with respect to target recognition. Probe **1** exhibits a strong push–pull electronic effect and comprises a dimethylaminoaryl group as a donor and malononitrile as an acceptor; the π-conjugation system can be destroyed by the Michael-type addition of cyanide at the electrophilic β-positions of the nitrile groups, resulting in the marked emergence of a peak at λ_{em} = 515 nm. The developed probe was successfully applied to a paper test strip because of its noticeable optical changes upon reaction with cyanide. The fabricated dumbbell-shaped paper strip with an internal reference allowed the cyanide detection, which is indispensable for quantitative analysis in point-of-care testing. The paper strip test showed selective response to cyanide with a linear correlation in the range of 0–25 mM in a simple and cost-effective manner.

1. Introduction

Cyanide is extremely toxic to mammals, primarily because it impairs the mitochondrial respiratory chain. This results from the strong coordination of

cyanide to iron at the heme active site in cytochrome oxidase, whereby it inhibits the aerobic production of adenine triphosphate.[1] Cyanide poisoning is also closely related to cardiovascular and central nervous system disorders.[2] According to previous reports, the LD_{50} values of hydrogen cyanide for human intake and dermal exposure are 1.0 and 100 mg/kg, respectively.[3] Cyanide can cause serious problems when it is accidentally released in operations such as gold cyanidation and industrial organic chemistry for nylon production and in certain areas of architecture; therefore, cyanides should be controlled with extreme precaution.[4]

Various potentiometric,[5] voltammetric,[6] chromatographic,[7] or fluorescence detection methods[8] have been reported for cyanide determination. Although these techniques meet most legislative requirements, they are operationally complex and time-consuming and often require significant preconcentration and/or organic solvents. Consequently, alternative and more sensitive methods that can directly measure cyanide from sub-μg/L to mg/L levels in different matrices are desirable. Among them, fluorescence determination shows promise because of its favorable sensitivity, operating cost, and operating process. Jang *et al*. recently described a cyanide probe that utilizes the nucleophilic attack of cyanide, resulting in strong fluorescence in aqueous conditions.[8a] Moreover, tremendous efforts have been devoted to the fluorescence determination of cyanides.[9] For several decades, paper-based sensors have attracted considerable attention because they can be easily utilized by the public for field testing.[10] Paper test strips are popular in the diagnostics field because of their low cost, light weight, portability, and ability to produce a rapid and easy-to-read answer. A simple point-of-care test for the rapid quantification of cyanide is also of great value in clinical examinations and

forensic investigations because cyanide exposure can occur frequently in daily life.

Here, a paper test strip that employs a cyanide-sensitive optical probe was prepared for the quantitative determination of cyanide. The synthetic probe **1** has an electron push–pull-type structure containing a dimethylamino group as an electron donor and malononitrile as an electron acceptor. Probe **1** acts as a fluorescent chemodosimeter toward cyanide; the strongly nucleophilic cyanide reacts with the electrophilic methylenemalononitrile group of probe **1** to form **1**-CN via a Michael-type conjugate addition, thereby generating ratiometric optical signal changes (Scheme 1). The addition of the cyanide anion breaks the π-conjugation, which decreases the dipole moment and results in the large spectral blue shift in the probe **1**. These photophysical changes enable the naked-eye determination for cyanide; thus, probe **1** can be utilized for detecting cyanide in paper-based sensors. We fabricated a dumbbell-shaped, simple paper device that allows the two-point referencing detection for cyanide. The rapid, quantitative determination of cyanide in the linear range of 0–25 mM was achieved on the internally referenced test strip in a simple and cost-effective manner.

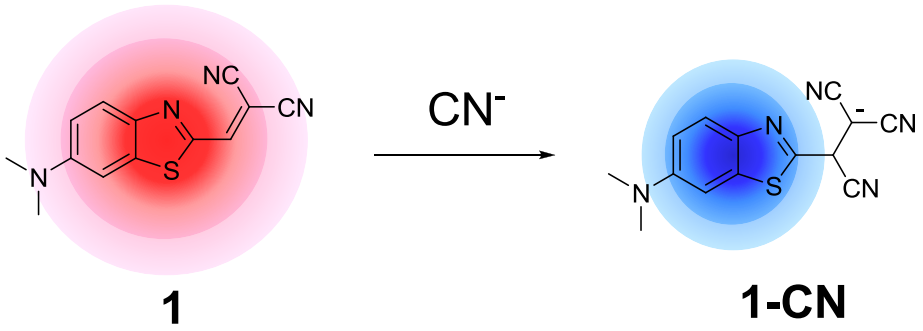

Scheme 1. Cyanide probing concept of **1**.

2. Data and results

2.1. Design concept of probe

The probe **1** was designed to have an electron push–pull conjugated structure consisting of electron donor and acceptor moieties. 6-(Dimethylamino)-1,3-benzothiazole and malononitrile were connected through a methylene linkage comprising electron deficient sites on the β-positions of the nitrile groups. Cyanide anion is strongly nucleophilic and is thus expected to attack the most electron deficient site (Scheme 1). Thus, the synthetic probe **1** is fully π-conjugated from the dimethylamino group to the malononitrile group. Upon the administration of cyanide via Michael-type addition to probe **1**, the electrophilic vinyl site is attacked by the strongly nucleophilic cyanide, consequently destroying the conjugated structure and decreasing the magnitude of the molecular dipole moment from **1** to **1**-CN (Figure 1).[8a] The decreased dipole moment would alter the HOMO–LUMO energy band gap (Figure 9), changing the photophysical properties.

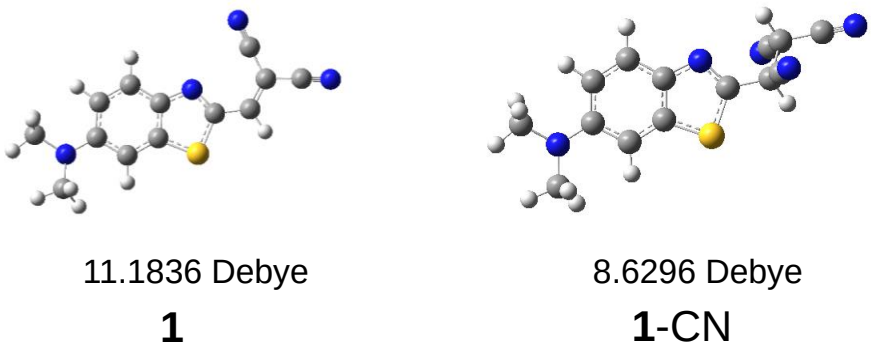

Figure 1. Dipole moments of **1** (11.1836 D) and **1**-CN (8.6296 D) calculated using DFT.

2.2. Synthesis and photophysical properties of 1

The probe **1** was prepared according to the previously reported synthesis procedure with a 28% overall yield.[11] As expected, **1** showed a reddish color in the DMSO solution because of the inherently strong electronic push–pull effect. Upon adding increasing amounts of cyanide, the absorbance of **1** at approximately 530 nm decreased, whereas the absorbance at approximately 382 nm increased. Three pseudo-isosbestic points were observed at 293, 324, and 437 nm, indicating a 1:1 reaction stoichiometry (Figure 2a). The absorbance change is completed upon the addition of 1 equiv. of cyanide (inset of Figure 2a). Similar to the large spectral shift (148 nm) observed in the absorbance spectra, the fluorescence spectra exhibited ratiometric changes with pseudo-isoemissive points at 617 nm upon excitation at 400 nm as well as with saturation upon the addition of 1 equiv. cyanide (Figure 2b). Cyanide showed selective response to probe **1** over other competitive analytes including SH^-, HPO_4^{2-}, OAc^-, N_3^-, F^-, Cl^-, and Br^- (Figure 3a). The reddish solution of **1** dramatically changed to a transparent solution upon the addition of cyanide, whereas other analytes showed no significant color changes (Figure 3b). The color change was confirmed by the UV–Vis spectra, in which the absorption maximum at approximately 530 nm changed only in the presence of cyanide (Figure 4a). Thus, the ratiometric probe **1** simultaneously records two emission peaks at 550 and 680 nm in the presence and absence of cyanide, allowing the accurate quantitative analysis of cyanide. The probe shows an approximately eight-fold greater ratiometric fluorescence response (550 nm/680 nm) to cyanide compared to the other analytes (Figure 3a). The fluorescence measurements in the presence of the other competitive analytes revealed a

selective response and reactivity for cyanide without any interference (Figures 3a and 4b).

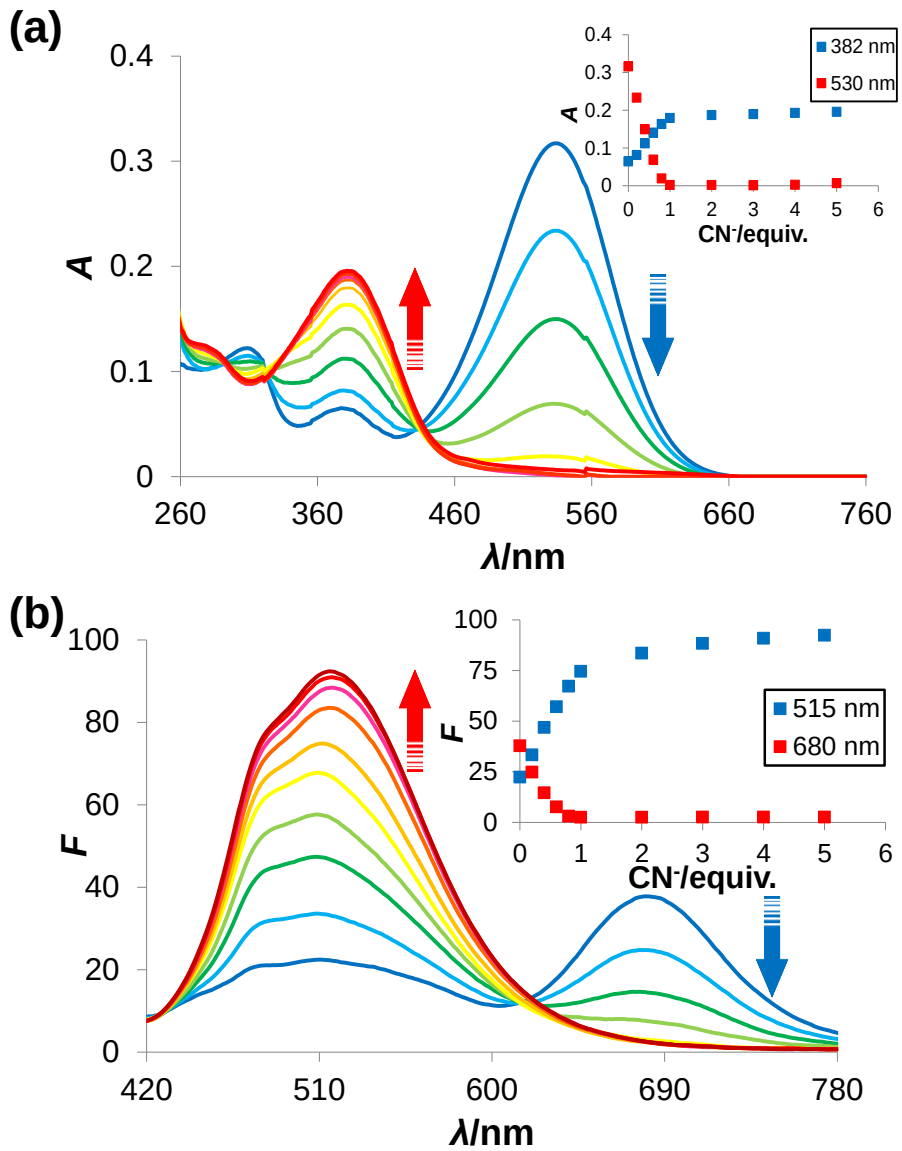

Figure 2. Absorbance (a) and fluorescence (b) changes of **1** (5 μM) upon titration with tetrabutylammonium cyanide (0–25 μM) in DMSO. Inset shows the absorbance intensities at 382 and 530 nm (a) and emission intensities at 515 and 680 nm (b) of **1** with cumulative cyanide addition (excitation: 400 nm, slit width: 5 × 5 nm).

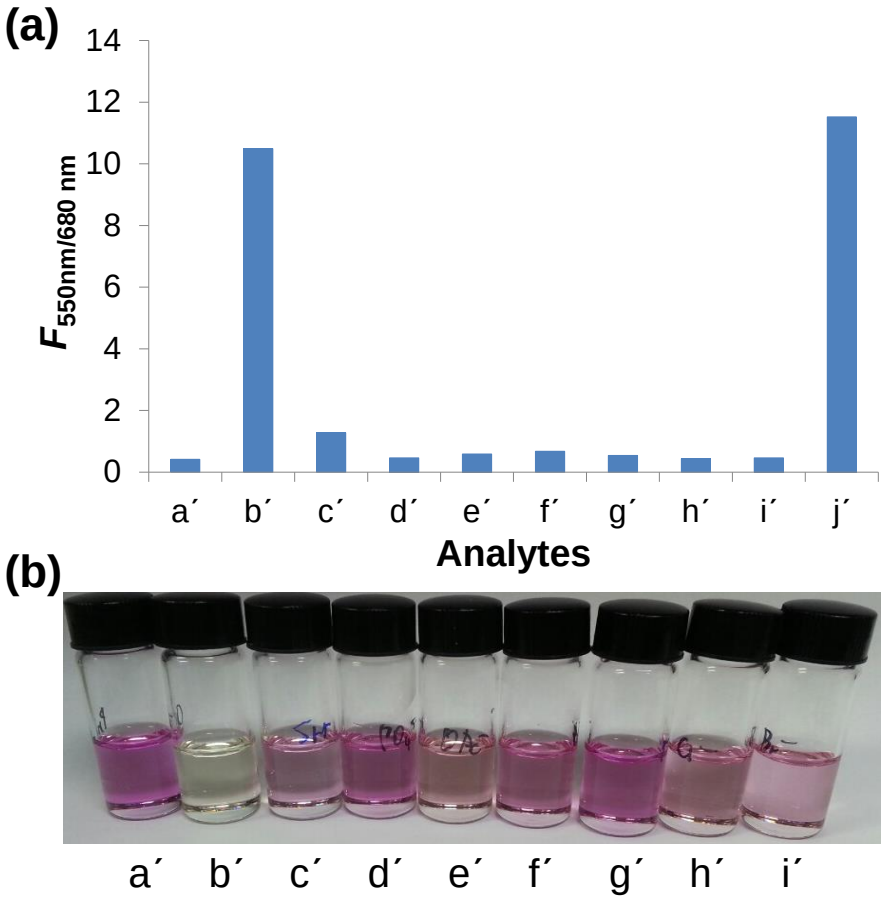

Figure 3. a) Fluorescence intensity ratio ($F_{550\ nm}/F_{680\ nm}$) of **1** (5 μM) in the presence of analytes (20 equiv. except for cyanide) in DMSO: (a´) probe **1**, (b´) CN^- (2 equiv.), (c´) SH^-, (d´) HPO_4^{2-}, (e´) OAc^-, (f´) N_3^-, (g´) F^-, (h´) Cl^-, (i´) Br^-, and (j´) all mixed analytes and the subsequent addition of 2 equiv. cyanide (excitation: 400 nm, slit width: 5 × 5 nm). b) The corresponding photographs.

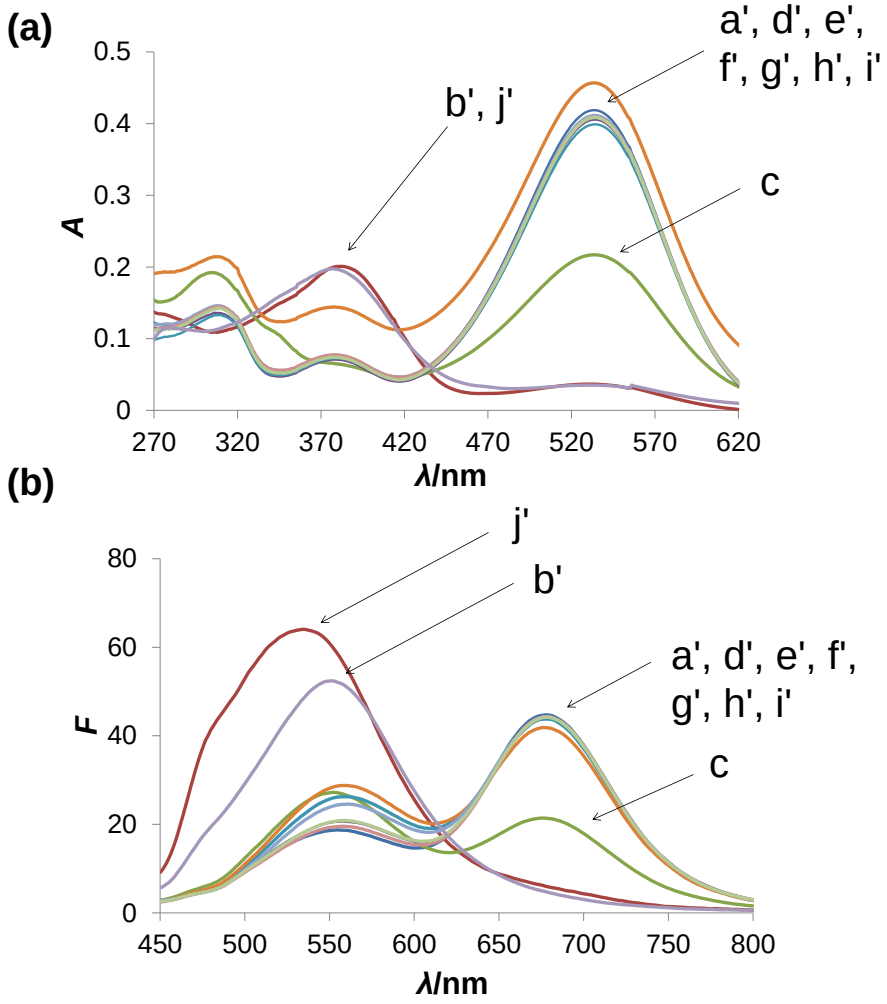

Figure. 4. Absorption (a) and fluorescence emission (b) spectra of **1** (5 μM in DMSO) in the presence of competitive analytes: (a') Probe only, (b') CN^-, (c') SH^-, (d') HPO_4^{2-}, (e') OAc^-, (f') N_3^-, (g') F^-, (h') Cl^-, (i') Br^-, (j') subsequent addition of CN^- (2 equiv.) into the mixture of all of the competitive analytes (20 equiv. each). The selectivity test was performed with 20 equiv. of other analytes except for cyanide (2 equiv.) (ex: 400 nm, slit width: 5×5 nm).

2.3. Paper strip sensor

Since probe **1** showed a large spectral shift upon cyanide addition, it was expected to be applicable to a simple paper strip. We prepared a dumbbell-shaped lateral flow format on a filter paper, and three distributable sites (sample loading site, detection site, and crosslinking fluidic channel) were simply patterned on the paper using a wax-based inkjet printer. Aqueous samples introduced onto the sample loading site could travel to the detection site through the crosslinking fluidic channel, leading to chemical reaction of the loaded sample with the imposed probe at the detection site (Figure 5). The fabricated

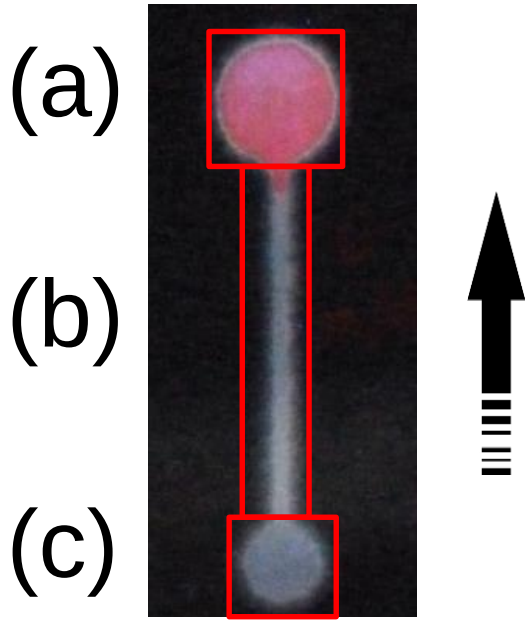

Figure 5. Dumbbell-shaped model of paper strips. The strips are made up of three distributable sites: (a) detection site, (b) crosslinking fluidic channel, (c) sample loading site. 1.2 μL of probe **1** solution in acetonitrile (5 mM) was imposed onto (a) site. 10 μL of analyte solution in water was introduced onto (c) site, leading to subsequent flow through (b) channel. The arrow indicates the flow.

paper device showed fluorogenic and colorimetric changes upon the addition of cyanide. Most importantly, the strips allowed a two-point referencing system by determining the ratio of the intensity at the detection site to the intensity at the sample loading site (a/c in Figure 5). This allows the compensation of possible errors caused by external light sources, which is indispensable for quantitative detection during field testing.[12] From the integrated fluorescence data processed by PC software, a linear correlation was obtained for cyanide concentrations in the range of 0–25 mM ($y = 0.0725x$, $R^2 = 0.99$; inset of Figure 6a). The limit of detection (LOD) was determined to be 1.6 mM (41.4 ppm; signal/noise ratio = 3, $n = 5$). Although The LOD did not reach a practically meaningful range (0.2 ppm in drinking water, US EPA), for the first time, the fabricated paper strip provides a model system to design matrices for *quantitative field tests for cyanide* with an internal reference. From comparative selectivity assays, the paper strip exhibits no significant response to other analytes including SH^-, HPO_4^{2-}, OAc^-, N_3^-, F^-, Cl^-, and Br^-, indicating that the fabricated strip has the potential for cyanide determination in the field (Figure 7).

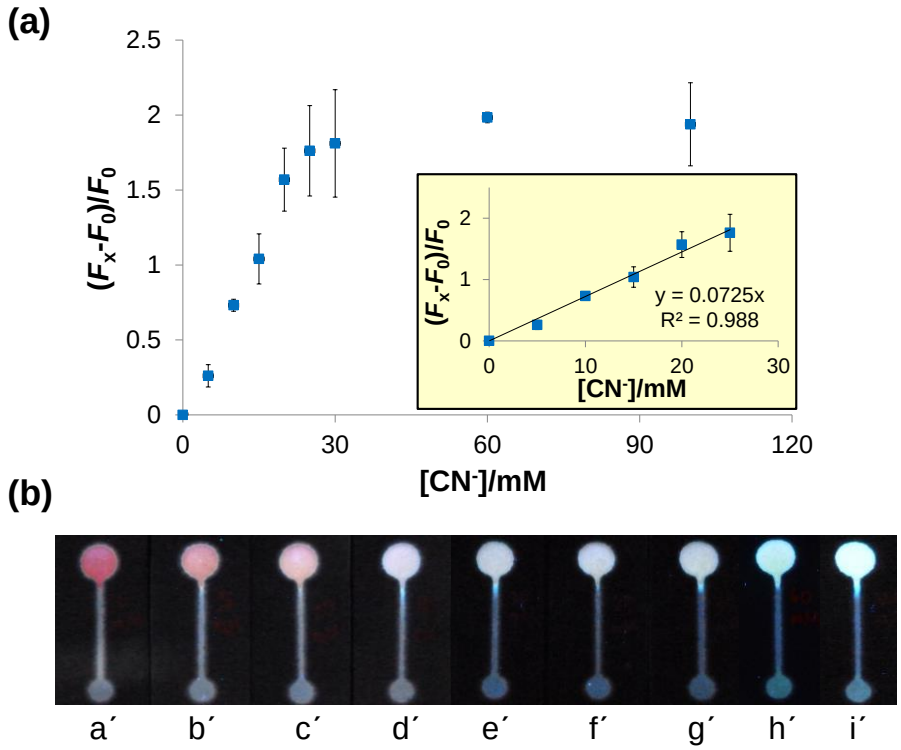

Figure 6. a) Paper-strip-based quantitative detection of cyanide (0–100 mM). The intensity was internally referenced by measuring the ratio of the intensities of the two circles (detection site/sample loading site). F_x = the intensity ratio of the two circles upon cyanide loading; F_0 = the intensity ratio on probe **1**. The plot shows the saturation point at 30 mM cyanide, and the error bar represents the standard deviation obtained from three sets of independent measurements. The inset yellow box shows a linear range from 0 to 25 mM of cyanide (R^2 = 0.9891). b) The corresponding photographs according to the cyanide concentration under UV irradiation: (a´) 0, (b´) 5, (c´) 10, (d´) 15, (e´) 20, (f´) 25, (g´) 30, (h´) 60, and (i´) 100 mM of CN^-.

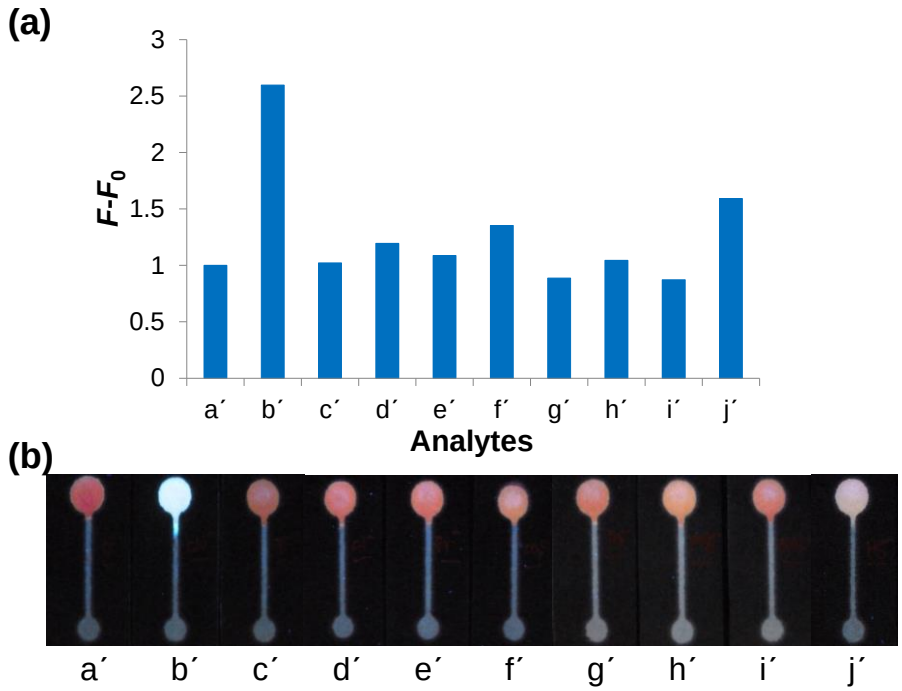

Figure 7. a) Paper-strip-based fluorogenic intensity ratio (F/F_0) upon administration of various anions (30 mM in 100 mM PBS buffer): (a´) probe **1**, (b´) CN^-, (c´) F^-, (d´) Cl^-, (e´) Br^-, (f´) HCO_3^- (g´) N_3^-, (h´) HPO_4^{2-}, (i´) OAc^-, and (j´) SH^-. The intensity was internally referenced by measuring the intensity ratio of the two circles (detection site/sample loading site). F = the intensity ratio of the two circles upon each analyte loading; F_0 = the intensity ratio on probe **1**. b) The corresponding photographs.

2.4. NMR experiment

^{1}H NMR was used to clarify the mechanism of cyanide detection. Upon the addition of increasing amounts of cyanide (0–1.0 equiv.) into the solution of **1** in DMSO-d_6, one singlet peak at 8.6 ppm gradually disappeared, while a new singlet signal began to appear in the up-field region at 6.4 ppm. This result indicates that cyanide participates in the conjugate addition reaction at the most electron deficient β-position of the nitrile groups to form **1**-CN, in which the β-

olefinic carbon is converted to an sp^3 carbon attached to the incoming CN. Thus, the signal of the newly formed cyanomethine should appear far up-field compared to that of the original vinyl proton (Figure 8).

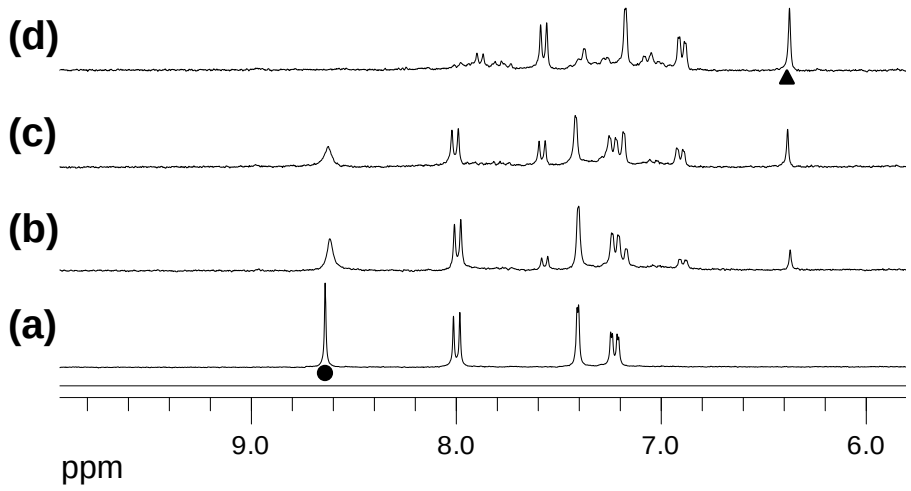

Figure 8. ^{1}H NMR spectra of **1** (10 mM) upon titration with tetrabutylammonium cyanide (TBAC) in DMSO-d_6: (a) 0, (b) 0.4, (c) 0.6, and (d) 1.0 equiv. of cyanide. The circle in (a) and triangle in (d) denote a vinyl proton in **1** and a cyanomethine proton in **1**-CN, respectively.

2.5. DFT calculation

To obtain more insights into the mechanism, we examined the changes in the theoretical energy band gap using density function theory (DFT) computations at the B3LYP/6-31+G* level of theory using the Gaussian09 program. The optimized geometry of **1** maintains a fully π-conjugated planar structure from the dimethylamino group to the methylenemalononitrile group, whereas the π-conjugation length in the cyanide adduct **1**-CN is shortened by the conversion of the π-conjugated methylene linker to the saturated aliphatic group, resulting in the breaking of the π-conjugated system (Figure 1). The DFT calculations

reveal that the addition of cyanide changes the theoretical electronic transition energy (ΔE_{calcd}) from 2.78 eV in **1** to 4.09 eV in **1**-CN (Figure 9). The change in electronic transition energy ($\Delta\Delta E_{calcd}$ = 1.31 eV) can be converted to absorbance shift ($\Delta\lambda_{max,\ calcd}$ = 147 nm) via the Planck–Einstein relation;[13] this calculated shift is close to the experimentally observed change in absorbance $\Delta\lambda_{max,\ exp}$ = 151 nm (Figure 2a).

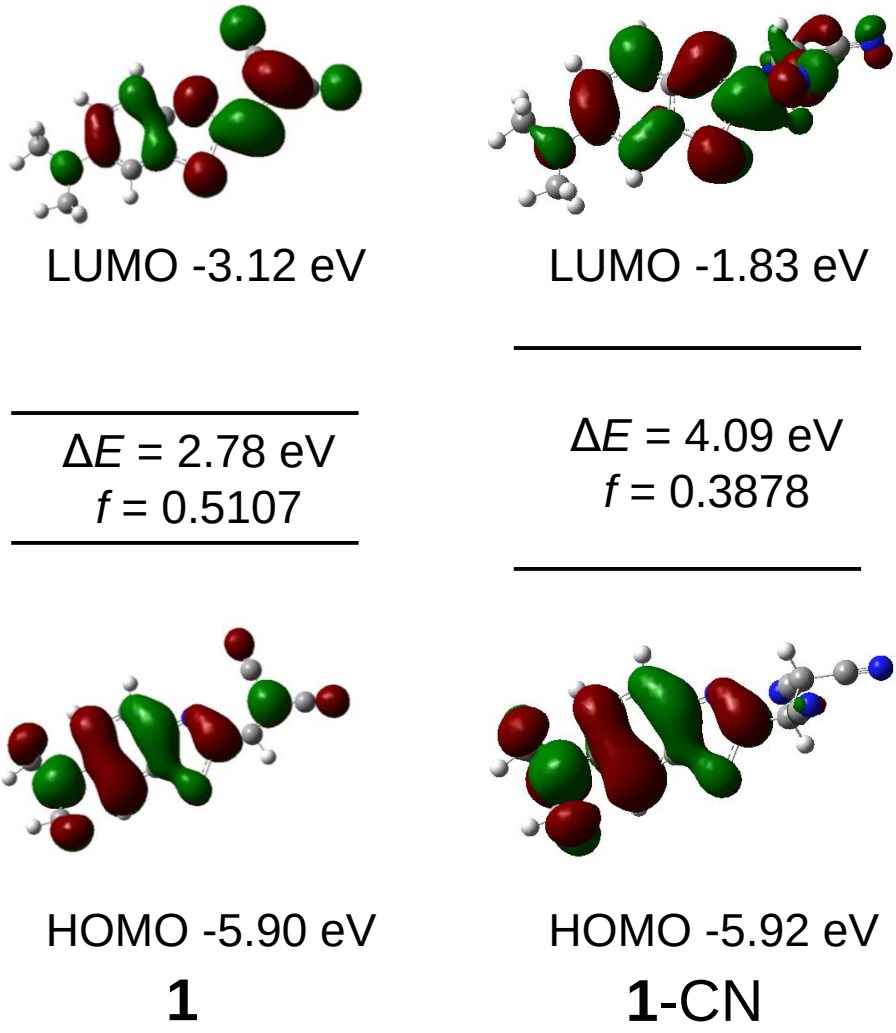

Figure 9. The HOMO and LUMO levels of **1** and **1**-CN and their corresponding frontier orbitals calculated using DFT. *f* is the calculated oscillator strength.

3. Conclusion

In this study, an electron push–pull type chemodosimetric probe **1** showed the selective optical response to cyanide. The large spectral shift of **1** was induced by alterations in the π-conjugated system, including the conjugation length and the magnitude of dipole moment, because of the nucleophilic attack by cyanide on the most electron deficient sites, the *β*-positions of the nitrile groups in **1**. The large optical signal change of probe **1** upon the addition of cyanide was successfully developed into paper strips for determining cyanide in the field. The paper strip employing **1** showed selective sensing behaviour toward cyanide. More importantly, the internally referenced system developed by the two-point measurement of the dumbbell-shaped strips facilitated the quantification analysis of cyanide in the field. The accurately described strip test would provide a reader-friendly guide to go about the point-of-care testing method for the determination of cyanide as well as other relevant targets.

4. Experimental

4.1. Synthesis procedure for ((6-(dimethylamino)-1,3-benzothiazol-2-yl)methylene)malononitrile (1)

Probe **1** was prepared following a previously reported synthesis procedure (Scheme 2).[11] To a solution of 6-(dimethylamino)-1,3-benzothiazole-2-carbaldehyde (**2**)[11] (160 mg, 0.78 mmol) in 2-propanol (9.75 mL), malononitrile (77.3 mg, 1.17 mmol) and pyridine (0.16 mL) were added. The mixture was stirred for 1.5 h at 90°C. The reaction mixture was cooled to room temperature (RT) and H_2O was subsequently poured into the mixture to quench the reaction. The mixture was extracted three times with $CHCl_3$, and the combined organic

layer was dried over Na_2SO_4. All volatiles were evaporated under reduced pressure. The resulting crude product was purified by flash column chromatography with dichloromethane:methanol (20:1) as eluent to give a violet solid (89% yield). ^{1}H NMR (300 MHz, DMSO-d_6) δ 8.61 (s, 1H), 7.97 (d, J = 9.2 Hz, 1H), 7.37 (d, J = 2.4 Hz, 1H), 7.2 (dd, J = 9.2, 2.4 Hz, 1H), 3.07 (s, 6H); ^{13}C NMR (75 MHz, DMSO-d_6) δ 151.2, 151.1, 151.0, 145.3, 141.4, 125.9, 116.4, 114.8, 113.9, 101.7, 80.4; HRMS (FAB$^+$, m-NBA) m/z calcd for $C_{13}H_{11}N_4S$: 255.0704, observed: 255.0705.

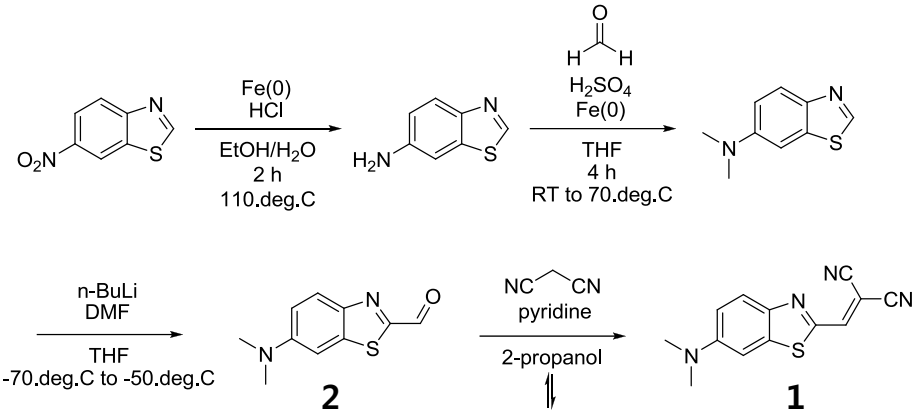

Scheme 2. Synthetic route of probe **1**.

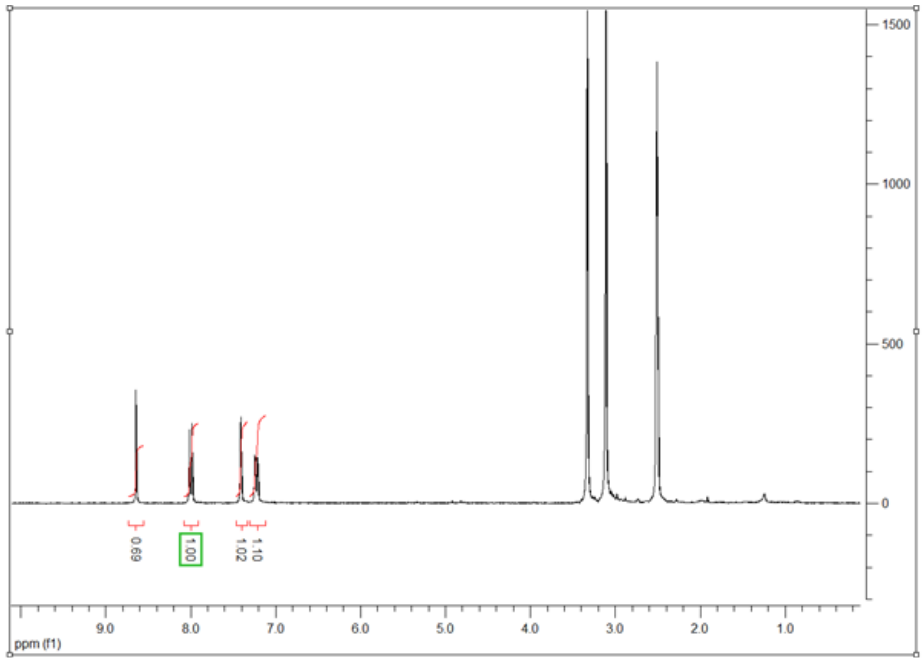

Figure 10. [1]H-NMR spectrum of **1**.

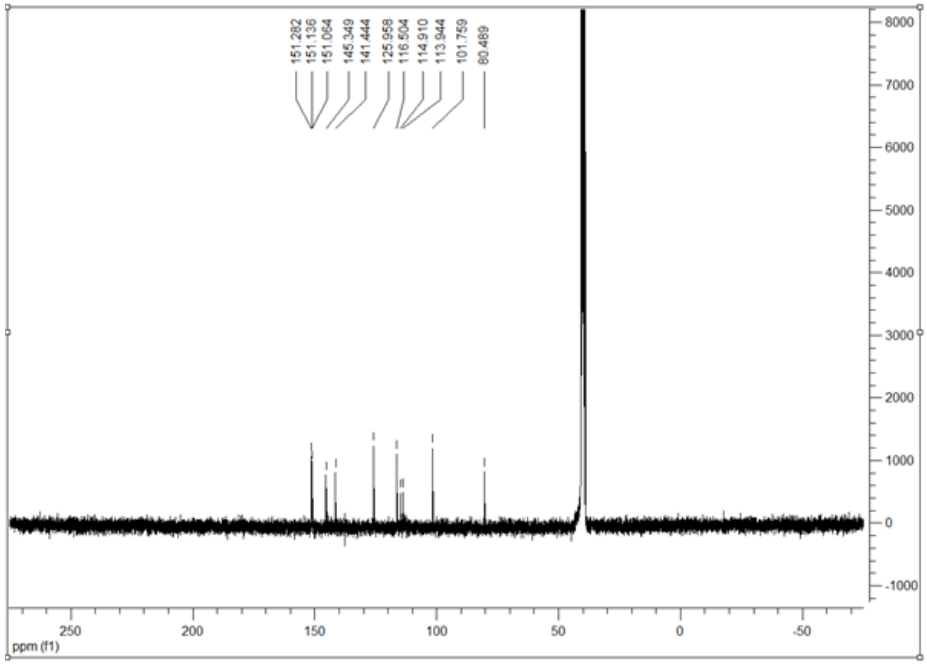

Figure 11. [13]C-NMR spectrum of **1**.

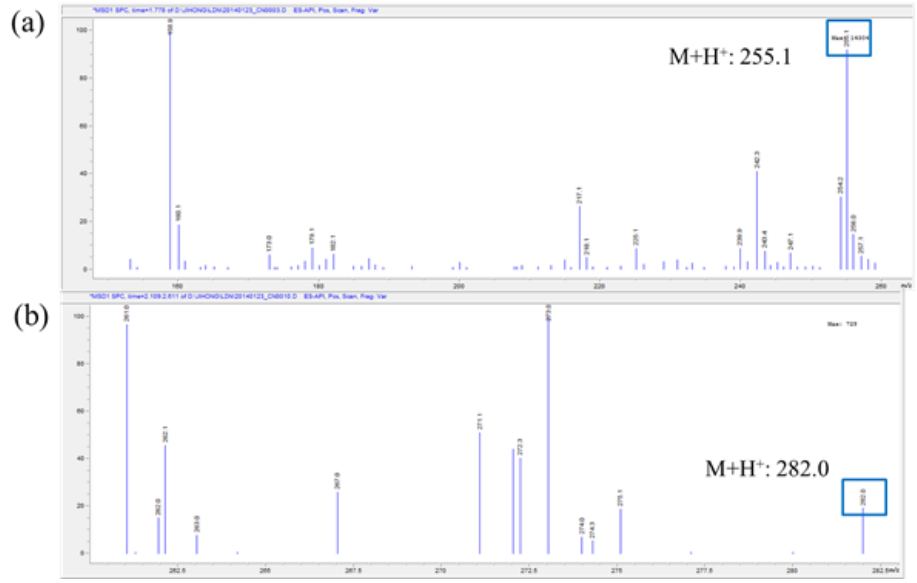

Figure 12. Mass spectra of (a) **1** and (b) **1**-CN.

4.2. Photophysical property measurements

A 10 mM stock solution of **1** was prepared in DMSO; however, the solution appeared to be unstable even on exposure to ambient light because of the labile nature of the vinyl linker.[14] Thus, all the experiments were performed with the solution carefully wrapped in aluminum foil to protect the solution from ambient light. The solution was diluted to 5 μM in DMSO just before photophysical measurements. The cyanide titration experiment was performed by adding increasing amounts of tetrabutylammonium cyanide (TBAC, 0−25 μM) to the solution of **1** (5 μM in DMSO). Each mixture was measured using Beckman Coulter DU 800 spectrometer and Jasco FP 6500 fluorescence spectrometer. Photophysical response to each analyte was estimated by adding each analyte (sodium salt, 2 equiv. of cyanide, 20 equiv. of other analytes) into each aliquot of solution of **1** (5 μM in DMSO). A competition experiment was performed by adding 2 equiv. of cyanide into the mixture of all analytes (each

20 equiv.) in **1** (5 μM in DMSO). The fluorescence experiment was performed by excitation at 400 nm (slit width: 5 × 5 nm).

4.3. Paper-based sensor

A dumbbell-shaped hydrophilic pattern was tailored using the Microsoft PowerPoint software (Figure 5). The crosslinking channel on the paper was approximately 1.6 cm in length and 0.2 cm in width. A large circle with a diameter of 0.7 cm and a small circle with a diameter of 0.5 cm were drawn on the top and bottom of the crosslinking channel, respectively. The tailored dumbbell shape was printed with wax-based solid ink on Whatman chromatography paper using a Xerox 8570DN inkjet printer. After the paper was heated by placing it on a hot plate with the wax side up for 15 s at 120°C and then cooled to RT, the dumbbell-shaped hydrophilic pattern was completely separated from the wax printed hydrophobic site.[15] A solution of probe **1** in acetonitrile (1.2 μL, 5 mM) was dropped onto a detection site (large circle; a in Figure 5) and dried for 5 min. Then, 10 μL of various NaCN solutions in water (0–100 mM) was introduced onto the sample loading site (small circle; c in Figure 5). The sample droplet reached the detection site through the crosslinking channel and then the paper device was dried for 1 h. The fluorescence intensity changes on the paper were measured by irradiation at 365 nm (6 W) using a hand-held UV lamp (Spectroline, ENF-260C). The paper strip was irradiated with UV light and photographed. The image was then imported into the Adobe Photoshop CS6 software to digitize the changes in fluorescence. The images were then transformed to gray-scale, and the mean fluorescence intensity was determined from the image histogram. To compensate for measurement errors caused by various light sources, an internal

standard was introduced by measuring the intensity on the sample loading circle because both circles (i.e., the detection and sample loading sites) will be equally affected by the light source.[12] Thus, all data were internally referenced by measuring the ratio of intensity at the detection site to the intensity at the sample loading site. To test the selectivity of the paper strips, 30 mM of CN^-, SH^-, HPO_4^{2-}, OAc^-, N_3^-, F^-, Cl^-, and Br^- solutions (sodium salt) were prepared in 100 mM PBS buffer. Each analyte solution (10 μL) was loaded onto the sample loading site, and the results were determined using the above method.

5. References

(1) (a) Ma, J.; Dasgupta, P. K. *Anal. Chim. Acta* **2010**, *673*, 117-125; (b) Beasley, D. M. G.; Glass, W. I. *Occup. Med. (Lond)* **1998**, *48*, 427-431.

(2) Biller, J. *Interface of neurology and internal medicine* Lippincott Williams & Wilkins, 2007, p 939.

(3) Baskin, S. I.; Brewer, T. G. *Medical Aspects of Chemical and Biological Warfare*; TMM Publication: Washington DC, 1997, p 271-286.

(4) Koenig, R. *Science* **2000**, *287*, 1737-1738.

(5) Safavi, A.; Maleki, N.; Shahbaazi, H. R. *Anal. Chim. Acta* **2004**, *503*, 213-221.

(6) Langmaier, J.; Janata, J. *Anal. Chem.* **1992**, *64*, 523-527.

(7) Christison, T. T.; Rohrer, J. S. *J. Chromatogr. A* **2007**, *1155*, 31-39.

(8) (a) Lee, C.-H.; Yoon, H.-J.; Shim, J.-S.; Jang, W.-D. *Chem. Eur. J.* **2012**, *18*, 4513-4516; (b) Badugu, R.; Lakowicz, J. R.; Geddes, C. D. *Dyes Pigm.* **2005**, *64*, 49-55; (c) Badugu, R.; Lakowicz, J. R.; Geddes, C. D. *J. Am. Chem. Soc.* **2005**, *127*, 3635-3641.

(9) Xu, Z.; Chen, X.; Kim, H. N.; Yoon, J. *Chem. Soc. Rev.* **2010**, *39*, 127-

137.

(10) (a) Yetisen, A. K.; Akram, M. S.; Lowe, C. R. *Lab Chip* **2013**, *13*, 2210-2251; (b) Lewis, G. G.; DiTucci, M. J.; Phillips, S. T. *Angew. Chem. Int. Ed.* **2012**, *51*, 12707-12710; (c) Yildiz, U. H.; Alagappan, P.; Liedberg, B. *Anal. Chem.* **2013**, *85*, 820-824.

(11) Ono, M.; Hayashi, S.; Kimura, H.; Kawashima, H.; Nakayama, M.; Saji, H. *Biorg. Med. Chem.* **2009**, *17*, 7002-7007.

(12) (a) Shen, L.; Hagen, J. A.; Papautsky, I. *Lab Chip* **2012**, *12*, 4240-4243; (b) Ashokkumar, P.; Weißhoff, H.; Kraus, W.; Rurack, K. *Angew. Chem. Int. Ed.* **2014**, *53*, 2225-2229.

(13) French, A. P.; Taylor, E. F. *An Introduction to Quantum Physics*; Van Nostrand Reinhold: London, 1978.

(14) Karton-Lifshin, N.; Albertazzi, L.; Bendikov, M.; Baran, P. S.; Shabat, D. *J. Am. Chem. Soc.* **2012**, *134*, 20412-20420.

(15) Liu, H.; Xiang, Y.; Lu, Y.; Crooks, R. M. *Angew. Chem. Int. Ed.* **2012**, *51*, 6925-6928.

Section 2.

Colorimetric and orange light-emitting fluorescent probe for pyrophosphate in water

Abstract

A dual-mode probe based on a benzothiazolium hemicyanine chromophore was designed and synthesized for the detection of pyrophosphate (PPi) in water. The use of a fluorescent probe for colorimetric and long wavelength fluorescence detection of PPi could be suitable for both rapid in-field and bioimaging experiments.

1. Introduction

Pyrophosphate (PPi) is involved in a number of important cellular metabolic processes such as DNA and RNA polymerization reactions and ATP hydrolysis.[1] In addition, researchers have recently reported a relationship between PPi concentration and cancer.[2] In this regard, there is a growing interest in using different detection methods to monitor PPi in biological processes, with fluorescence techniques being the most popular.[3] Although many fluorescent probes for PPi have already been reported, both by our group and others,[4] there is a continuous need for the development of novel probes for this species that can facilitate the study of biological processes involving its release.

It is well known that a fluorophore with near infrared (NIR) or long wavelength emission is desirable for the detection of cellular PPi because of its favorable cell penetrating ability and the minimal overlap with the wavelengths

at which cells exhibit autofluorescence.[5] In addition, a probe that can detect PPi using a colorimetric method could facilitate rapid in-field analysis without sophisticated instrumentation.[3b] Currently, there is considerable interest in developing chemosensors that emit at longer wavelengths and can be visualized with the naked eye.[6] However, there are only a few successful PPi sensors reported to date.[7] Here, a new colorimetric and orange light-emitting fluorescent probe for PPi will be described.

2. Data and results

It was expected that benzothiazolium hemicyanine dye would be a suitable signaling unit for use in biological applications because of its cell permeability, non-toxicity, and long wavelength emission ($\lambda_{em} \approx 560$ nm).[8] Thus, by combining this with a Zn(II)•2,2′-dipycolylamine (DPA) complex as a binding site, an effective fluorescent probe for PPi could be achieved (Figure 1).[4,7] Treatment of 4-hydroxybenzaldehyde with DPA in the presence of formaldehyde gave compound **2**. The benzothiazolium hemicyanine fluorophore was then introduced by Knoevenagel condensation with 3-ethyl-2-methylbenzothiazolium iodide. Sensor **1**•2Zn(II) was obtained by the addition of $Zn(NO_3)_2$ to a solution of **1** in DMSO.

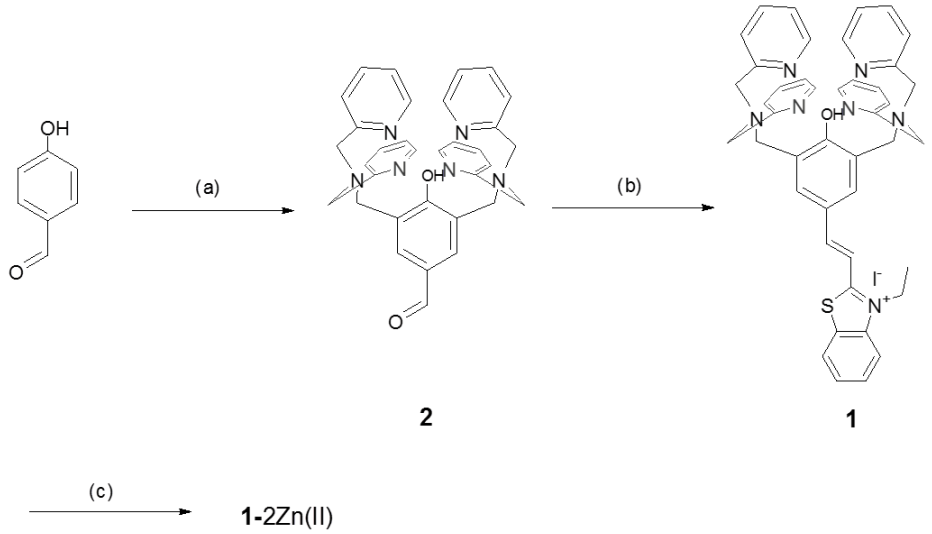

Figure 1. Synthesis of **1**•2Zn(II): (a) 2,2′−Dipicolylamine, aq. formaldehyde, 1,4-dioxane, 110 °C, 2 days, 48% yield (b) 3-Ethyl-2-methylbenzothiazolium iodide, pyridine, EtOH, 80 °C, 1 d, 12% yield (c) $Zn(NO_3)_2$, DMSO, RT, 30 min, quantitative yield.

Photophysical properties of **1**•2Zn(II) in the presence of PPi were monitored by UV−vis and fluorescence spectrometry. UV−vis titration of **1**•2Zn(II) revealed that the maximum intensity wavelength (λ_{abs} = 454 nm) underwent a 27 nm bathochromic shift with increased intensity upon the addition of PPi in 10 mM HEPES buffer (pH 7.4). The intensity of the fluorescence emission of **1**•2Zn(II) at 548 nm was relatively weak (Φ_F = 0.08), whereas the addition of 2 equiv. of PPi caused a prominent increase (ca. 5 times) in fluorescence centered at 558 nm (Φ_F = 0.10)[9] (Figure 2a). The fluorescence intensity exhibited a sharp increase upon the addition of an increasing amount of PPi to the **1**•2Zn(II) solution, with the maximum intensity being exhibited when 1 equiv. of PPi was added (Figure 2b). The binding constant was estimated to be 4.4×10^7 M^{-1}.

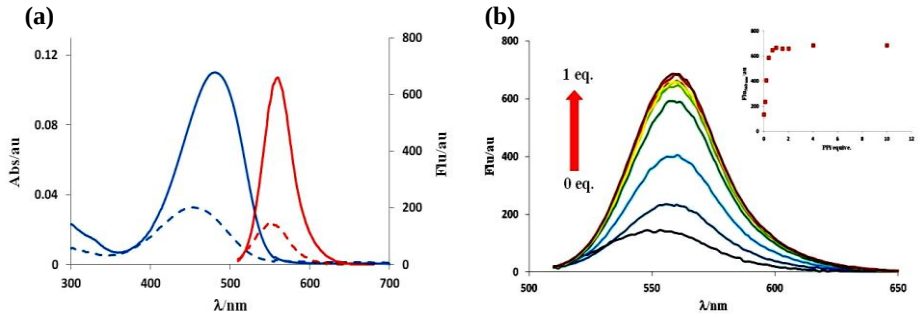

Figure 2. (A) UV−vis absorption (blue dashed line) and fluorescence emission (red dashed line) spectra of **1**•2Zn(II) (10 μM) in the presence of PPi (2 equiv., solid line) in 10 mM HEPES buffer (pH 7.4). (B) Fluorescence emission intensity of **1**•2Zn(II) (10 μM) in various concentrations of PPi (1−100 μM, pH 7.4, 10 mM HEPES buffer). Inset shows increasing fluorescence intensities of **1**•2Zn(II), which are measured at 560 nm with excitation at 500 nm.

To evaluate the selectivity of **1**•2Zn(II) toward PPi, various biological competitive analytes were prepared. As expected, there were no significant changes in the fluorescence intensity upon the addition of an excess amount of phosphate (Pi), CN^-, citrate, Cl^-, F^-, HCO_3^-, OAc^-, N_3^-, and AMP, whereas a detectable response was observed due to ATP. This competitive experiment clearly demonstrated that **1**•2Zn(II) has a high selectivity for PPi over many other biological competitive analytes, apart from nucleoside triphosphates (NTPs) that are present in cells (Figure 3).

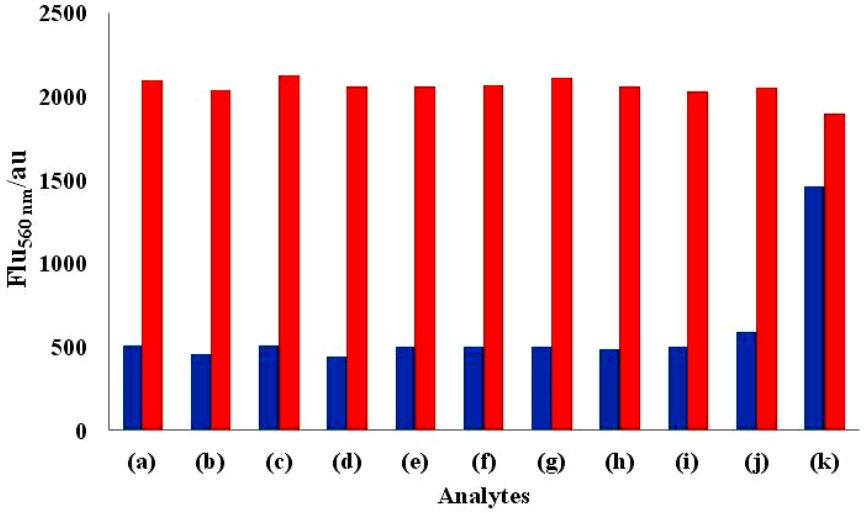

Figure 3. Fluorescence emission intencity of **1**•2Zn(II) (5 μM, pH 7.4 10 mM HEPES buffer) in the presence of (a) probe only, (b) Pi, (c) CN^-, (d) citrate, (e) Cl^-, (f) F^-, (g) HCO_3^-, (h) OAc^-, (i) N_3^-, (j) AMP, (k) ATP. Blue bars represent the addition of analytes (20 equiv.). Red bars represent the subsequent addition of PPi (2 equiv.) to the mixture. All data were measured by fluorescence spectrometer at 560 nm with excitation at 500 nm.

Furthermore, the selective recognition of PPi by **1**•2Zn(II) can be visualized by the naked eye owing to the colorimetric change. Solutions of **1**•2Zn(II) alone and those of it mixed with other analytes, except PPi and ATP, in 10 mM HEPES buffer, appeared yellow, whereas mixtures of **1**•2Zn(II) and either PPi or ATP were pale brown. Therefore, it is clear that **1**•2Zn(II) can distinguish PPi or ATP from other anions (Figure 4). The color change may result from the observable bathochromic shift[10] of **1**•2Zn(II) triggered by the addition of either PPi or ATP (Figure 2a).

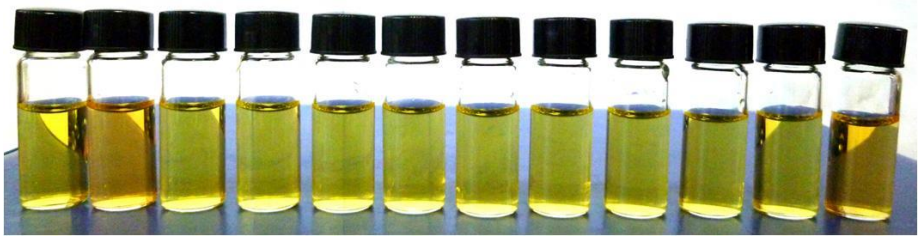

(a) (b) (c) (d) (e) (f) (g) (h) (i) (j) (k) (l)

Figure 4. Colorimetric detection of **1**•2Zn(II) (5 μM, pH 7.4 10 mM HEPES buffer) in the presence of (a) probe only, (b) PPi, (c) Pi, (d) CN^-, (e) citrate, (f) Cl^-, (g) F^-, (h) HCO_3^-, (i) OAc^-, (j) N_3^-, (k) AMP, (l) ATP. 20 equiv. of analytes were added except for PPi (2 equiv.).

To determine whether **1**•2Zn(II) was suitable for use in biological applications, *in vitro* testing using the C2C12 myoblast cell line was carried out (Figure 5). The cells were incubated with **1**•2Zn(II) (80 μM) for 30 min, and subsequently with PPi ($Na_4P_2O_7$, 200 μM) for 30 min. Prior to the addition of PPi, the cells showed only a weak level of fluorescence (Figure 5b),[11] however, a clear intracellular fluorescence increase was observed after the addition (Figure 5d). The viability of the cells after treatment with the probe was verified using the Hoechst nuclear stain (Figure 5a, c).[12] These results show the potential for using **1**•2Zn(II) for the detection of PPi within cells.

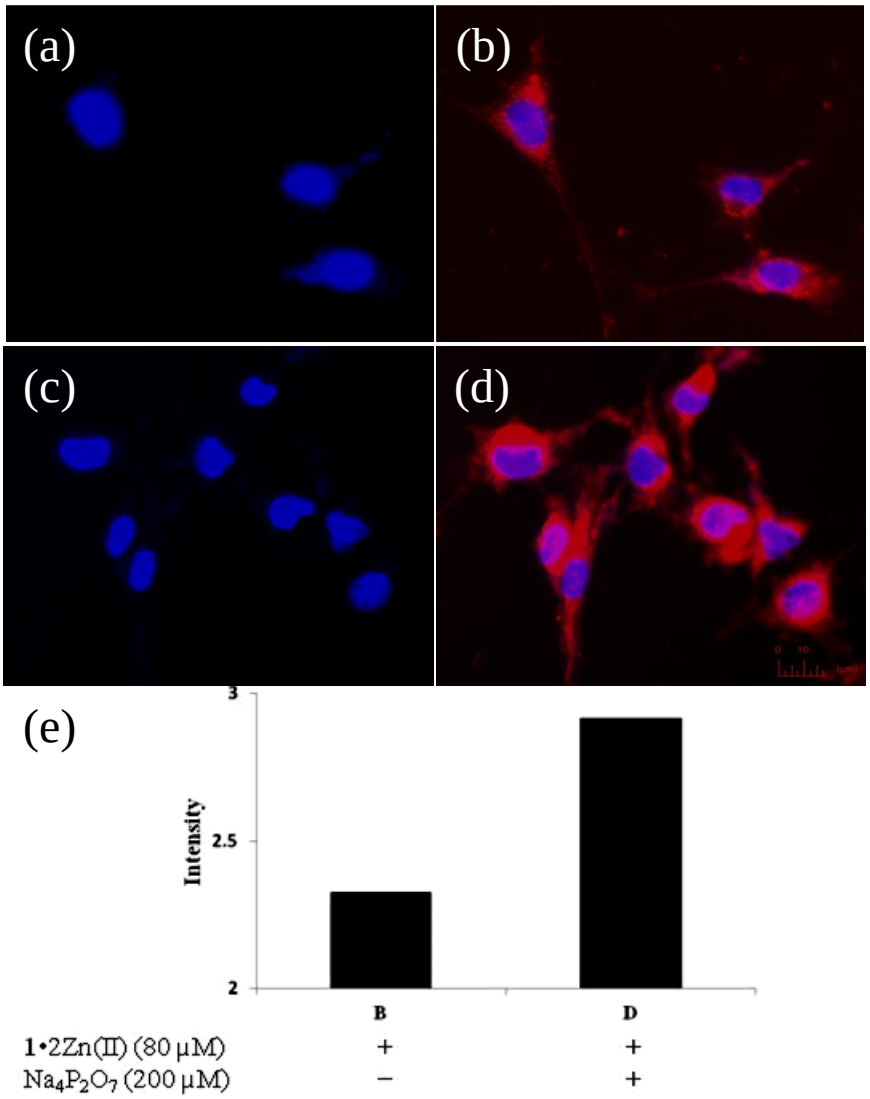

Figure 5. Fluorescence live-cell pseudo-color images of C2C12 myoblast cells. (a and c) Cells stained by Hoechst nuclear dye. (b) Cells incubated with Hoechst nuclear dye and then with **1**•2Zn(II) (80 μM) for 30 min. (d) Cells incubated with Hoechst nuclear dye followed by **1**•2Zn(II) (80 μM) for 30 min, and subsequently, with PPi ($Na_4P_2O_7$, 200 μM) for 30 min. Emission was collected at (a, c) blue channel and (b, d) Cy3 channel upon excitation at (a, c) 350 ± 25 nm (200 W metal halide arc lamp) and (b, d) 543 ± 11 nm (200 W metal halide arc lamp). All images were acquired using a 20× objective. (e) Quantification data from (b) and (d).

3. Conclusion

In conclusion, a highly selective colorimetric and fluorescent probe for PPi has been described. This probe can be applied in biological fluorescence imaging, and its orange emitting light and good cell permeability make it highly desirable for other bio-studies. This would be attractive to biological and medical researchers who are studying the biological roles and diagnostic relevance of PPi.

4. Experimental

4.1. General procedure

5 mM of **1**•2Zn(II) stock solutions was prepared in DMSO. The stock solution of **1**•2Zn(II) was diluted to 5 μM or 10 μM in pH 7.4 10 mM HEPES buffer. UV−vis absorbance and fluorescence changes of **1**•2Zn(II) in the presence of 2 equiv. of PPi were measured by Beckman coulter DU 800 spectrometer and Jasco FP 6500 fluorescence spectrometer, respectively. Fluorescence titration was performed with increasing equiv of PPi addition (0.1−10 equiv.) following by 560 nm with excitation at 500 nm. For the fluorescence selectivity and competition experiment, 10 mM stock solutions of analytes were prepared in water (sodium salt). To a separated solution of **1**•2Zn(II) were added 20 equiv of analytes, and measured by fluorescence spectrometer. Subsequent addition of PPi (2 equiv.) into the separated mixtures was performed. The fluorescence quantum yields were determined by the single point method, following literature procedure.[13]

4.2. HPLC instrument and separation condition

For the purification of crude compound **1**, Semi prep. HPLC was prepared as following: HECTOR-M C18 (21.2 × 150 mm) column (RS tech.) using HPLC system composed of a binary HPLC pump (Waters 1525) and UV−vis detector (Waters 2489). Flow rate was determined to be 8 mL/min with following gradient mobile phase condition: 0 min, 10 % ACN/0.1 % TFA aq. ~ 40 min, 90 % ACN/0.1 % TFA aq. Gained fractions were in basic work-up process, and introduced into next step.

4.3. Biological cell imaging method and equipment

Cell culture. C2C12 myoblast cells were obtained from American Type Culture Collection [ATCC, Manassas, VA, USA]. C2C12 cell lines were cultured in DMEM [GIBCO, Invitrogen] supplemented with heat-inactivated 10% (v/v) fetal bovine serum [GIBCO, Invitrogen] and 1% (v/v) antibiotic-antimycotic solution [GIBCO, Invitrogen]. Cells were maintained in a humidified atmosphere of 5% CO_2 incubator at 37°C, and cultured in 100mm cell culture dish [CORNING].

Biological cell imaging equipment. Cell imaging was performed by InCell analyzer 2000 [GE Healthcare] and fluorescence images were analyzed by InCell analyzer 1000 workstation 3.6 program.

Cell imaging using InCell Analyzer 2000. C2C12 myoblast cells were seeded on black well and clear 96 plate ($3x10^3$ cells / well) and incubated at 5% CO2, 37°C for 24h. **1**•2Zn(II) were treated to the cell for 30min, and subsequently with $Na_4P_2O_7$ [Sigma-Aldrich] for 30min with PBS buffer. Hoechst 33342 (2ug/ml) was added to the cell. After PBS washing, fluorescence images of the plate were taken automatically by InCell analyzer 2000. (**1**•2Zn(II) : Excitation filter : 543±11nm, Emission filter: Red channel, Hoechst 33342: Excitation

filter : 350±25nm, Emission filter: Blue channel).

4.4. Synthetic procedure for compound 1, 2, and 1•2Zn(II)

Compound **2** was prepared by modified literature procedure. [14]

Compound 1. To a solution of **2** (1.18 g, 2.16 mmol) in EtOH (11 mL) were added 3-Ethyl-2-methylbenzothiazolium iodide (791 mg, 2.6 mmol), pyridine (0.2 mL, 2.6 mmol) subsequently, and the mixture was stirred for 1 d at 80°C. A volatile solvent was removed *in vacuo*, and the resultant was introduced into HPLC instrument as mentioned above (reddish oily liquid, 12% yield).

^{1}H NMR (CD_3OD, 300 MHz): δ 8.47 (d, J = 4.5 Hz 4H), 8.22-8.10 (m, 3H), 7.86-7.65 (m, 3H), 7.81 (s, 2H), 7.76 (t, J = 7.5 Hz, 4H), 7.60 (d, J = 7.8 Hz, 4H), 7.29 (t, J = 6.3 Hz 4H), 4.95 (d, J = 7.2 Hz 2H), 3.91 (s, 8H), 3.89 (s, 4H), 1.64 (t, J = 7.2 Hz, 3H); ^{13}C NMR (CD_3OD, 75 MHz): δ 172.0, 158.6, 150.8, 148.0, 141.0, 137.2, 132.3, 129.3, 128.1, 127.9, 125.5, 124.9, 124.5, 123.5, 123.3, 123.2, 122.4, 115.6, 59.2, 54.4, 44.0, 29.3; HRMS (FAB$^+$, m-NBA) *m/z* calculated for $C_{43}H_{42}N_7OS^+$: 704.3172, observed: 704.3179.

Compound 1•2Zn(II). To a solution of **1** (4.32 μmol) in DMSO (0.4 mL) was added a 270 mM stock solution of $Zn(NO_3)_2 \cdot 6H_2O$ (32 μL, 8.62 μmol) in DMSO. After aged for 30 min at RT, the resulting solution was used as a 10 mM stock solution of **1**•2Zn(II) without further purification (reddish solution, quantitative yield).[15]

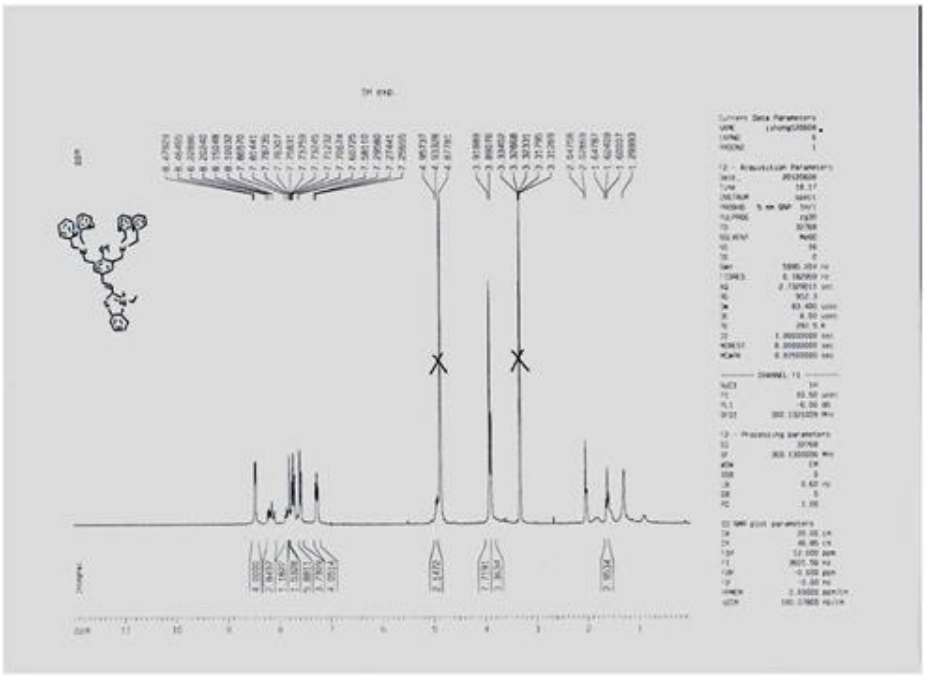

Figure 6. ^{1}H-NMR spectrum of **1**.

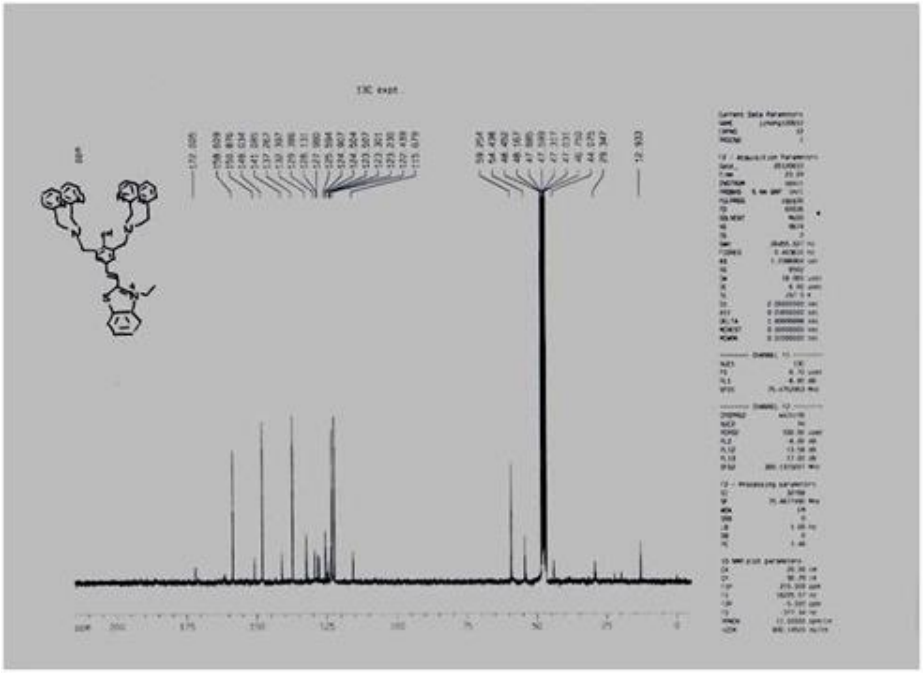

Figure 6. ^{13}C-NMR spectrum of **1**.

5. References and notes

(1) Heinonen, J. K. *Biological Role of Inorganic Pyrophosphate*; Kluwer Academic Publishers: Norwell, 2001.

(2) Xu, S.; He, M.; Yu, H.; Cai, X.; Tan, X.; Lu, B.; Shu, B. *Anal. Biochem.* **2001**, *299*, 188-193.

(3) (a) Vance, D. H.; Czarnik, A. W. *J. Am. Chem. Soc.* **1994**, *116*, 9397-9398; (b) Lee, D. H.; Im, J. H.; Son, S. U.; Chung, Y. K.; Hong, J.-I. *J. Am. Chem. Soc.* **2003**, *125*, 7752-7753; (c) Nyren, P.; Pettersson, B.; Uhlen, M. *Anal. Biochem.* **1993**, *208*, 171-175.

(4) (a) Kim, S. K.; Lee, D. H.; Hong, J.-I.; Yoon, J. *Acc. Chem. Res.* **2008**, *42*, 23-31; (b) Lee, D. H.; Kim, S. Y.; Hong, J.-I. *Angew. Chem. Int. Ed.* **2004**, *43*, 4777-4780; (c) Lee, J. H.; Park, J.; Lah, M. S.; Chin, J.; Hong, J.-I. *Org. Lett.* **2007**, *9*, 3729-3731; (d) Ojida, A.; Nonaka, H.; Miyahara, Y.; Tamaru, S.-i.; Sada, K.; Hamachi, I. *Angew. Chem. Int. Ed.* **2006**, *45*, 5518-5521; (e) Cho, H. K.; Lee, D. H.; Hong, J.-I. *Chem. Commun.* **2005**, 1690-1692; (f) Lee, H. N.; Xu, Z.; Kim, S. K.; Swamy, K. M. K.; Kim, Y.; Kim, S.-J.; Yoon, J. *J. Am. Chem. Soc.* **2007**, *129*, 3828-3829.

(5) (a) Karton-Lifshin, N.; Segal, E.; Omer, L.; Portnoy, M.; Satchi-Fainaro, R.; Shabat, D. *J. Am. Chem. Soc.* **2011**, *133*, 10960-10965; (b) Fu, M.; Xiao, Y.; Qian, X.; Zhao, D.; Xu, Y. *Chem. Commun.* **2008**, 1780-1782.

(6) (a) Yuan, M.; Li, Y.; Li, J.; Li, C.; Liu, X.; Lv, J.; Xu, J.; Liu, H.; Wang, S.; Zhu, D. *Org. Lett.* **2007**, *9*, 2313-2316; (b) Tatay, S.; Gaviña, P.; Coronado, E.; Palomares, E. *Org. Lett.* **2006**, *8*, 3857-3860.

(7) (a) Zhu, W.; Huang, X.; Guo, Z.; Wu, X.; Yu, H.; Tian, H. *Chem. Commun.* **2012**, *48*, 1784-1786; (b) Feng, X.; An, Y.; Yao, Z.; Li, C.; Shi, G. *ACS Appl.*

Mater. Inter. **2012**, *4*, 614-618.

(8) Zhu, B.; Yuan, F.; Li, R.; Li, Y.; Wei, Q.; Ma, Z.; Du, B.; Zhang, X. *Chem. Commun.* **2011**, *47*, 7098-7100.

(9) (a) Fluorescence quantum yields were determined using rhodamine B (Φ_F = 0.49 in ethanol) as a standard; (b) Casey, K. G.; Quitevis, E. L. *J. Phys. Chem.* **1988**, *92*, 6590-6594.

(10) (a) Leontiev, A. V.; Rudkevich, D. M. *J. Am. Chem. Soc.* **2005**, *127*, 14126-14127; (b) Sola, A.; Tarraga, A.; Molina, P. *Dalton Trans.* **2012**, *41*, 8401-8409.

(11) We think that the observed weak fluorescence prior to PPi addition may be due to the presence of cellular PPi and NTPs.

(12) The cell imaging experiments with lower concentrations of **1**•2Zn(II) ($\leq$ 40 μM) were not successful as the fluorescence was not high enough for monitoring the fluorescence differences. After treatment with higher concentrations of **1**•2Zn(II) ($\geq$160 μM) and PPi ($\geq$400 μM), denaturation of cells was occasionally observed.

(13) Lakowicz, J. R. *Principles of Fluorescence Spectroscopy*; Kluwer Academic: New York, 1999.

(14) Shin, I.-S.; Bae, S. W.; Kim, H.; Hong, J.-I. *Anal. Chem.* **2010**, *82*, 8259-8265.

(15) Rhee, H.-W.; Lee, S. H.; Shin, I.-S.; Choi, S. J.; Park, H. H.; Han, K.; Park, T. H.; Hong, J.-I. *Angew. Chem. Int. Ed.* **2010**, *49*, 4919-4923.

국문초록 (Abstract in Korean)

전자효과를 적절히 활용하면, 기존 센싱시스템 보다 향상된 방법을 개발할 수 있다.

Part I에서는 광산화반응을 기반으로 하는 새로운 타입의 플라빈 센싱 방법을 서술한다. [9*H*]xanthene부분이 플라빈의 강한 전자받개 능력에 의해서 산화된 후 장파장(λ_{em}= 600nm)에서 높은 밝기(brightness, $\varepsilon \times \Phi_F$= $6.50 \times 10^3 M^{-1}cm^{-1}$)의 형광 방출을 보일 수 있게 프로브를 설계했다. 플라빈에 조사(irradiation)해준 빛의 세기 및 파장은 [9*H*]xanthene부분이 플라빈에 의해 산화되는 광산화반응(flavin-mediated photo-oxidation)속도에 강하게 영향을 주었다. 프로브는 다른 산화제(oxidant)보다 플라빈에 의해서 선택적으로 산화 되었고, 빛에 대한 안정성 및 미토콘드리아에 위치하는 특징을 보였다. 또한, 미토콘드리아에 존재하는 산화 상태의 플라빈을 프로브를 이용해서 살아있는 세포 및 조직에서도 관찰했다.

프로브가 빛에 노출되었을 때, [9*H*]xanthene부분이 스스로 산화(autooxidation)가 되는 문제점을 드러냈지만, 프로브에 양전하를 띠는 아연복합체(Zn^{2+}-complex)를 도입했을 때 그 자발적인 산화 속도가 늦춰졌다. 이것은 양전하에 의한 정전기적 힘에 의해 [9*H*]xanthene부분이 열역학적으로 안정화된 결과임을 밝혔다. 반면에, 플라빈에 의한 광산화반응에서는 양전하가 프로브의 산화 속도를 높이는 역할을 했다. 그 양전하가 플라빈의 환원전위를 낮췄고, [9*H*]xanthene에서 플라빈으로의 분자 간 전자전달과정에 유리한 정전기적 환경을 제공했다는 것을 실험을 통해 밝혔다. 성능이 향상된 프로브를 이용하여 호산구(eosinophils)를 이미징 했고,

인간의 혈액 세포 용해물(blood cell lysate)에 적용해서 호산구 증가증(eosinophilia)을 진단하는 데에 이용해 보았다.

Part Ⅱ에서는 정전기적 상호작용을 기반으로 하는 파이로포스페이트(PPi) 검출용 센싱 플렛폼에 대해서 기술한다. 기존 분자인식 방법을 산화그래핀과 조합하여 새로운 PPi 센싱 플렛폼을 개발했다. 이것은 뉴클레오타이드(NTPs)가 많은 상황에서도 PPi에 대한 높은 선택성을 보였으며, 최종적으로 유전자증폭기술(polymerase chain reaction)에도 응용했다.

Part Ⅲ에서는 콘쥬게이션 효과가 단분자 프로브에 미치는 영향에 관해서 기술한다. Section I에서는, 시안화이온을 검출할 수 있는 단분자 프로브를 합성하고, 이것을 페이퍼 스트립(paper strip)에 도입하여 시안화이온을 정량분석한 내용을 다룬다. 시안화이온이 프로브의 전자가 부족한 부분과 친핵성 반응을 해서 프로브의 파이콘쥬게이션 길이가 짧아졌고 쌍극자 모멘트도 작아졌다. 따라서 프로브의 흡수 및 방출파장이 단파장 쪽으로 크게 이동했다. 이어서 프로브를 내부표준시스템(internal referencing system)을 도입한 페이퍼 스트립에 적용해서 시안화이온을 넓은 범위(0–25mM)에서 검출했다.

Section Ⅱ에서는, 장파장에서 형광 방출($\lambda_{em} \approx$ 560nm) 할 수 있는 프로브를 가지고 세포 내 PPi를 이미징한 내용에 대해서 서술한다. 합성한 프로브는 다른 음이온들 보다 PPi에 대해서 선택성을 보여주었지만, ATP에 대해서도 약 10^2정도 약한 세기로 결합했다. 그럼에도 불구하고, 프로브를 이용하여 세포(C2C12 myoblast) 내에 존재하는 PPi에 대한 형광 이미지를 얻을 수 있었다.

KeyWords: 단분자 프로브, 형광 검출법, 전기장 효과, 광산화반응, 플라빈, 정전기적 상호작용, 산화그래핀, 파이로포스페이트, 콘쥬게이션 효과, 페이퍼 스트립